



**UNIVERSIDAD DE CHILE
FACULTAD DE CIENCIAS FÍSICAS Y MATEMÁTICAS
DEPARTAMENTO DE GEOLOGÍA**

**PROPIEDADES MECÁNICAS DE ROCAS CON VETILLAS SOMETIDAS A ALTAS
TASAS DE DEFORMACIÓN**

**TESIS PARA OPTAR AL GRADO DE MAGISTER EN CIENCIAS
MENCIÓN GEOLOGÍA**

FRANCO MATÍAS ROBBIANO MUÑOZ

**PROFESOR GUÍA
SOFÍA REBOLLEDO LEMUS**

**PROFESOR CO-GUÍA
LUIS FELIPE ORELLANA ESPINOZA**

**MIEMBROS DE LA COMISIÓN
SERGIO SEPÚLVEDA VALENZUELA
JOHN BROWNING**

SANTIAGO DE CHILE

2022

Resumen

Los estallidos de rocas corresponden a eventos complejos, caracterizados por la liberación espontánea de energía en los límites de las excavaciones subterráneas en roca en zonas de tensión de confinamiento. En minería subterránea, tanto la seguridad de los trabajadores como de los equipos se ve mermada por estos eventos ya que implica un riesgo para las operaciones mineras: lesiones a los trabajadores o víctimas mortales, daños a la infraestructura y al equipo de la mina, una rehabilitación que requiere mucho tiempo y, por lo tanto, pérdidas de producción y su evaluación representa un gran desafío.

En este estudio, reportamos una serie de pruebas de compresión uniaxial mediante el uso de una barra de presión Hopkinson dividida (SHPB), una barra triaxial tipo Hopkinson (THB), y una cámara de alta velocidad de hasta 200.000fps, para comprender el papel de las cargas dinámicas y las altas tasas de deformación (10 a 10^2 s^{-1}) en el comportamiento mecánico y en los patrones de fractura de rocas con vetillas. Las muestras corresponden a cilindros (SHPB) y cubos (THB) elaborados a partir de rocas de los principales distritos de gran minería subterráneos de Chile: Chuquicamata (CHQ), Andina (RB) y El Teniente (CMET). Así, se representan tres estados de tensión subterránea: Desconfinado (SHPB), confinamiento uniaxial (THB), y confinamiento biaxial (THB).

Los resultados obtenidos a través de la SHPB muestran un claro aumento de la resistencia a la carga uniaxial en relación con los resultados de técnicas con tasas de carga cuasi-estática. El aumento fue de hasta 2,2 veces en CMET, 1,8 en RB y 2,6 en CHQ. Además, el factor de aumento dinámico (DIF) indica una fuerte dependencia de la tasa de deformación de las muestras de CHQ. Este efecto en las muestras de RB y CMET es menos evidente. Los datos obtenidos con las pruebas de compresión dinámica indican que tanto el aumento de la rigidez como la resistencia a la compresión dinámica dependen en gran medida de la tasa de deformación de la roca. Además, informamos una relación directa entre los patrones de fractura y la presencia de vetillas.

Los resultados obtenidos a través de THB no son concluyentes con respecto al aumento de la resistencia a la carga uniaxial, al compararlo con respecto al estado desconfinado. Sin embargo, se observa un aumento del módulo elástico al aumentar σ_2 . Dos tipos de curvas post-peak, I y II, son reportadas en la curva de carga-deformación: La curva post-peak tipo I está asociada a fracturas singulares por la cual la muestra no pierde su capacidad de carga en un estado de confinamiento biaxial. La curva post-peak tipo II está asociada a una fragmentación del espécimen ensayado, y a la expulsión de fragmentos desde las caras libres. En ambos casos, la propagación de la fractura está controlada por las vetillas que están orientadas de manera favorable con respecto a la carga dinámica. Se reproducen dos fenómenos asociados al strainburst en los ensayos biaxiales, el Slab buckling o pandeamiento, y la expulsión de fragmentos a altas velocidades luego de la fragmentación de la muestra durante su fase post-peak.

De acuerdo con los resultados, sugerimos que la propagación de la fractura en rocas con vetillas que fallan a altas tasas de deformación ocurre través de la matriz y las vetillas cuando las propiedades mecánicas instantáneas de este tipo de roca muestran una fuerte dependencia de la tasa de deformación, mientras que se restringen sólo a las vetillas cuando esta dependencia es menos evidente. Frente a un pulso dinámico que generen tasas de deformación entre 10 a 10^2 s^{-1} , aumenta la rigidez instantánea, y por lo tanto la disipación de energía también. La propensión a la formación de bloques es mayor en rocas con vetillas. Estas son condiciones que favorecen la ocurrencia estallidos de rocas, y podrían incrementar la severidad de este fenómeno en las excavaciones subterráneas de los distritos mineros estudiados.

Tabla de contenido

1	Introducción.....	1
1.1	Preámbulo	1
1.2	Motivación	2
1.3	Objetivos	3
1.3.1	Objetivo general	9
1.3.2	Objetivos específicos.....	9
1.4	Alcances.....	9
1.5	Metodología.....	10
1.6	Resumen de la investigación.....	20
2	Artículo 1: Dynamic compression test on veined rocks at high strain rates and their implications to strainburst in deep mining	21
3	Artículo 2: Dynamic mechanical properties under confinement of veined rocks from El Teniente Mine in Chile.....	47
4	Conclusiones y trabajo futuro.....	65
4.1	Conclusiones generales.....	65
4.2	Recomendaciones y trabajo futuro	66
5	Bibliografía.....	67

Agradecimientos

Esta tesis de magister se ha realizado con el financiamiento del proyecto basal FB-0809 del Centro Avanzado de Tecnología Minera (AMTC).

Agradezco al profesor Dr. Luis Felipe Orellana Espinoza por su excelente labor como docente, y además por su confianza, respeto y apoyo tanto con el trabajo realizado como hacia mí. Además, quiero agradecer a la profesora Sofía Rebollodo por su constante apoyo, tanto académico como administrativo. Agradezco además a los profesores Dr. Sergio Sepúlveda y Dr. John Browning por sus comentarios y sugerencias en el proceso de revisión del documento de tesis.

Agradezco a Nadia, por apoyarme desde el inicio en la decisión de realizar mis estudios de magister, y a la vez por estar presente durante el largo proceso. Esta etapa nos ha dejado grandes enseñanzas y bellas experiencias. Sin duda alguna este título es en parte tuyo.

Agradezco a mi mamá y papá, por entregarme, a través de su esfuerzo, determinación, y perseverancia, las herramientas y las ganas para cumplir mis sueños. Agradezco a mi hermano y hermanas, porque de ustedes aprendo día a día. Agradezco a mis abuelos y abuelas, porque su sagacidad ha sido la base de mis logros.

Agradezco finalmente a quienes me entregaron su inmenso e incondicional cariño en su breve paso por el mundo terrenal, y que hoy viven eternamente en mis recuerdos. Facundo, Abra, Bella, Luna, Canela y Bajuan.

*"I suppose you think that nothing much is happening at the moment...aha...
Well, that's what I want to talk to you all about. Endings
Now, endings normally happen, at the end...
But as we all know,... endings are just beginnings"*

Amarok

Capítulo 1

1 Introducción

1.1 Preámbulo

La dinámica de las rocas corresponde al estudio del comportamiento mecánico de las rocas sometidas a condiciones de cargas dinámicas. Los procesos que involucran un comportamiento dinámico de las rocas están presentes en la explotación de los recursos minerales, y por lo tanto, durante la excavación del macizo rocoso para el acondicionamiento de la infraestructura minera subterránea. Algunos de estos procesos dinámicos son:

- Tronadura de rocas mediante perforación tradicional y tronadura (P&T).
- Corte y penetración de rocas durante la excavación de la tuneladora (TBM).
- Daños por estallidos de rocas en las galerías.
- Fallas.
- Eventos sísmicos inducidos.

Las rocas experimentan un comportamiento de tensión-deformación diferente al comparar los resultados de un ensayo dinámico y otro de compresión cuasi-estática. Es de consenso general que, ante un aumento en la tasa de carga, y por consiguiente ante una tasa de deformación alta, la respuesta mecánica de las rocas y el comportamiento del fracturamiento son afectados, lo que incluye el módulo elástico, el módulo de corte, la razón de Poisson, la resistencia a la compresión y la resistencia a la tracción.

La mayoría de las metodologías con las que se elaboraron estudios dinámicos en rocas contemplaron la aplicación de tasas de deformación entre 10 s^{-1} a 10^3 s^{-1} mediante el uso de una barra de presión dividida de Hopkinson, o barra de Kolsky. Estos estudios indican que tanto el comportamiento mecánico como el proceso de fracturamiento, en condiciones dinámicas, son inherentemente diferentes al compararlos con la misma roca sometida a condiciones de carga cuasi-estática. Es decir:

- Mejora de las propiedades mecánicas, p. ej. resistencia a la compresión, y tenacidad a la fractura
- Comportamientos de fractura, p. ej. fracturamiento simple, fracturamiento múltiple y pulverización.

A pesar del gran avance en los ensayos para la estimación de las propiedades dinámicas de las rocas, hay una falta de información sobre las propiedades dinámicas de las rocas provenientes de la minería, donde además pueden coexistir múltiples fuentes de cargas dinámicas durante la operación minera.

Las rocas encontradas en una faena minera distan de ser continuas y homogéneas, y suelen caracterizarse por la presencia de diferentes tipos de vetillas, las que a su vez pueden distribuirse espacialmente en tres estilos estructurales diferentes: 1) stockworks (diseminado), 2) vetas y 3) brechas hidrotermales, todas ellas dentro de cuerpos mineralizados de cobre-molibdeno, es decir, pórfidos cupríferos. Las vetillas son una característica principal por la cual estas rocas se consideran anisotrópicas, y el comportamiento dinámico de este tipo de rocas aún no es bien conocida. De hecho, la mayoría de los estudios previos sobre las propiedades mecánicas de las rocas con vetillas se han llevado a cabo en condiciones de fluencia (10^{-8} a 10^{-5} s^{-1}) y cuasi-estáticas (10^{-5} a 10^{-1} s^{-1}), en pruebas de compresión uniaxial y triaxial, cuyos resultados indican una fuerte

Introducción

influencia de la resistencia máxima a la compresión en relación con la orientación del plano de la vetilla con respecto a la orientación de la carga axial.

Investigaciones recientes se han centrado en el estudio de las propiedades dinámicas de muestras anisotrópicas de carbón, lutitas, y granitos ((J. Li et al., 2021; Xia et al., 2008; Yang et al., 2020) mostrando que las propiedades mecánicas dinámicas son sensibles a la dirección de la característica principal de la anisotropía. con respecto al eje de carga. Sin embargo, ninguno de estos estudios se ha centrado en las propiedades dinámicas de las rocas con vetillas, en las cuales no existe necesariamente una condición de regularidad (p. ej. planos de foliación, textura, laminación, bandeadimiento, clivaje).

1.2 Motivación

Las rocas en un pórfido cuprífero distan de ser continuas y homogéneas, y suelen caracterizarse por la presencia de diferentes tipos de vetillas, las que a su vez pueden distribuirse espacialmente en tres estilos estructurales diferentes: 1) stockworks o diseminado, 2) vetas y 3) brechas, todas ellas dentro de cuerpos de mineral de cobre-molibdeno.

Las vetillas son la característica principal, a escala de muestra de mano, por la cual estas rocas se consideran anisotrópicas, y el comportamiento dinámico de este tipo de rocas en Chile aún no se ha investigado. La mayoría de los estudios previos sobre las propiedades mecánicas de estas rocas se han llevado a cabo en condiciones de fluencia (10^{-8} a 10^{-5} s $^{-1}$) a quasi-estáticas (10^{-5} a 10^{-1} s $^{-1}$), en pruebas de compresión uniaxial y triaxial.

Investigaciones recientes se han centrado en el estudio de las propiedades dinámicas de muestras anisotrópicas de carbón, granito y lutitas, mostrando que las propiedades mecánicas dinámicas son sensibles a la dirección de la característica principal de la anisotropía con respecto al eje de carga (p. ej. planos de foliación, texturas, laminación) Sin embargo, ninguno de estos estudios se ha centrado en las propiedades dinámicas de las rocas con vetillas, en las cuales no existe necesariamente una condición de regularidad, tanto mineralógica como espacial.

Por su parte, la creciente demanda de commodities metálicos conlleva la necesidad de garantizar tanto reservas como recursos de minerales. Actualmente, se han descubierto gran parte de los yacimientos minerales superficiales, y se espera que la mayoría de las minas se profundicen y se estudie la factibilidad de una explotación subterránea. Una de las principales preocupaciones frente a esta realidad es el aumento de los costos de inversión y costos operativos debido a la profundidad de las excavaciones y los riesgos asociados.

Durante las excavaciones de galerías y túneles en una faena minera subterránea, el macizo rocoso se ve afectado por dos configuraciones de confinamiento. El estado de confinamiento estático, que puede ser desconfinado en la interfaz cercana al límite de la excavación. También puede ser uniaxial en una estructura tipo pilar, o biaxial en el entorno radial de un túnel, e incluso triaxial en un entorno radial lejano a la excavación.

Las fuentes de cargas dinámicas modifican la configuración estática, imponiendo una configuración de naturaleza dinámica. Las fuentes de cargas pueden estar relacionadas con las actividades mineras, como vibraciones por métodos de excavación mecanizadas, tronaduras asociadas tanto al desarrollo como al nivel de hundimiento, y eventos sísmicos, tanto naturales como inducidos, p. ej. terremotos y estallidos de rocas, respectivamente. Las cargas dinámicas son de particular importancia ya que modifican el comportamiento mecánico de la roca y el macizo rocoso.

Introducción

En excavaciones subterráneas, el estallido de rocas corresponde un evento violento y repentino cerca de los límites de una excavación. Corresponde a una falla violenta, con liberación de energía de deformación, que afecta a rocas frágiles altamente estresadas. Varios autores han clasificado el mecanismo del estallido de rocas (J. Zhou et al., 2018a, y las referencias en el mismo), y junto con ello clasificaciones de su severidad. Según Kaiser et al. (1996), el mecanismo de estallido de rocas se puede agrupar en tres categorías generales:

- Strainburst
- Fault-slip burst
- Pillarburst

El mismo autor señala que el strainburst es el mecanismo de explosión de rocas más frecuente, y que puede ser causada por una perturbación dinámica, predominantemente por pulsos de tensión o transferencia de energía de un evento sísmico remoto. En Chile, más de 100 de estos eventos se registraron desde 1992 en la mina El Teniente. Comprender el fenómeno de los estallidos de rocas representa un gran desafío, ya que este implica riesgos para las operaciones mineras: lesiones a los trabajadores o fatalidades, daños a la infraestructura y equipos de la mina, rehabilitación que requiere mucho tiempo y, por lo tanto, pérdidas de producción.

La evaluación de los estallidos de rocas se puede realizar desde diferentes aristas, los que incluyen datos empíricos, técnicas de simulación, algoritmos matemáticos y diagramas de estallidos de rocas. Sumado a ello, un estallido de rocas puede ser reproducido a escala de laboratorio tanto a través de ensayos quasi-estáticos como dinámicos.

Con el objetivo de entender mejor la influencia de las vetillas en el comportamiento dinámico de las rocas que las contienen, en este estudio se han llevado a cabo una serie de pruebas aplicando altas tasas de deformación. Las muestras empleadas corresponden a rocas de pórfidos cupríferos de distritos mineros en Chile: El Teniente, Andina y Chuquicamata, todos ellos pertenecientes a la mayor productora de cobre del mundo, la estatal CODELCO. De esta manera, el estudio apunta a explorar y describir la respuesta dinámica de la roca, y entender mejor el mecanismo que controla el estallido de rocas en este tipo de litologías en Chile

1.3 Marco geológico distritos mineros

En el borde sur-occidental de Sudamérica, la placa oceánica de Nazca subduce a la placa continental Sudamericana, generando condiciones para la fusión parcial del manto astenosférico, y la posterior acumulación de magmas en el moho. Ambos, el proceso de generación, y la dinámica interna en el ascenso del magma a través de la corteza, permiten la liberación de fluidos hidrotermales que transportan minerales, y que alteran la mineralogía de la roca encajante. La precipitación de estos minerales en fracturas o porosidades resulta en la generación de depósitos minerales magmáticos-hidrotermales.

Una franja metalógénica se caracteriza por una agrupación de depósitos minerales magmáticos-hidrotermales, de uno o más tipos característicos de depósitos, dispuestos en forma de cinturones longitudinales de orientación norte-sur, cuyo emplazamiento ocurre durante períodos discretos: Los más antiguos se ubican al oeste, en la Cordillera de la Costa, mientras que los más recientes, al este, en la Cordillera de los Andes.

En la figura siguiente se indican las principales franjas metalógénicas en Chile indicándose además pórfidos cupríferos en explotación. Las franjas metalógénicas son, de izquierda a derecha partiendo

Introducción

por el Cretácico tardío (Domeyko, Andacollo) hasta el Mioceno medio-Plioceno temprano (Cerro Casale, El Refugio).

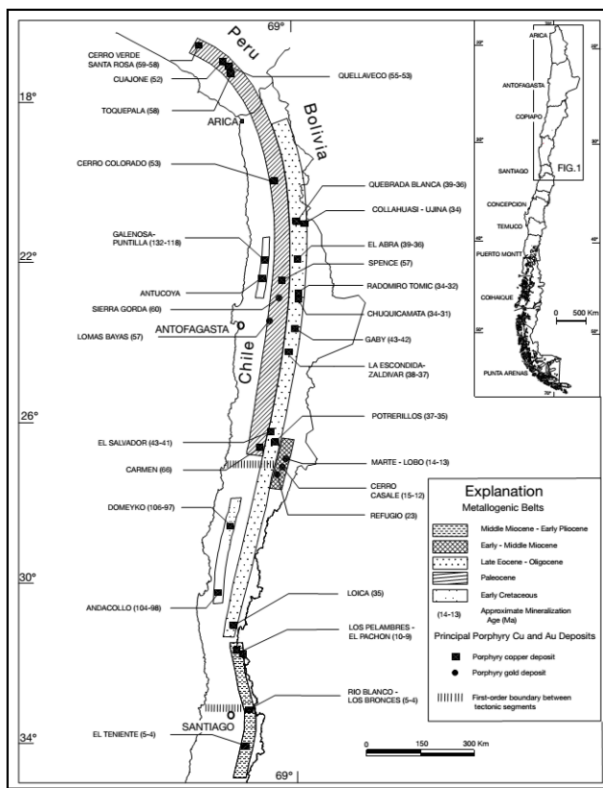


Figura 1 Franjas metalógénicas chilenas. Chuquicamata: Eoceno tardío-Oligoceno, Andina y El Teniente: Mioceno medio-Plioceno temprano.

Un pórfido cuprífero, de acuerdo con el Instituto Americano de Geociencias (AGI), corresponde a un depósito de baja ley de cobre, que siempre está asociado a stocks, pero puede estar en esquistos, calizas silicificadas y rocas volcánicas; Los minerales están típicamente en granos diseminados y/o en vetillas en un gran volumen de roca. La extensión superficial y tamaño del sistema hidrotermal relacionado a un pórfido es un elemento distintivo ya que puede variar entre 10 a 100 km³ de rocas alteradas. Hay tres miembros extremos no excluyentes de estilos estructurales en los pórfidos:

- Stockwork
- Vetas
- Brechas magmático-hidrotermales.

Estos tipos de depósitos están relacionados espacial y temporalmente a complejos intrusivos: Stocks y/o diques félsicos subvolcánicos o epizonales, usualmente porfidíticos y multifase (varias intrusiones sucesivas). Son depósitos epigenéticos, con mineralización de sulfuros hipógenos (primarios) introducidos en rocas preexistentes ya cristalizadas. En relación a su temporalidad con intrusiones, un pórfido cuprífero corresponde a una apófisis intrusiva y/o ejambres de diques sobre cúpulas de batolitos graníticos.

Este tipo de depósitos es de gran importancia para la sociedad, ya que su explotación aporta el 75% del cobre, el 50% del molibdeno y el 20% del oro a nivel mundial, además de tierras raras. Sumado a ello, las minas son de larga vida (Chuquicamata desde 1915, El Teniente desde 1906, Andina desde 1970), impactando fuertemente en el empleo.

1.3.1 Distrito Minero El Teniente

El yacimiento hipógeno de cobre El Teniente pertenece al grupo de depósitos de cobre formados a fines del Mioceno y es uno de los más grandes del mundo. Se encuentra emplazado en rocas intrusivas, piroclásticas, volcánicas y subvolcánicas correspondientes a la Formación Farellones de edad miocena media a superior (Camus, 1975; Cuadra, 1986).

Las rocas intrusivas que se observan en el depósito se emplazan, principalmente, en el miembro inferior de la Formación Farellones y corresponden a: cuerpos irregulares de composición diorítica, que afloran en los alrededores de la localidad de Sewell. En su parte central se encuentra la megaestructura denominada Brecha Braden, con forma de cono invertido (Cuadra, 1986) y en donde se ubican las instalaciones principales de la mina. También se distingue un dique de composición dacítica que solamente aflora en las laderas de la Quebrada Teniente; filones latíticos dispuestos concéntricamente a la Chimenea de Brechas Braden, ubicados al oeste del sector; cuerpos intrusivos y de brechas menores; y un dique de lamprófido que aflora al sur de la megaestructura.

El depósito es el resultado de sucesivos eventos de deformación, intrusión de cuerpos félsicos, mineralización y alteración superpuestos, ocurridos en un lapso de al menos 5,3 Ma, donde los recursos se generaron en un periodo de 1,2 Ma (Maksaev et al., 2002; Maksaev, 2004; Canell et al., 2004). Otra hipótesis es la propuesta por Skewes et al. (2002), la que sugiere que se trataría de un depósito de megabrecha generado por la exsolución de fluidos magmáticos de plutones en enfriamiento. La formación de las vetas tardías, en asociación con el emplazamiento de brechas más jóvenes e intrusiones de pórfidos félsicos, generan una alteración sericítica que en algunos casos contribuye con Cu y en otros elimina o redistribuye la mineralización preexistente (Skewes et al., 2002).

La mineralización de cobre y molibdeno es principalmente en vetillas del tipo stockwork (70%), formando un cuerpo mineralizado de forma elíptica en planta, de 1,6 km x 2 km aproximadamente. El 30% restante se concentra en el cemento de diversa brechas magmáticas-hidrotermales de biotita, anhidrita, cuarzo y turmalina, y en menor proporción, diseminada en la matriz de los cuerpos intrusivos félsicos. Los minerales de mena más importantes, en la zona primaria, corresponden a la asociación calcopirita-bornita-pirita. En la zona de enriquecimiento secundario, el mineral característico es la calcosina y en forma subordinada covelina, cobre nativo y cuprita (Cuadra, 1986). Los sistemas estructurales principales de la mina son: NS, NE, NNW, esta última con continuidad distrital, evidenciados por la traza de los contactos entre unidades de rocas diferentes, por fallas y zonas de cizalle, y por la distribución y geometría de las vetas y vetillas.

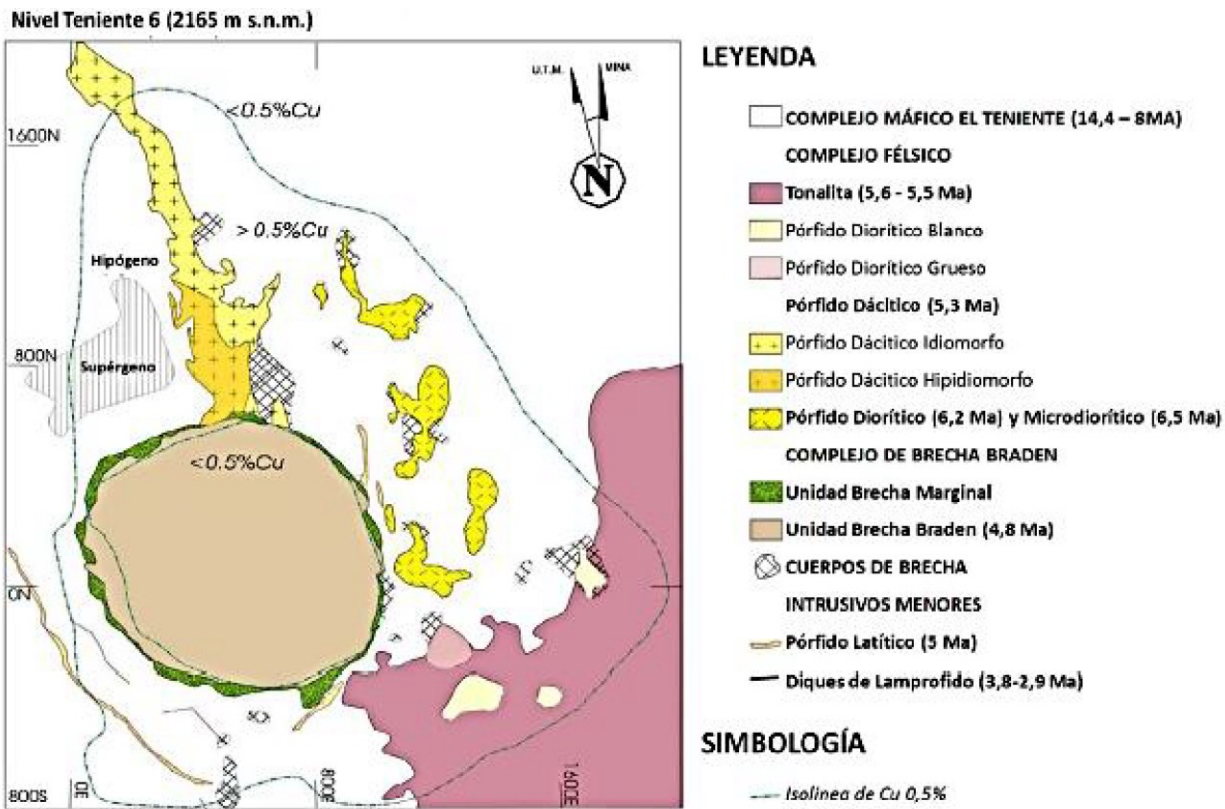


Figura 2 Geología del nivel Teniente 6 (2165 m.s.n.m) (León, 2016)

1.3.2 Distrito Minero Andina

El yacimiento Río Blanco-Los Bronces (Chile Central) es un depósito tipo pórfido cuprífero, asociado con brechas de turmalina. El intrusivo relacionado con la mineralización (Plutón Río Blanco-San Francisco) es de composición granodiorítica y en él se han reconocido, al menos, tres eventos magmáticos temporalmente distintos. Este plutón está intruyendo a la Formación Farellones, compuesta de lavas y rocas volcanoclásticas continentales de composición intermedia. Tanto esta formación como el Plutón Río Blanco-San Francisco subyacen a la Formación Colorado-La Parva consistente de rocas de composición dacítica a riolítica, cuyo modo de emplazamiento es típico de diatremas volcánicas.

La geología del pórfido Río Blanco-Los Bronces ha sido resumida por Serrano et al. (1996), basándose en numerosos informes internos y datos publicados, incluyendo la descripción de Warnaars et al. (1985) de la mina Los Bronces. Vargas et al. (1999) revisaron las brechas mineralizadas en los sectores de Río Blanco y Los Bronces, mientras que Skewes et al. (2003) proporcionaron una descripción detallada del yacimiento de la brecha Donoso en la mina Los Bronces.

La configuración del yacimiento a escala regional y de distrito ha sido descrita por Skewes y Stern (1995, 1996), Kay et al. (1999), Kay y Mpodozis (2001, 2002), Skewes et al. (2002) y Hollings et al. (2005). Las rocas que albergan la mineralización de brecha y stockwork incluyen flujos subhorizontales, dominanteamente andesíticos, subaéreos y volcaniclásticos, que han sido asignados a la Formación Farellones (Stambuk et al., 1985; Warnaars et al., 1985) o a la Formación Abanico más antigua (Rivano et al., 1990), ambas consideradas de edad temprana o media del Mioceno

Introducción

(Vergara et al., 1988). Sin embargo, gran parte del mineral está alojado en unidades granitoides intermedias a silílicas que constituyen el margen occidental del batolito más joven de San Francisco, de edad inferiora del Mioceno temprano o medio. La alteración hidrotermal de estas rocas del terreno, tanto potásica como, con menor intensidad, sericitica, ha provocado incertidumbre en la interpretación de los datos de edad K-Ar disponibles, especialmente en lo que se refiere a la edad del mineral.

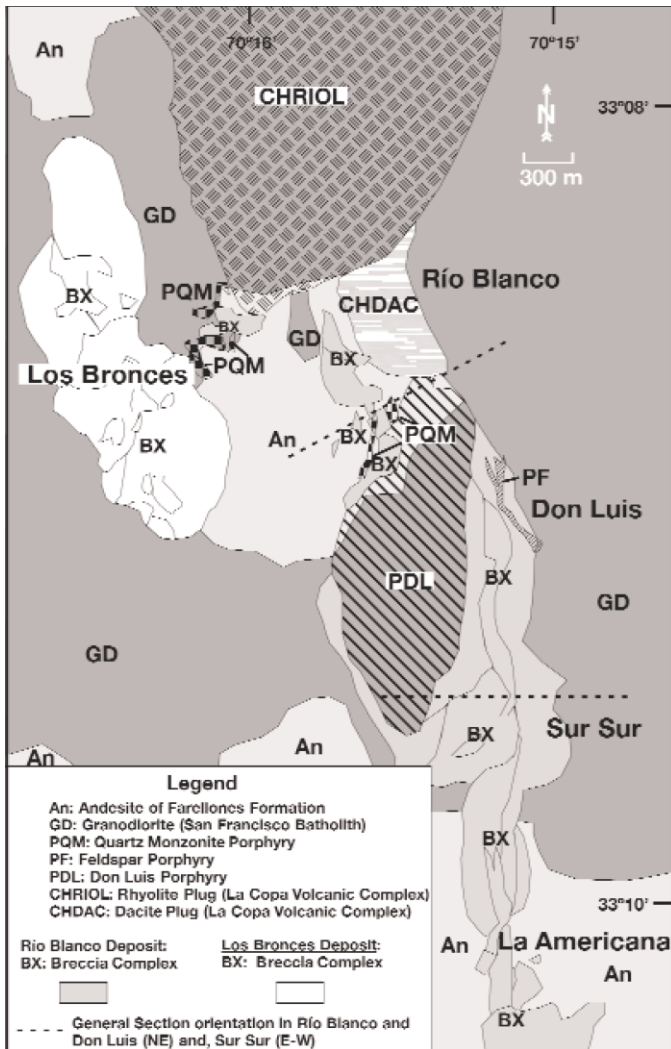


Figura 3: Geología del distrito Andina (Deckart et al. 2005).

Se considera que la historia hidrotermal del complejo Río Blanco-Los Bronces comenzó con el desarrollo de un extenso sistema de alteración, en gran parte en rocas granitoides, caracterizado por conjuntos de actinolita-magnetita ± clinopiroxeno ± titanita ± plagioclasa, con vetas y cementos de brechas mineralógicamente similares (Skewes et al., 1994, 2003). Esta asociación, que implica metasomatismo de Fe, es similar en muchos aspectos a la documentada en el yacimiento de pórfito de Cu-Mo-Au de Island Copper, en la Columbia Británica, por Arancibia y Clark (1995) y comparte su escasez o ausencia de sulfuros. El primer evento de mineralización económica postulado por Serrano et al. (1996) coincidió con una intensa alteración potásica, dominante biotita, tanto de andesitas como de rocas granitoides, centrada en el sector de Río Blanco. La alteración de biotita ± magnetita ± sulfuros ± feldespato se asoció con el desarrollo de un stock de vetas mineralógicamente similares, en las que la calcopirita está acompañada de bornita, pirita y

Introducción

molibdenita en menor medida. El complejo de brechas de Río Blanco (por ejemplo, la Fig. 3A), estrechamente con la alteración de los silicatos K, comprende enjambres de

1.3.3 Distrito Minero Chuquicamata

El yacimiento de Chuquicamata corresponde a un pórfito cuprífero que está alojado en rocas intrusivas del Terciario, vinculadas al emplazamiento de complejos intrusivos cenozoicos. Las rocas encajantes y que contienen la mineralización corresponden a tres unidades porfidíticas, con diferentes texturas y cantidades variables de plagioclasa, cuarzo, ortoclasa y biotita. Estas unidades son las denominadas:

- Pórfito Este, granodiorítico a monzodiorítico, con abundantes fenocristales apretados y matriz escasa. Concentra la mayor parte de los minerales de mena.
- Pórfito Oeste, monzogranítico a granodiorítico, con fenocristales espaciados y matriz sacaroidal; y
- Pórfito de Banco, monzodiorítico, con una distribución de tamaños bimodal de fenocristales en una matriz afanítica (Aracena, 1981). El rango de edad en el que se emplazan estas unidades varía entre 35,6 y 33,6 Ma (U-Pb en círculo; Ballard et al., 2001).

Chuquicamata se relaciona espacial y temporalmente con el Sistema de Fallas de Domeyko (DFZ), específicamente con la Falla Oeste (Ossandón et al., 2001). Esta falla, subvertical y de rumbo aproximadamente N-S, corresponde al contacto del bloque mineralizado en su pared oeste con la Granodiorita Fiesta. La roca encajante corresponde a intrusivos más antiguos cuyas edades no han sido establecidas con certeza.). Asimismo, existen afloramientos de rocas estratificadas mesozoicas (metasedimentitas y metavolcanitas: Formación Caracoles, Lindsay, 1997), y depósitos cuaternarios. La distribución de las diferentes unidades, tanto en el interior como en el exterior del pozo, puede verse en la figura siguiente (Astudillo et al. 2008).

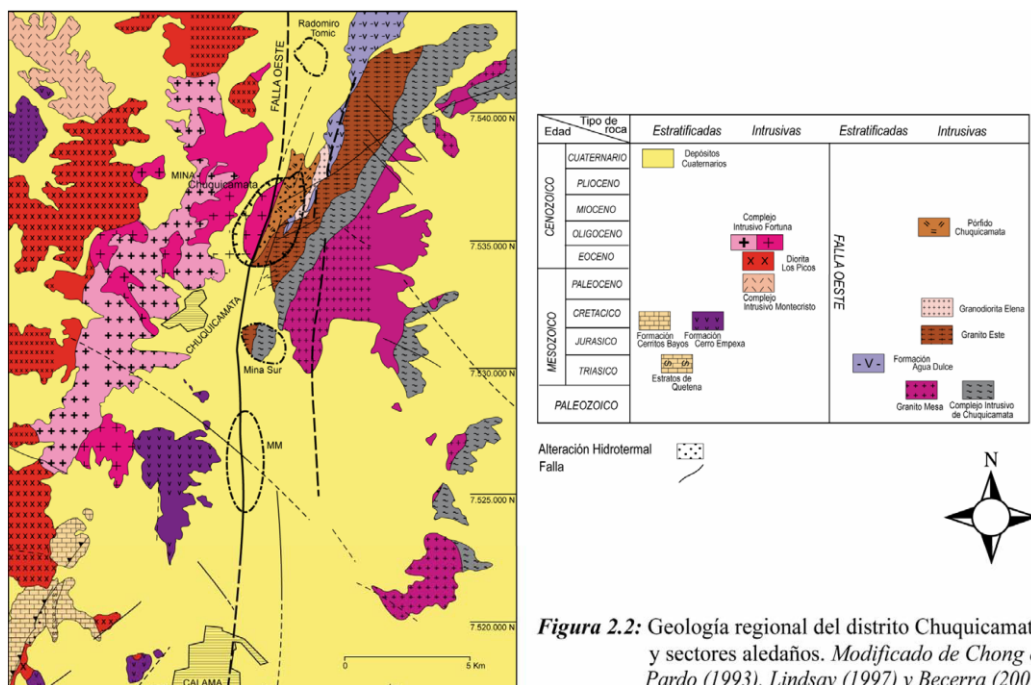


Figura 2.2: Geología regional del distrito Chuquicamata y sectores aledaños. *Modificado de Chong & Pardo (1993), Lindsay (1997) y Becerra (2001)*

Figura 4: Geología del distrito Chuquicamata (Astudillo et al. 2008).

1.4 Objetivos

1.4.1 Objetivo general

- Aportar al conocimiento sobre el proceso de estallido de rocas en condiciones de deformación dinámica en yacimientos de tipo stockwork.

1.4.2 Objetivos específicos

- Comprender las variaciones de las propiedades mecánicas de las rocas con vetillas pertenecientes a faenas mineras subterráneas en pórfidos cupríferos.
- Comprender los patrones de fracturamiento a distintas condiciones de stress in-situ.
- Comprender el proceso del estallido de rocas a partir de ensayos de laboratorio a pequeña escala.

1.5 Alcances

Las siguientes limitaciones se han adoptado durante el desarrollo de este estudio con el fin de ceñir la discusión y conclusiones a los ensayos realizados:

- i. Las muestras de rocas corresponden a litologías específicas que fueron proveídas desde la compañía para el desarrollo del estudio, y no fueron seleccionadas bajo algún criterio en específico. Estas corresponden a:
 - a. Andesitas basálticas del Complejo Máfico El Teniente (CMET), desde la mina El Teniente.
 - b. Granodiorita del intrusivo Rio Blanco, desde la mina Andina. (RB)
 - c. Rocas de alteración Cuarzo-Sericita (QS-QIS, QS-QMS), desde la mina Chuquicamata. QIS significa cuarzo igual a sericita, mientras que QMS significa cuarzo mayor a sericita.
- ii. Debido a la disponibilidad de muestra de roca de Granodiorita (RB) y Cuarzo-Sericita (QS), con ellas sólo se han realizado ensayos desconfinados en muestras cilíndricas. Por su parte, se han realizado ensayos desconfinados en muestras cilíndricas y confinados en muestras cúbicas de CMET.
- iii. El análisis sobre el proceso de fractura corresponde a uno del tipo cualitativo, a través de una cámara de alta velocidad. Se realiza describiendo sólo el campo visible por la cámara, por lo que es una descripción parcial. Una descripción cuantitativa para este tipo de ensayos normalmente incluye una cámara de alta velocidad adicional, además del procesamiento de la muestra mediante una tomografía computarizada de rayos-X, que permite obtener superficie de fracturas y orientaciones preferenciales.
- iv. El problema de escalabilidad del macizo rocoso no se ha abordado en este estudio debido a que no es uno de los objetivos principales. Por otra parte, existen limitaciones técnicas de los equipos al realizar ensayos en muestras mayores a 50mm de largo.

1.6 Metodología

Las muestras se sometieron a cargas dinámicas y altas tasas de deformación mediante el uso de una barra de presión dividida de Hopkinson, para el caso desconfinado, y una barra de Hopkinson triaxial, para los casos de confinamiento uniaxial y biaxial. El proceso de fractura se capturaron mediante una cámara de alta velocidad. Finalmente, se discuten las implicancias del análisis dinámico, en términos de la evaluación de estallidos de rocas del tipo strainburst en excavaciones subterráneas profundas. La metodología que se adoptó para el desarrollo del presente estudio se indica en el siguiente esquema (Figura 5). Cada una de las etapas es descrita en los apartados 1.5.1 al 1.5.3.

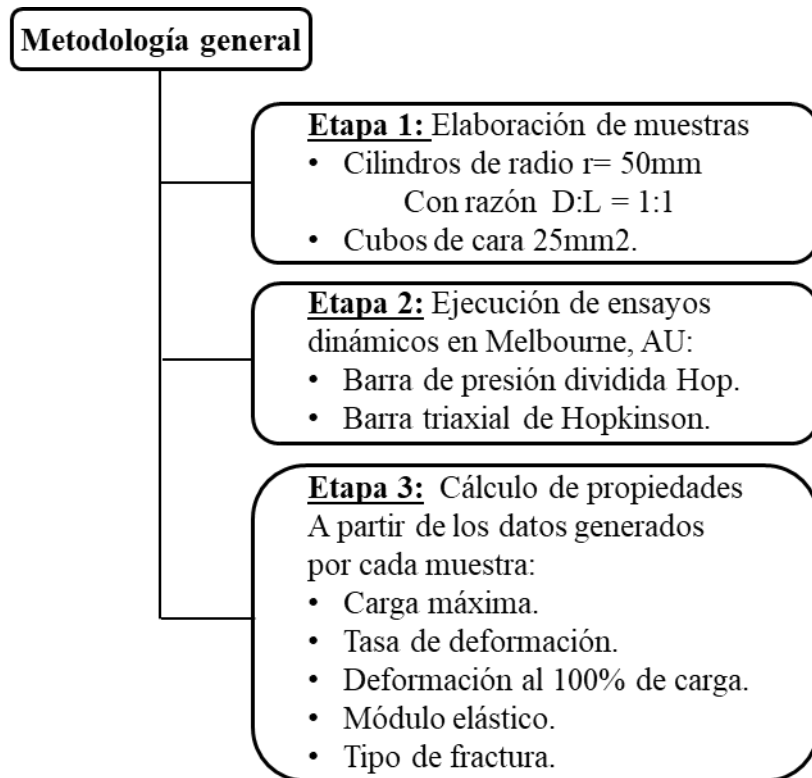


Figura 5 - Esquema sobre la metodología adoptada durante el estudio.

1.6.1 Etapa 1: Elaboración de muestras

La elaboración de muestras considera la disponibilidad de tres equipos fundamentales: Testiguera, Sierra de roca, y Rectificadora de superficies.

El primer paso consiste en el uso de una testiguera para la obtención de cilindros. Se debe utilizar un cabezal de 2" de diámetro interior para los cilindros a utilizar en ensayos desconfinados, mientras que para los cilindros de los ensayos confinados se debe utilizar un cabezal de 3".

El segundo paso corresponde a cortar mediante una sierra de roca todos los cilindros de manera que su largo L sea igual a 50mm.

El tercer paso corresponde al uso de la rectificadora. En el caso de muestras cilíndricas para pruebas desconfinadas, se utilizan cilindros diámetro D= 2" y largo L=2", obteniendo una razón de esbeltez

Introducción

L:D igual 1. La rectificadora se utiliza para asegurar el paralelismo de las dos caras planas del cilindro.

Para obtener las muestras cúbicas se deben desbastar los cilindros de diámetro D=3" y largo L=2". Es decir, se utiliza una rectificadora para que, mediante el desbastado de la superficie curva o lateral del cilindro, se formen cuatro caras perpendiculares, aprovechando el sistema de fijación que regularmente se utiliza en la rectificadora, para asegurar tanto paralelismo como perpendicularidad a las caras, en la secuencia indicada en el esquema de la figura siguiente.

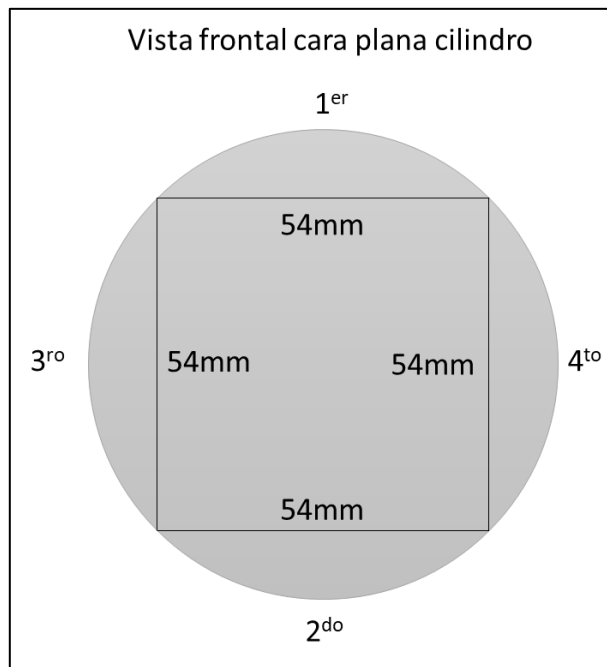


Figura 6 Secuencia de pulido para obtención de muestras cúbicas a partir de un cilindro D=3" y L=50mm.

El resultado del desbastado inicial corresponde a un paralelepípedo de largo 50mm, con caras cuadradas de arista 54mm. Se debe finalizar desbastando cuidadosamente 4mm de cada una de las caras, obteniendo un cubo con aristas de 50mm.

1.6.2 Etapa 2: Ejecución de ensayos dinámicos

Los ensayos fueron realizados en el laboratorio Monash GeoExtremes Lab (MGE) en Melbourne, Australia. Los dispositivos utilizados corresponden a una Split Hopkinson Pressure Bar (SHPB), utilizada para ensayos dinámicos desconfinados, y una Triaxial Hopkinson Bar (THB), utilizada para ensayos dinámicos confinados.

1.6.2.1 *Split Hopkinson Pressure Bar*

Se ensayaron un total de 35 muestras cilíndricas para los ensayos de compresión uniaxial desconfinados (Figura 7). Las muestras corresponden 12 a CMET, 13 a RB y 10 a CHQ. El diámetro de la muestra se fijó en 50 mm. La relación de esbeltez elegida es 1: 1 para minimizar los efectos de fricción e inercia (Q. B. Zhang y Zhao, 2014). Además, las muestras se rectificaron para

Introducción

que la perpendicularidad fuera inferior a 0,02 mm en 25 mm (0,1%). La superficie lateral es recta con una diferencia máxima de 0,02 mm en toda la muestra.

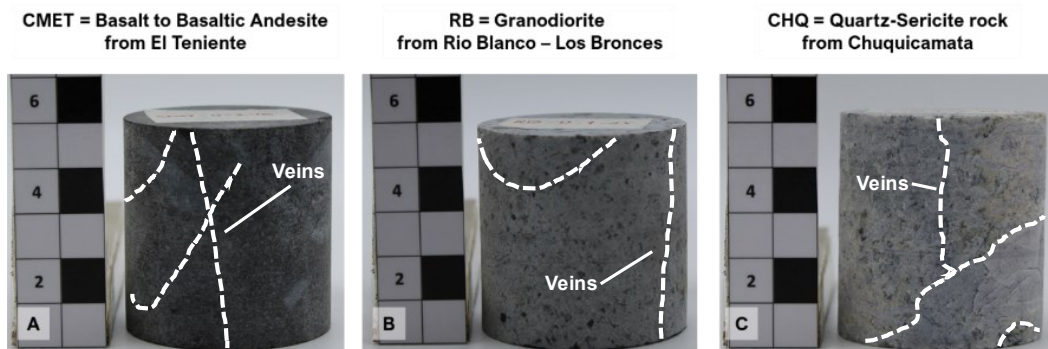


Figura 7: Muestras cilíndricas para ensayos desconfinados.

En este trabajo, se ensayaron muestras de roca utilizando un sistema SHPB, situado en la Universidad de Monash (J. Li et al., 2021; Q.-B. Zhang et al., 2021). El SHPB se compone de una barra de percusión (7850 kg/m³, o 210 GPa, 50 mm), una barra de incidencia y transmisión (50 mm), y una muestra intercalada. Se utiliza una pistola de gas para las barras de golpeo por impulso. Hay un amortiguador para absorber el impacto de la barra transmitida. Un dispositivo de adquisición de datos (NI PXIE 5105, frecuencia de muestreo de 1 MHz) recoge la señal de dos galgas extensométricas (FLA-6-11) instaladas en las barras incidente y de transmisión, respectivamente (Figura 8).

Las pruebas comienzan cuando la pistola de gas se carga a la presión deseada. Una vez disparada, la barra de percusión se desplaza hacia la barra incidente, donde se produce una onda incidente (ϵ_i) durante el impacto. Ésta se transmite a través de la barra hasta la muestra, y la interacción da lugar a una onda de transmisión (ϵ_t) y otra de reflexión (ϵ_r). Los ensayos se realizan a diferentes velocidades de impacto, que van de 5 a 18 m/s.

Introducción

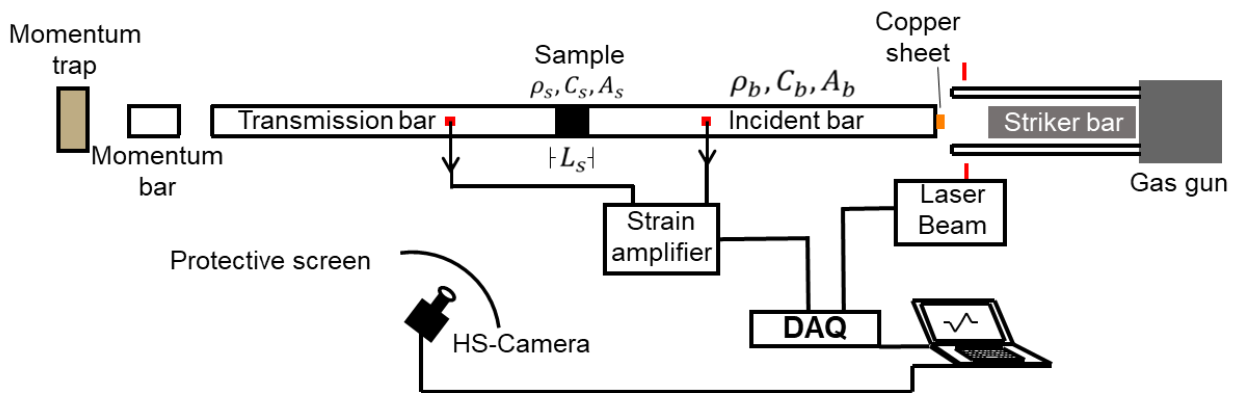


Figura 8: Split Hopkinson Pressure Bar en Monash Geoextremes, Universidad de Monash, Melbourne, AU.

Se utilizó una cámara de alta velocidad de la marca Phantom V2511 (resolución de 256x256 píxeles a 200.000 fotogramas por segundo (fps)), para estudiar el patrón de fractura experimentado durante la deformación dinámica. En ese sentido, en este estudio se utilizaron tres categorías principales ampliamente aceptadas para describir los patrones de fractura (Q.B. Zhang y Zhao, 2014)

- 1) cuasi-elástica o aparentemente intacta (Figura 9a): no hay nuevas grietas visibles en la muestra de roca.
- 2) La muestra está agrietada o dividida por una sola fractura (Figura 9b): la muestra analizada se recupera con nuevas grietas visibles a lo largo de las vetas, o de la matriz de la roca, y normalmente se pueden ver "parches blancos". Las manchas blancas están relacionadas con el desarrollo de zonas de microfisuración y se observan antes del crecimiento de las fracturas visibles (X. Li et al., 2017; Wong y Einstein, 2009).
- 3) el nivel de fracturación fragmentada o múltiple (Figura 9c). Aquí, la muestra ensayada pierde su capacidad de carga debido a la repentina fragmentación o ruptura a lo largo de múltiples vetas y/o masa de tierra.

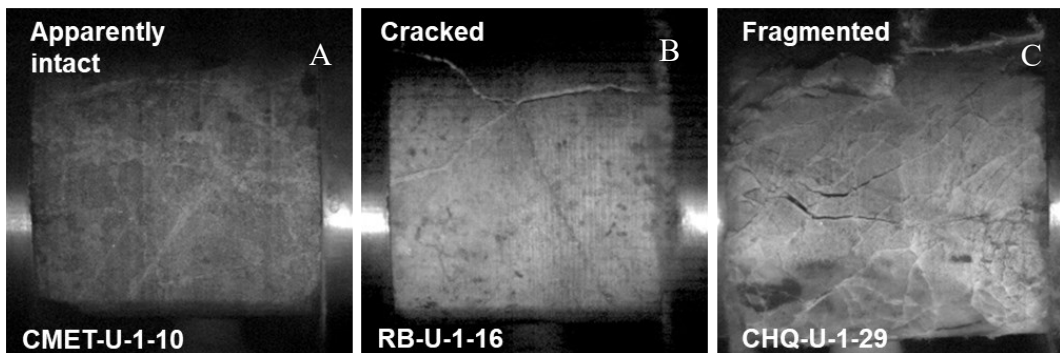


Figura 9 Fracture patterns (a) Quasi-elastic or apparently intact. (b) Cracked or split by single vein. (c) Fragmented or multiple fracturing.

1.6.2.2 Triaxial Hopkinson Bar

Se fabricaron un total de 8 muestras cúbicas con un volumen de $50 \times 50 \times 50 \text{ mm}^3$, para cumplir la recomendación de tamaño medio (Y. X. Zhou et al., 2012). Las muestras están rectificadas y el paralelismo de las caras opuestas es inferior a 0,02 mm en 25 mm. Se cumple la perpendicularidad entre superficies adyacentes. La figura 10 indica dos muestras diferentes con litología similar pero con diferentes tipos de vetas, lo que implica una anisotropía.

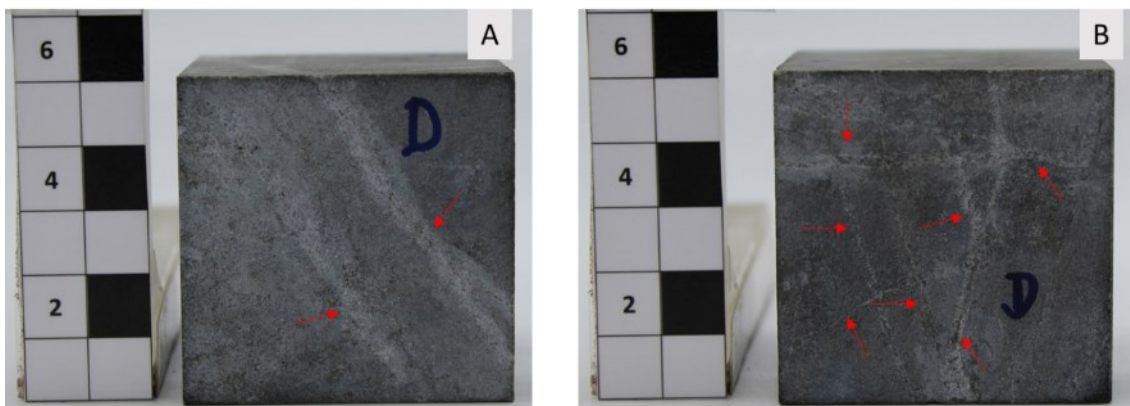


Figura 10: Muestras Cúbicas para ensayos dinámicos confinados.

En este trabajo, utilizamos una barra triaxial de Hopkinson (THB) en la Universidad de Monash , como la que se muestra en la Figura 10 superior (K. Liu et al., 2019b, 2020; Q. B. Zhang & Zhao, 2014). El aparato consiste en un sistema de carga dinámica, que incluye una pistola de gas, un módulo de rayo láser para las mediciones de velocidad, una barra de percusión ($= 7850 \text{ kg/m}^3$, $= 210 \text{ GPa}$, $= 40\text{mm}$, velocidad de impacto de hasta 50 m/s), y tres pares independientes de barras cuadradas de acero (sección transversal $50 \times 50 \text{ mm}^2$) alineadas ortogonalmente en tres direcciones (XYZ): las barras de percusión, incidente y de transmisión en la dirección X, dos barras de salida en la dirección Y, y dos barras de salida en la dirección Z.

Aunque se puede obtener un estado de pretensión triaxial puro utilizando el THB, también se pueden conseguir estados de pretensión biaxiales y uniaxiales. El estado triaxial in situ en una muestra cúbica se consigue utilizando dos cilindros hidráulicos que cargan las barras incidentes y transmitidas en la dirección X y las barras de salida en la dirección Y, mientras que un cilindro

Introducción

hidráulico vertical carga las barras de salida en la dirección Z. La carga dinámica puede aplicarse de modo que la barra percutora se desplace hacia la barra incidente. La velocidad de la barra percutora se mide con el módulo de rayo láser justo antes del impacto. Se coloca un disco de cobre rojo en la cara de impacto de la barra incidente para dar forma de onda sinusoidal al impulso (Y. X. Zhou et al., 2012).

Para la prueba, se coloca una muestra cúbica en la célula de carga en la intersección del eje XYZ. Una vez que gatilla la pistola de gas, la barra de percusión se mueve hacia la barra incidente, golpeándola, por lo que se produce una onda incidente durante el impacto. Ésta se transmite a través de la barra a la muestra, y la interacción da lugar a una onda de transmisión y otra de reflexión en la dirección X, y a ondas transmitidas en la dirección Y. Todas las ondas se miden con gomas extensométricas, como se muestra en la figura 11 en la parte inferior.

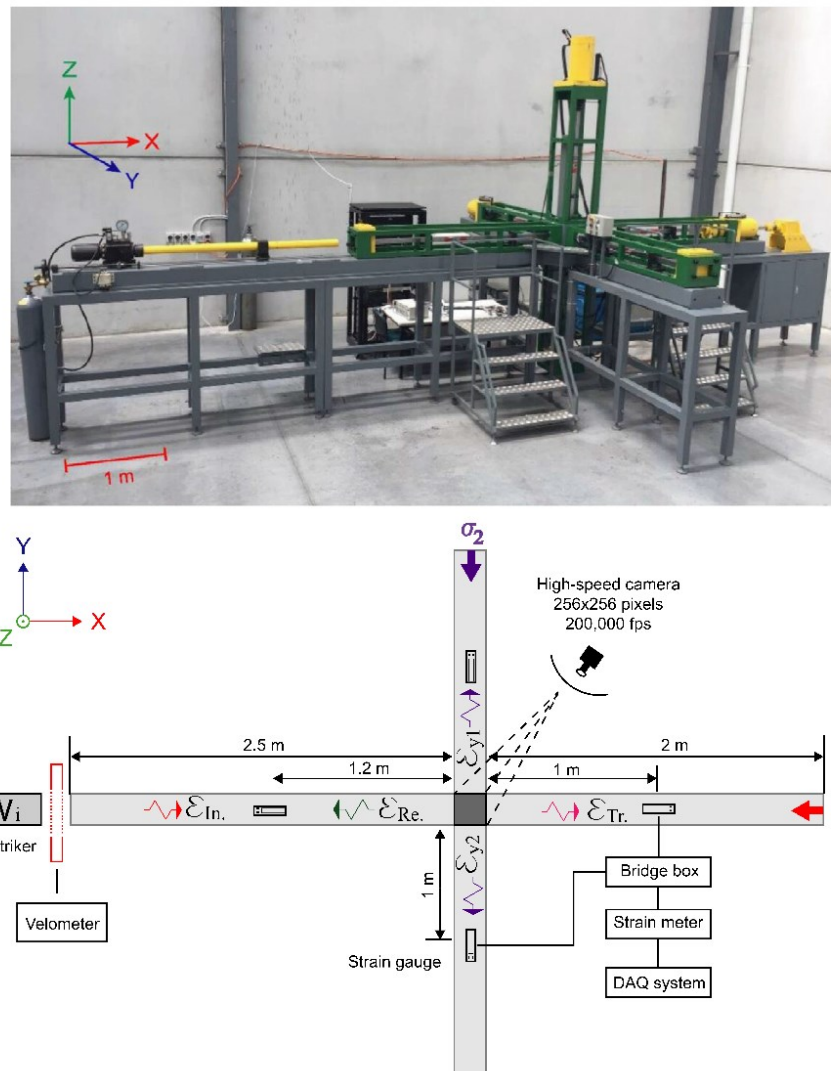


Figura 11: Triaxial Hopkinson Bar en la Universidad de Monash (arriba). Esquema de la configuración típica utilizada en una prueba de compresión dinámico en una barra triaxial (abajo).

Para estudiar el patrón de fractura experimentado por la muestra durante la deformación dinámica, utilizamos una cámara de alta velocidad, la CMOS Phantom V2511 (resolución de 256x256 píxeles, 200.000 fotogramas por segundo (fps)).

1.6.3 Etapa 3: Comportamiento dinámico muestras ensayadas

1.6.3.1 Procesamiento de datos: ensayos desconfinados

El sistema de adquisición de datos utilizado en este estudio corresponde a un sistema de adquisición de datos (DAQ) de alta velocidad, el National Instruments (NI) PXIe-1078, con una ranura de 8 canales, mientras que la velocidad de muestreo es de 1 MHz. Los datos capturados de onda incidente (i), transmitida (t) y reflejada (r) se procesan para cada prueba. De acuerdo con la teoría de ondas de tensión unidimensional (Q. M. Li & Meng, 2003), se utilizan las siguientes ecuaciones para los cálculos:

$$\sigma(t) = \frac{A_b E_b}{2A_s} [\varepsilon_i(t) + \varepsilon_t(t) + \varepsilon_r(t)] = \frac{A_b E_b}{2A_s} \varepsilon_{tr}(t) \quad (1)$$

$$\varepsilon(t) = \frac{C_b}{L_s} \int_0^t [\varepsilon_{in}(t) - \varepsilon_{tr}(t) - \varepsilon_{re}(t)] dt = \frac{C_b}{L_s} \int_0^t \varepsilon_{tr}(t) dt \quad (2)$$

$$\dot{\varepsilon}(t) = \frac{C_b}{L_s} [\varepsilon_{in}(t) - \varepsilon_{tr}(t) - \varepsilon_{re}(t)] = \frac{-2C_b}{L_s} \varepsilon_{re}(t) \quad (3)$$

Donde $\sigma(t)$ es el esfuerzo de compresión axial en la muestra en función del tiempo, A_b es la superficie de sección de las barras, E_b es el módulo de Young de las barras (210 GPa) y C_b es la velocidad de onda de las barras (5200 m/s). Los parámetros A_s y L_s son la longitud y el área de la muestra, respectivamente. Los parámetros $\varepsilon_i(t)$, $\varepsilon_t(t)$, $\varepsilon_r(t)$ corresponden a la deformación y los subíndices "i", "t" y "r" se refieren a las ondas incidente, transmitida y reflejada, en ese orden. El parámetro $\dot{\varepsilon}(t)$ corresponde a la tasa de deformación durante la prueba. En la figura 12 se muestra una señal típica de la prueba

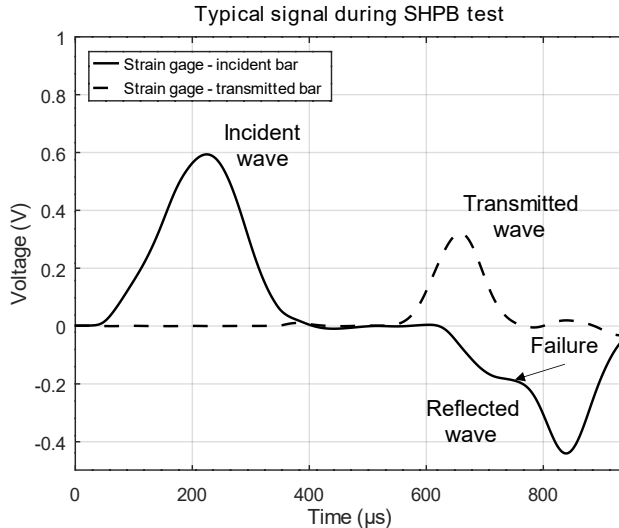


Figura 12. Señales de onda típicas: incidente ε_i , transmitida ε_t y reflejada ε_r , durante una prueba de compresión uniaxial dinámica mediante una SHPB cuya velocidad de impacto es 15 m/s. El momento de falla de la muestra se observa en la onda reflejada mediante un cambio en la pendiente, tal como se indica.

Para validar los resultados de cada ensayo de compresión dinámica, debe verificarse el balance de cargas, el cual se consigue una vez que las tensiones medidas en ambos extremos de la muestra son casi iguales (Q. B. Zhang y Zhao, 2014). En la Figura 13 superior, se representa gráficamente el

Introducción

equilibrio de tensiones en un ensayo típico. Aquí, el equilibrio se alcanza una vez que la tensión de la onda incidente más la reflejada es equivalente a la de la onda transmitida, es decir:

$$\sigma_{in}(t) + \sigma_{re}(t) = \sigma_{tr}(t).$$

Utilizando las ecuaciones (1), (2) y (3), la curva tensión-deformación puede ser trazada como se muestra en la Figura 13 inferior. El peak de esta curva tensión-deformación corresponde a la compresión dinámica uniaxial o carga máxima (σ_{ucd}).

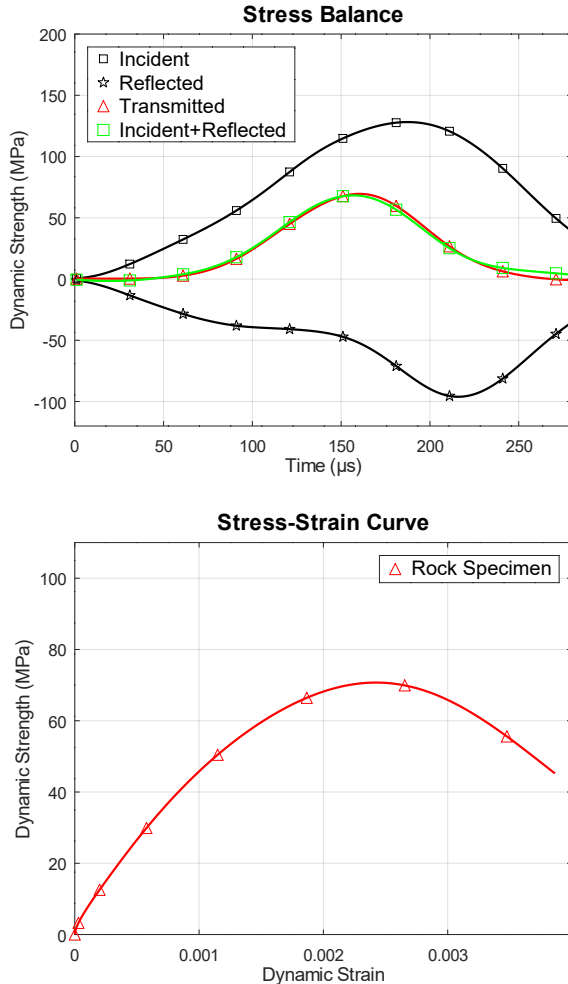


Figura 13. Superior: Equilibrio de cargas $\sigma_i(t) + \sigma_r(t) = \sigma_t(t)$. Subíndices i para incidente, r para reflejada, y t para transmitida. Abajo: Curva de carga-deformación para la determinación de la resistencia a la compresión uniaxial dinámica. (σ_{ucd}).

1.6.3.2 Procesamiento de datos: Ensayos confinados

Las ondas incidente (ε_{In}), transmitida (ε_{Tr}) y reflejada (ε_{Re}) se miden mediante galgas extensométricas instaladas en las barras de incidencia y transmisión. Estos datos de las ondas se procesan para cada ensayo y permiten reconocer los picos de carga, la deformación y las tasas de deformación, como se muestra en la figura3. Utilizando ε_{In} , ε_{Tr} y ε_{Re} :

$$\sigma_x(t) = \frac{A_b E_b}{2A_s} [\varepsilon_{In}(t) + \varepsilon_{Tr}(t) + \varepsilon_{Re}(t)] = \frac{A_b E_b}{2A_s} \varepsilon_{Tr}(t) \quad (4)$$

$$\varepsilon_x(t) = \frac{C_b}{L_s} \int_0^t [\varepsilon_{In}(t) - \varepsilon_{Tr}(t) - \varepsilon_{Re}(t)] dt = \frac{C_b}{L_s} \int_0^t \varepsilon_{Tr}(t) dt \quad (5)$$

$$\dot{\varepsilon}_x(t) = \frac{C_b}{L_s} [\varepsilon_{In}(t) - \varepsilon_{Tr}(t) - \varepsilon_{Re}(t)] = \frac{-2C_b}{L_s} \varepsilon_{Re}(t) \quad (6)$$

$$\sigma_y(t) = \frac{A_b E_b}{2A_s} [\varepsilon_{y1}(t) + \varepsilon_{y2}(t)] \quad (7)$$

$$\varepsilon_y(t) = \frac{C_b}{L_s} \int_0^t [\varepsilon_{y1}(t) + \varepsilon_{y2}(t)] dt \quad (8)$$

Donde $\sigma_x(t)$ es la tensión de compresión axial en función del tiempo t, A_b es la superficie de sección de las barras, E_b es el módulo de Young de las barras, C_b es la velocidad de onda en las barras, y L_s y A_s son la longitud y el área de la muestra. El parámetro ε_x corresponde a la deformación y los subíndices In, Re y Tr se refieren a las ondas incidente, transmitida y reflejada en la dirección X, respectivamente. En este estudio los valores de compresión son positivos, luego las tensiones previas y la resistencia a la compresión dinámica también lo son. En la figura 14 se muestra un ejemplo de interpretación del estado de pretensión biaxial (40,30,0) en un ensayo de barra triaxial de Hopkinson.

La señal típica obtenida de las galgas extensométricas en la dirección X del impacto se representa en la Figura 14a, donde se miden las ondas Incidentes (in), Transmitidas (Tr) y Reflejadas (Re). El valor medio de 43 MPa indicado en la etapa de descarga de la onda incidente es el resultado de la interacción entre la barra incidente y el dispositivo de reacción de la cuña por el impacto de la barra percutora (Hokka et al., 2016; K. Liu et al., 2019a; H. Wang et al., 2021; Yang et al., 2020). El espécimen de roca bajo carga biaxial pretensada se deforma debido a la carga dinámica, y se puede medir una onda transmitida en la dirección Y debido al efecto de Poisson y al confinamiento, como se muestra en la Figura 14b.

Para validar los resultados de cada ensayo de compresión dinámica en un SHPB, debe comprobarse la uniformidad de la deformación de la muestra (Q. B. Zhang y Zhao, 2014). Del mismo modo, debe comprobarse durante un ensayo de barra Hopkinson triaxial, como se indica en la Figura 14c, aunque la concentración de tensiones en las esquinas (X. Li et al., 2017). Así, dado un ensayo THB, el equilibrio de tensiones se alcanza cuando las tensiones medidas en ambos extremos de la muestra son casi iguales, según la siguiente la ecuación $\sigma_{In}(t) + \sigma_{Re}(t) = \sigma_{Tr}(t)$. Como se muestra en la Figura 14c, el equilibrio de tensiones se alcanza bien en torno a 65 μ s hasta 90 μ s, antes del fallo de la muestra. La tensión total aplicada durante la carga dinámica en cada dirección a la muestra se muestra en la Figura 12d, donde el valor máximo para la dirección X es de 231 MPa y la dirección Y es de 59 MPa, y ambos consideran la carga estática (40,30,0) y la carga dinámica ($\sigma_x(t), \sigma_y(t), 0$). A continuación, las figuras 14 e,f muestran las curvas de tensión-deformación dinámicas de la muestra, calculadas según las ecuaciones (4) a (9).

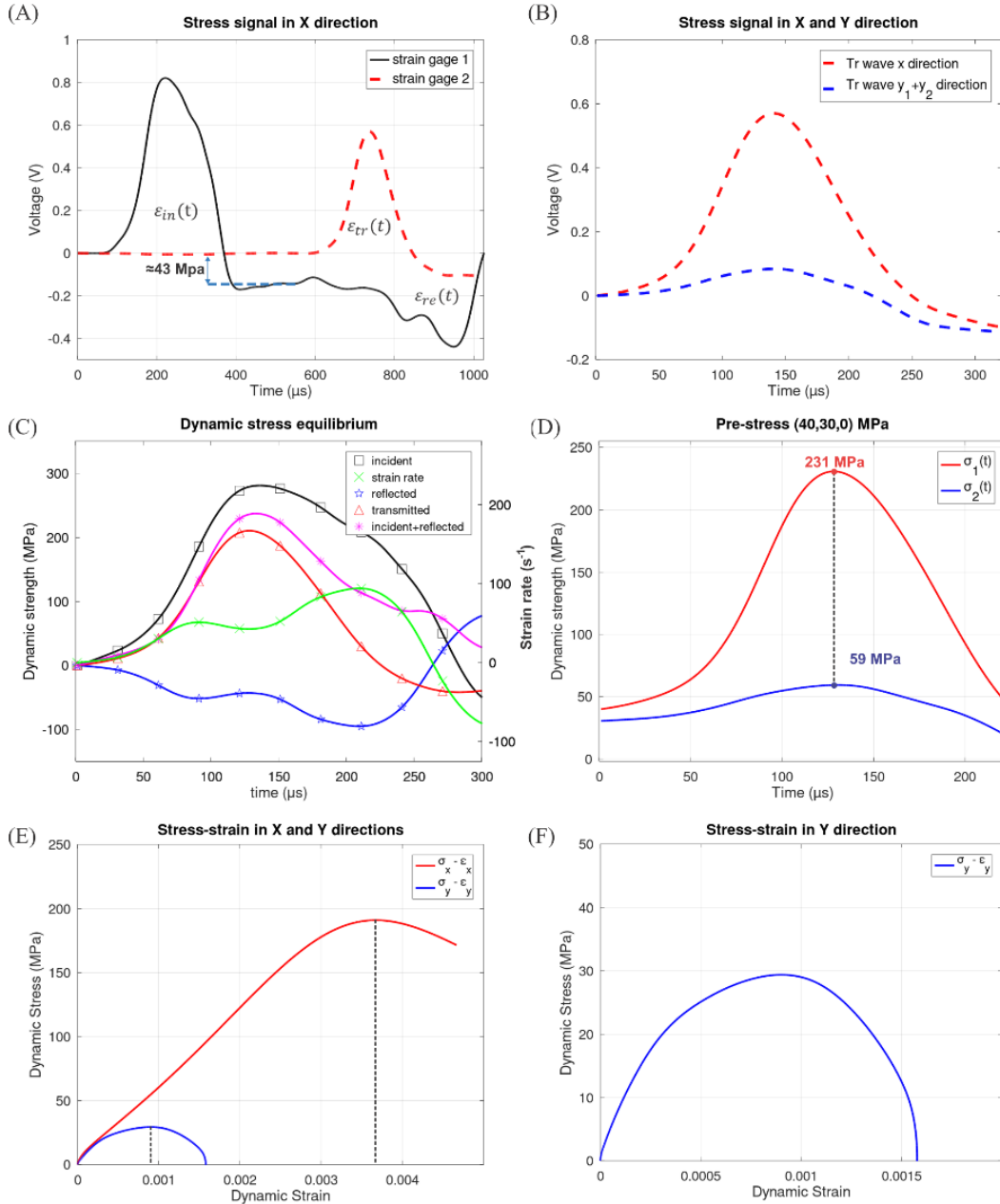


Figura 14 Resumen de los datos obtenidos de un ensayo dinámico utilizando una THB. En esta figura, la pre-tensión equivale a (40,30,0). (a) Onda incidente ε_{inx} , transmitida ε_{trx} y reflejada ε_{rex} . El momento en que ocurre la fatiga del material se reconoce en la onda reflejada. (b) Onda transmitida en la dirección X (rojo) y dirección Y (azul). (c) equilibrio de esfuerzos en los extremos de la muestra en la dirección X. (d) Esfuerzo total dinámico aplicado a la muestra (pre-tensión + tensión dinámica). (e) Esfuerzo dinámico vs deformación dinámica en la dirección X (rojo) y dirección Y. (f) Esfuerzo dinámico vs deformación dinámica en la dirección Y.

1.7 Resumen de la investigación

Los resultados del estudio son presentados en los siguientes artículos:

Artículo 1: Franco Robbiani, Kai Liu, Qian-Bing Zhang, Luis Felipe Orellana, Dynamic uniaxial compression testing of veined rocks under high strain rates, International Journal of Rock Mechanics and Mining Sciences, Volume 153, 2022, 105085, ISSN 1365-1609, <https://doi.org/10.1016/j.ijrmms.2022.105085>.

Artículo 2: Robbiani, F., Orellana, L.F., Liu, K., Zhang, Q.B. (2021). Dynamic mechanical properties of veined rocks from El Teniente Mine in Chile under confined and unconfined conditions. Article to be submitted to the International Journal of Rock Mechanics and Mining Sciences.

2 Artículo 1: Dynamic uniaxial compression testing of veined rocks under high strain rates

Franco Robbiano^{1,2,3}, Kai Liu^{4,5}, Qian-Bing Zhang⁴, Luis Felipe Orellana^{1,3,*}

¹ Department of Mining Engineering, FCFM - University of Chile, Chile

² Department of Geology, FCFM - University of Chile, Chile

³ Advanced Mining Technology Center (AMTC), FCFM - University of Chile, Chile

⁴ Department of Civil Engineering, Monash University, VIC 3800, Australia

⁵ Department of Engineering Science, University of Oxford, Parks Road, OX1 3PJ, United Kingdom

ABSTRACT

The occurrence of strainbursts is of major concern in underground deep mining operations. Strainbursts are complex events characterized by a spontaneous strain-energy liberation at the boundaries of underground excavations, putting both the long-term safety of operations and exposing workers to risk. In this study, we reported a series of uniaxial compression tests by using a split Hopkinson pressure bar (SHPB) and a high-speed camera, to understand the role of dynamic loads and high strain rates (10 to 102 s⁻¹) in the mechanical behavior and the fracture patterns of veined rocks. The samples are representative of major deep underground mine districts in Chile: Chuquicamata (QS), Andina (RB), and El Teniente (CMET). Results show a clear increase in the dynamical uniaxial strength concerning quasi-static values. The increase was up to 2,2 times in CMET, 1,8 in RB, and 2,6 in QS. Additionally, the dynamic increase factor (DIF) indicates a strong strain rate dependency of the QS samples. This effect on RB and CMET samples is less evident. The data obtained with dynamic compressional testing indicates that both the increase in stiffness and dynamical compressive strength depends largely on the rock strain rate dependency. Further, we report a direct relationship between fracture patterns and the presence of veinlets. We suggest that fractures propagate through the matrix when the mechanical properties show a strong strain rate dependency, whereas are restricted to veinlets and veins when this dependence is less evident. Thus, as stress pulses enhance the stiffness, the energy dissipation increases, and the proneness of block formation is higher. These are conditions favoring strainbursts occurrence and might increase the severity of this phenomena in underground excavations.

1. INTRODUCTION

The increasing demand for metal commodities is leading to a market pressure, and the need of ensuring both reserves and resources of metal-bearing minerals. It is assumed that superficial ore bodies have already been discovered, and it is expected that most future mines will be deeper and become underground. Given that underground mining is a suitable solution for metal production, one of the main concerns is the increase in investment and operational costs due to deeper excavations and associated risks. For example, mining operations in world-class copper-molybdenum porphyries, such as Chuquicamata, Andina, and El Teniente mines in Chile, are currently exploited deeper underground by using block and panel mining methods. Several geotechnical challenges are identified under these conditions: Higher¹ and local stress concentrations due to mining perturbations, reactivation of geological faults and inducing seismicity in the surrounding areas^{2–5}, but also a major role of discontinuities (such as joints and veins) in the behavior and mechanical properties of the rock mass^{6–8}.

Copper-molybdenum rocks are far from continuous and homogeneous, and are often characterized by the presence of different types of veins and veinlets^{9,10}. These veins and veinlets can be distributed spatially in three different structural styles: i) stockworks or disseminated in veinlets, ii) veins, and iii) hydrothermal breccias^{11–14}. For example, several rocks of the El Teniente mine complex corresponds to an assemblage of intact rocks bound by veinlets¹⁵ (Figure 1).

Veinlets (with a thickness of less than 1 cm) are the main feature for which these rocks are considered anisotropic, and the dynamic behavior of this type of rock is thus far partially unknown. In fact, most of the previous studies about the mechanical properties of veined rocks have been carried out under creep to quasi-static conditions in uniaxial and triaxial compressional tests^{16–18}, and indicate a strong influence on the peak strength relative to the veinlets direction with respect to the loading direction.

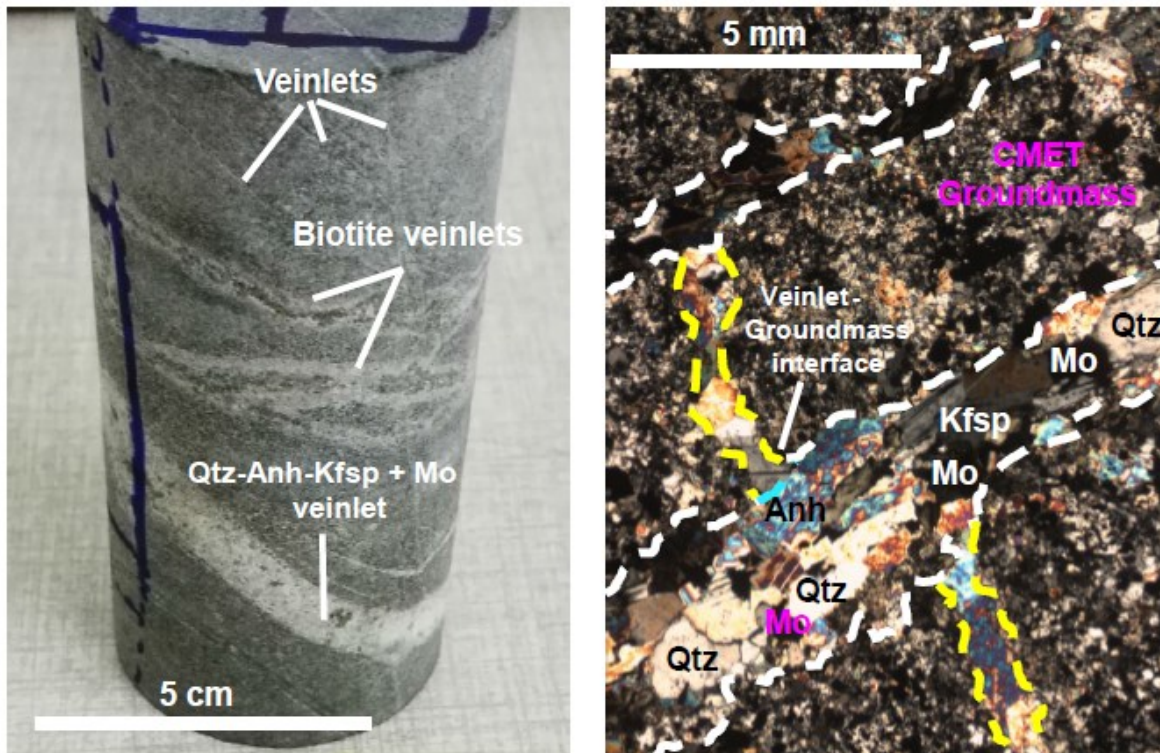


Figure 1 Left: A core sample from the copper-molybdenum porphyry in El Teniente Mafic Complex (CMET). The figure shows different types of veinlets in a stockwork structural configuration and the multiple geometrical relations among veinlets. Right: Thin section from a CMET sample, showing three different types of veinlets in the CMET groundmass. The main differences among veinlets rely on their infills, orientation, length and width.

Quasi-static experimental techniques use servo hydraulic machines to describe the static behavior of the rocks under strain rates ranging from 10^{-5} to 10^{-1} s^{-1} . Other techniques, such as the Hopkinson split-pressure bar (SHPB)^{19,20}, are used to study the dynamic behavior of rocks. With the SHPB, high strain rates from 10^1 to 10^4 s^{-1} are achieved, while decoupling the wave propagation and strain rate effects in the tested rocks. Experimental results regarding the SHPB technique show that dynamic strength values increase with increasing strain rate. Such a relationship is called rate dependence^{21–27}.

Several authors applied the SHPB technique to different rock types to understand the variation of strength with respect to strain rate. Studies about dynamic properties of rocks using SHPB, such as basalts^{28–30}, acid igneous,^{21,28,31–36} hydrothermal and metamorphic rocks^{37–42} suggest that mechanical and fracture behaviors under dynamic conditions are inherently different when compared to the same rock subjected to quasi-static load conditions^{21–25}. Reports indicate the enhancement of mechanical properties e.g., strength and fracture toughness, and variations in the fracture behaviors e.g., single fracture, multiple fracture, and pulverization. Furthermore, recent investigations into mechanical properties at high strain rates of anisotropic specimens of coal, granite, and shale^{36,43,44} indicates that mechanical properties are sensitive to the direction of bedding or microfracturing with respect to the loading axis. Despite great progress in the understanding of the dynamic properties, there is a lack of reports about the dynamic properties of rocks from copper-molybdenum porphyry mining, where multiple sources of dynamic loads coexist during the ore extraction operation.

Excavations in underground mining activities are affected by in-situ confining stresses (i.e., σ_1 , σ_2 , and σ_3) and the trajectories of induced static and dynamic loads. In particular, dynamic load sources can be related to man-made activities, such as mechanical vibrations (e.g., drilling), blasting, and natural (e.g., tectonic earthquakes) or induced seismic events. As a result, the underground mining excavations are subjected to evolving coupled static-dynamic states.^{45–51}.

In high-stress deep underground mining, the coupled static-dynamic state of the rock mass can result in the occurrence of strainburst. Strainburst corresponds to a sudden, violent damage event near an excavation boundary, usually associated with a seismic source, and is the most frequent mechanism of rockburst^{50,52–55}. Strainburst implies risk to mining operations: injuries to workers or fatalities, damage to mine infrastructure and equipment, time-consuming rehabilitation, and therefore production losses^{50,53}, and its assessment represents a major challenge.

Strainburst can be caused by a dynamic disturbance, predominantly by stress pulses or energy transfer from a remote seismic event. For instance, more than 100 of these events have been recorded since 1992 in the El Teniente mine⁵⁰. Different approaches, including empirical criteria^{56,57}, numerical simulations^{58,59}, mathematical algorithms⁶⁰ and artificial intelligence⁶¹ techniques have been carried out to understand rockburst potential. Moreover, laboratory tests have identified critical variables for strainburst potential (e.g. water content, loading rates, biaxial confinement, energy-storage capacity, among others) through both quasi-static and dynamic tests^{51,62–65}.

To better understand the influence of veinlets on the dynamic behavior of rocks, we performed a series of high strain rate tests on veined rocks from three major underground mining districts in Chile: Andina, Chuquicamata, and El Teniente. All these operations are run by Codelco, the Chilean State-owned company that is the world's largest copper mining producer⁶⁶.

This study aims to explore and describe the dynamic response rather than the quasi-static behavior of the rock. To this end, we present a series of dynamic compression tests to understand the dynamic response of veined rock samples under high strain rates (10 to 10^3 s⁻¹) by using a SHPB. Furthermore, to discuss the fracture process, we record each test using a high-speed imaging camera. Finally, the dynamic analysis based on the results of actual dynamic testing is discussed in terms of strainburst assessment for deep underground excavations.

2. MATERIALS AND METHODS

2.1. Samples

Rocks samples were obtained from three different major underground mines in Chile: 1) El Teniente mine, a Cu-Mo porphyry with estimated resources of $>96 \times 10^6$ metric tonnes of fine Cu in ore in central Chile¹⁴; 2) Andina mine, a Cu-Mo porphyry with estimated resources of >135 Mt of fine Cu, in central Chile, and 3) Chuquicamata mine, a Cu-Mo porphyry with estimated resources of $>63 \times 10^6$ metric tonnes, in northern Chile⁶⁶. It should be noted that traditional names of rock units are assumed in many long-established mines, although they are not necessarily related to reliable lithological description. These names are adopted in the article, though rock type of the samples used in this study is clarified.

Most of mineral resources in El Teniente mine are hosted by the El Teniente Mafic Complex (CMET) geological unit, or traditionally named “Mine Andesites”, which consist in a

pervasively biotite-altered and mineralized mafic intrusive complex composed of gabbros, diabases, and porphyritic basalts and basaltic andesites¹⁴. Our samples consist in basaltic andesites affected by veinlets (< 1 cm). In the Andina district, the Rio Blanco-Los Bronces porphyry is being exploited, and most of mineral resources are hosted by the San Francisco Batholith. The San Francisco Batholith consists in quartz monzonites, hornblende diorites and Rio Blanco and Cascada granodiorite¹³. Our samples are obtained from the Rio Blanco granodiorite. Finally, the Chuquicamata intrusive complex (CIC) hosts the Cu-Mo mineralization in the Chuquicamata district, and it is a composite intrusion formed by granodioritic to monzogranitic rocks. Main hydrothermal event is represented by quartz-sericite rock assemblage (QS)¹². The lithological variations of QS rocks are associated to the quartz content: Quartz equal Sericite (QIS) or Quartz major Sericite (QMS). The physical and mechanical properties of intact rock used in this study are obtained from other works on that lithologies^{15,67} and are summarized in Table 1.

Table 1: Physico-mechanical properties of rock samples used in this study. In parenthesis, the number of tested samples.

Properties	CMET ¹⁵	RB ⁶⁷	QS*
UCS (MPa)	92.5±14	150	67.2±19.6 (QIS) 76.5±23.7 (QMS)
Density ρ (g/cm^3)	2.82	2.66	2.7
Elastic Modulus E (GPa)	35.2±5.4	53	20 ±7.7 (QIS) 27 ±11.8(QMS)
Poisson's ratio ν	0.22±0,04	0.28	0.21±0.02 (QIS) 0.22±0.03 (QMS)

*Data provided by Chuquicamata Mine

2.2. Sample preparation

A total of 35 cylindrical specimens were prepared for dynamic uniaxial compression tests. They correspond 12 to CMET, 13 to RB and 10 to QS (see Figure 2). The diameter of specimen D_s is set to 50 mm. The slenderness ratio ($L_s:D_s \approx 1:1$) is chosen to minimize the effects of friction and inertia, but also to prevent damage to the test equipment given the stiffness of the rock samples^{22,55,68}. Also, samples were rectified so that the perpendicularity is less than 0.02 mm in 25mm (0.1%). The lateral surface is straight with a maximum difference of 0.02 mm throughout the entire specimen.

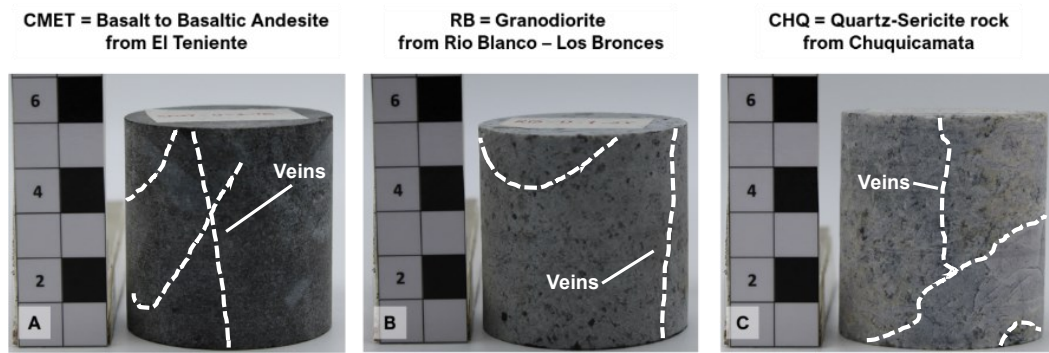


Figure 2 Photo of samples for uniaxial compressional tests. Samples contain veins of different length, width, orientations and infills. Slenderness ratio is $L:D \approx 1:1$.

Table 2. Slenderness ratio (D: L) and number of veins for tested samples.

Sample (ID)	L:D	Nº of veins	Sample (ID)	L:D	Nº of veins	Sample (ID)	L:D	Nº of veins
CMET-U-1-17	0.98	4	RB-U-1-4	0.98	3	QS-U-1-17-S	0.93	5
CMET-U-1-18	1.02	2	RB-U-1-11	0.99	3	QS-U-1-18-S	0.91	3
CMET-U-1-10	1.00	6	RB-U-1-14	0.97	8	QS-U-1-23-Q	0.93	4
CMET-U-1-24	0.99	4	RB-U-1-24	0.97	4	QS-U-1-26-Q	0.96	3
CMET-U-1-13	0.96	4	RB-U-1-28	0.97	7	QS-U-1-29-Q	0.93	1
CMET-U-1-28	1.02	9	RB-U-1-5	0.97	4	QS-U-1-6-S	0.93	5
CMET-U-1-16	1.00	8	RB-U-1-17	0.99	7	QS-U-1-4-S	0.93	6
CMET-U-1-12	0.99	7	RB-U-1-20	1.00	5	QS-U-1-3-S	0.94	4
CMET-U-1-5	1.00	6	RB-U-1-22	0.93	3	QS-U-1-10-S	0.91	6
CMET-U-1-2	0.98	8	RB-U-1-12	1.02	5	QS-U-1-9-S	0.93	4
CMET-U-1-4	0.95	5	RB-U-1-29	1.02	3			
CMET-U-1-9	0.98	5	RB-U-1-1	0.97	4			
			RB-U-1-16	0.94	6			

3.1.The Split Hopkinson pressure bar system (SHPB)

In this work, rock samples were tested using a SHPB system located at the Monash University, Australia^{69,70}. The SHPB consists of a striker bar ($\rho_b = 7850 \text{ kg/m}^3$, $E_b = 210 \text{ GPa}$, $C_b = 5200 \text{ m/s}$, $\sigma_p = 930 \text{ MPa}$, $\varphi=50\text{mm}$), incident and transmission bar ($\varphi=50\text{mm}$) in which the sample is sandwiched. A gas gun is used for impulse strike bar. There is a damper to absorb the impact of transmitted bar, and sample/bar interface is lubricated with water-based lubricant. A data acquisition device (NI PXIe 5105, sampling rate 1 MHz) collects the signal of two strain gauges (FLA-6-11) installed in both, incident, and transmission bars, respectively.

Tests start when the gas gun is loaded to the desired pressure. Once triggered, the striker bar moved towards the incident bar in which an incident wave (ε_{in}) was produced along during the impact. It is transmitted through the bar to the sample, and interaction resulted in a transmission wave (ε_{tr}) and a reflection wave (ε_{re}). Tests were performed at different impact velocities upon each set of samples, ranging from 5 to 18 m/s, as summarized in Table 3.

A high-speed camera Phantom V2511 (resolution of 256x256 pixels at 200,000 frames per second (fps)) was used to study the fracture pattern experienced during dynamic deformation. In that sense, three widely accepted main categories were used in this study for describing fracture patterns²²:

The first category corresponds to a Quasi-elastic or apparently intact behavior (Figure 3a). In this case, the rock sample has no visible new cracks. The second category corresponds to cracked or split by single fracture samples (Figure 3b). Here, the tested sample is recovered with new visible cracks along veinlets, or rock matrix, and usually some “white patches” can be recognized. White patches are related to the development of microcracking zones and are observed prior to the growth of visible fractures^{39,71}. Finally, the third category corresponds to samples showing fragmented or multiple fracturing level (Figure 3c). Here, the tested sample loses the loading carrying capacity because of sudden fragmentation or rupture along multiple veins and/or groundmass.

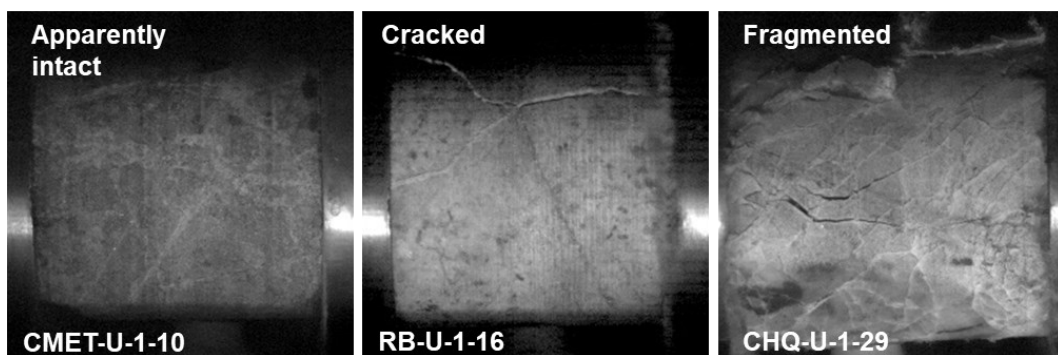


Figure 3 Fracture patterns (a) Quasi-elastic or apparently intact. (b) Cracked or split by single vein. (c) Fragmented or multiple fracturing.

The failure type description corresponds to indicate where the fracture is propagating through, and there are four primarily types^{8,72}: Homogenous, combined, discrete, and around or along veins. Homogenous failure means the sample fails through the groundmass or intact rock. Combined indicates the failure is through intact rock and healed veinlets or discontinuities. Discrete indicates the failure is along a discrete healed vein, and finally, the failure involves only the vein network. The vein acute angle with respect to the horizontal axis is described for combined, discrete, and along vein network failure types.

3.2. Data acquisition and processing

The data acquisition system used in this study correspond to a high-speed data acquisition (DAQ) system, National Instruments (NI) PXle-1078 with one slot of 8 channels, whereas sample rate is 1MHz. Captured incident (ε_i), transmitted (ε_t) and reflected (ε_r) waves data is processed for each test. According to one-dimensional stress-wave theory⁷³, following equations are used for calculations:

$$\sigma(t) = \frac{A_b E_b}{2A_s} [\varepsilon_i(t) + \varepsilon_t(t) + \varepsilon_r(t)] = \frac{A_b E_b}{2A_s} \varepsilon_t(t) \quad (1)$$

$$\varepsilon(t) = \frac{C_b}{L_s} \int_0^t [\varepsilon_i(t) - \varepsilon_t(t) - \varepsilon_r(t)] dt = \frac{C_b}{L_s} \int_0^t \varepsilon_r(t) dt \quad (2)$$

$$\dot{\varepsilon}(t) = \frac{C_b}{L_s} [\varepsilon_i(t) - \varepsilon_t(t) - \varepsilon_r(t)] = \frac{-2C_b}{L_s} \varepsilon_r(t) \quad (3)$$

Where $\sigma(t)$ is the axial compressional stress in the sample as a function of time t , A_b is the section surface of the bars, E_b is the Young's modulus of the bars (210 GPa), C_b is the wave velocity in the bars (5200 m/s). The parameters L_s and A_s are the length and area of the sample, respectively. The parameter ε corresponds to strain and the subscripts “ i ”, “ t ” and “ r ” are referred to the incident, transmitted and reflected waves, in that order. The parameter $\dot{\varepsilon}(t)$ corresponds to the strain rate during the test. A typical signal for the test is shown in Figure 4.

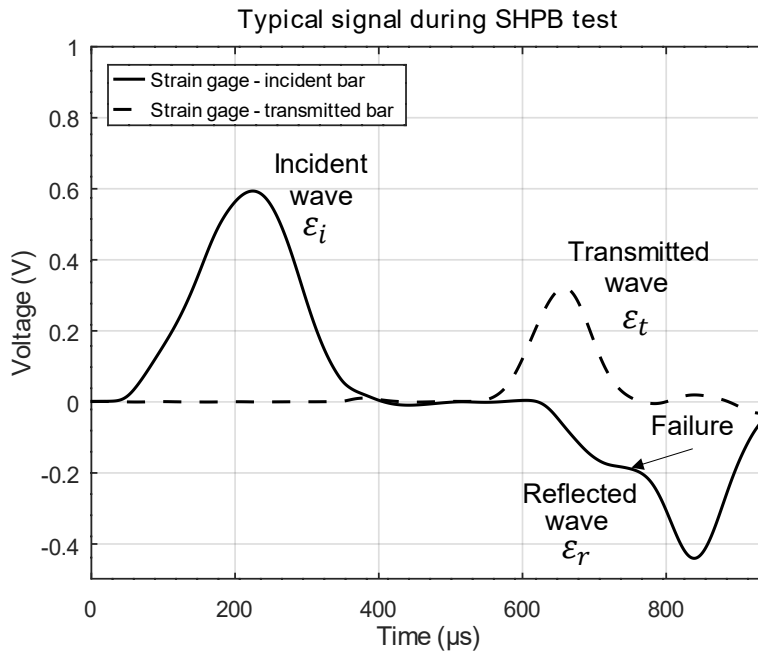


Figure 4. Typical incident ε_i , transmitted ε_t and reflected ε_r wave signal during uniaxial compressional test using a SHPB system at the impact velocity of 15 m/s. The moment of failure is recognized in the reflected wave as indicated.

The stress balance validates the results of each dynamic compressional test. It is achieved once the stresses measured at both ends of the sample are nearly equal^{22,55,68}. In Figure 5a the stress

balance is represented graphically in a typical test. Here, the equilibrium is reached once the stress of the incident plus the reflected is equivalent to that of the transmitted wave: $\sigma_i(t) + \sigma_r(t) = \sigma_t(t)$. Then, using equations (1), (2) and (3), the stress-strain curve can be plotted as shown in Figure 5b. The peak corresponds to the dynamic peak stress, or dynamic uniaxial compressive strength for fractured samples (σ_{ucd}).

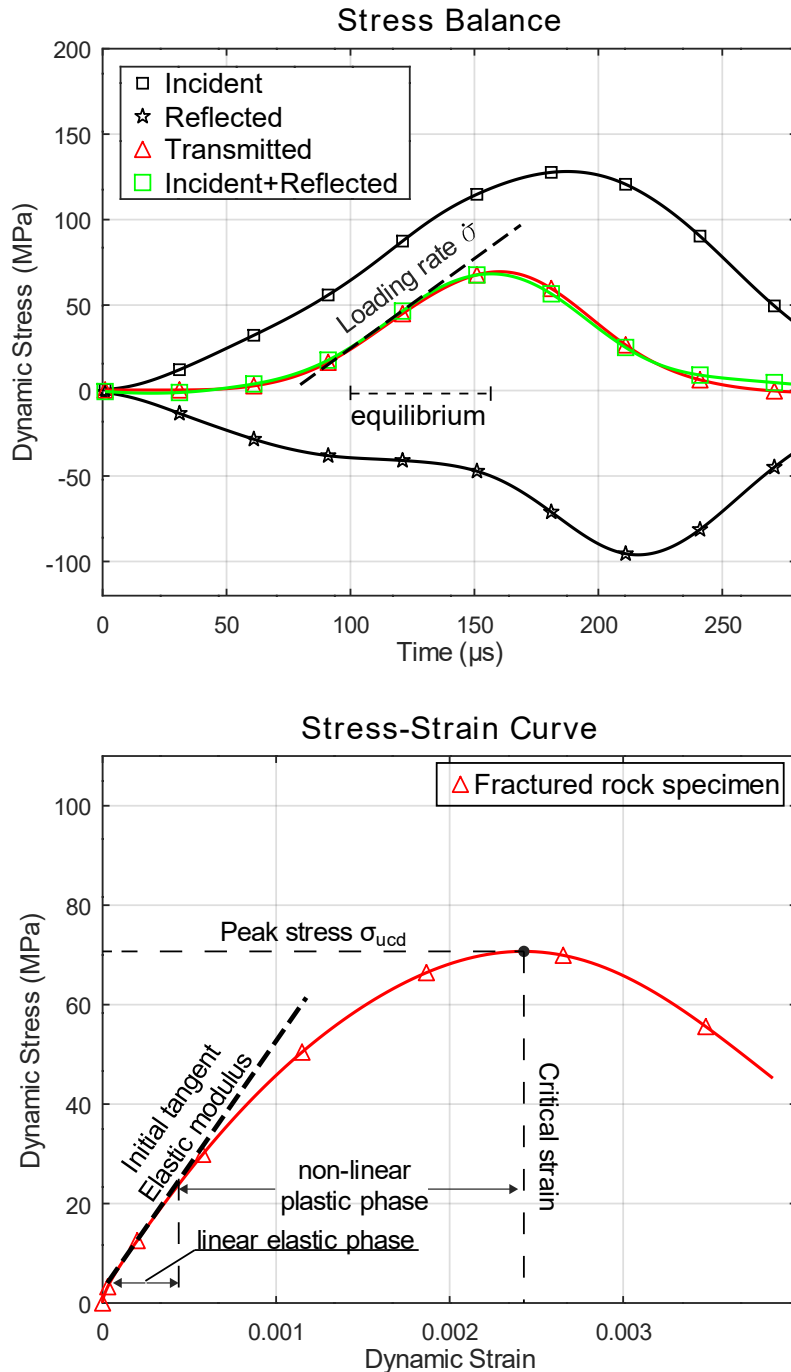


Figure 5. Top: Dynamic stress equilibrium $\sigma_i(t) + \sigma_r(t) = \sigma_t(t)$ for incident wave (i), transmitted wave (t) and reflected wave (r). **Bottom:** Stress-strain curve for determination of the peak stress (σ_{ucd}).

The stress pulse rise is lengthened by a red copper sheet placed between the striker and the incident bar in all tests. Here, the duration of the loading pulses is around 350 s. The time for the sample to reach stress equilibrium is denoted as T₀. Generally, T₀ is calculated around 3 to 5 reverberations of the stress pulse within the sample, which might not be necessarily equal to that measured empirically^{22,55}. The moment at the corresponding peak stress is denoted as T_f, which is related to the time of fracture.

Additionally, the Dynamic Increase Factor (DIF) is calculated as the ratio of the dynamic to static compressional strength^{27,30,69}, i.e., DIF = DCS/UCS. DIF values are plotted against strain rate values in an X-log chart. In this study, DIF is calculated for the peak stress of each tested sample using the following UCS values for each lithology: CMET = 94 MPa, RB = 150 MPa, and QS = 67–76 MPa (Table 1).

Table 3 Summary of results for uniaxial dynamic compressional tests using SHPB.

Sample ID	Impact velocity (m/s)	Dynamic uniaxial compressive strength σ_{ducs} (MPa)	Dynamic increase factor (DIF)	Critical strain ε	Peak strain rate $\dot{\varepsilon}$ (s^{-1})	Initial tangent modulus (E) (GPa)	Loading rate $\dot{\sigma}$ (GPa/s)	Dissipated Energy W_s (J)	Fracture Pattern	Failure type	Angle of involved veinlet
CMET-U-1-17	18	216	2,3	0,005	122	71	3591	22392	Fragmented	combined	32
CMET-U-1-18	18	174	1,9	0,003	155	185	4080	22194	Fragmented	combined	18
CMET-U-1-28	15	223	2,4	0,005	229	155	4414	11612	Fragmented	combined	39
CMET-U-1-4	12	149	1,6	0,002	127	145	2439	-	Cracked	discrete	33
CMET-U-1-10	16	247	-	-	73	44	3353	4688	Apparently intact.	-	-
CMET-U-1-24	16	230	-	-	167	195	4319	-	Apparently intact.	-	-
CMET-U-1-12	15	277	-	-	127	81	4819	10992	Apparently intact.	-	-
CMET-U-1-5	15	214	-	-	138	116	3639	143	Apparently intact.	-	-
CMET-U-1-16	15	162	-	-	77	285	2752	858	Apparently intact.	-	-

CMET-U-1-2	12	146	-	-	92	105	1814	-	Apparently intact.	-	-
CMET-U-1-13	12	132	-	-	133	78	2162	-	Apparently intact.	-	-
CMET-U-1-9	10	149	-	-	109	245	2771	972	Apparently intact.	-	-
<hr/>											
RB-U-1-24	18	247	1,6	0,004	49	72	3261	18583	Fragmented	combined	24
RB-U-1-11	18	239	1,6	0,004	54	62	3227	22994	Fragmented	combined	14
RB-U-1-28	18	207	1,4	0,007	148	80	3375	15511	Fragmented	homogenous	0
RB-U-1-14	18	128	0,9	0,004	203	92	2485	26201	Fragmented	combined	48
RB-U-1-20	16	186	1,2	0,004	88	115	3343	21974	Fragmented	combined	22
RB-U-1-17	16	158	1,1	0,003	131	115	3439	19937	Fragmented	combined	40
RB-U-1-3	15	185	1,2	0,005	96	-	2880	12863	Fragmented	homogenous	0
RB-U-1-29	15	111	0,7	0,005	114	42	1928	20727	Fragmented	combined	52
RB-U-1-16	12	103	0,7	0,005	74	38	1461	10076	Fragmented	combined	25

RB-U-1-5	16	217	1,4	0,007	117	135	3910	683	Cracked	discrete	0
RB-U-1-22	16	212	1,4	0,007	97	47	3249	12504	Cracked	combined	0
RB-U-1-12	15	167	1,1	0,005	65	42	2346	10766	Cracked	discrete	24
RB-U-1-1	12	150	1	0,005	133	92	2411	-	Cracked	discrete	0
RB-U-1-4	18	266	-	-	96	92	4195	-	Apparently intact.		
QS-U-1-26-QMS	16	116	1,5	0,003	188	79	2434	19495	Fragmented	combined	37
QS-U-1-9-QIS	16	172	2,6	0,007	131	47	1568	14140	Fragmented	combined	36
QS-U-1-29-QMS	15	117	1,5	0,004	174	38	1017	14083	Fragmented	homogenous	0
QS-U-1-17-QIS	12	102	1,5	0,006	102	38	1235	7615	Fragmented	homogenous	0
QS-U-1-10-QIS	15	163	2,4	0,007	89	47	1327	4095	Cracked	combined	42
QS-U-1-18-QIS	5	93	1,4	0,006	72	20	839	1626	Cracked	combined	46
QS-U-1-23-QMS	5	111	1,5	0,005	43	26	646	2628	Cracked	combined	33
QS-U-1-3-QIS	5	97	1,4	0,003	84	34	748	348	Cracked	homogenous	-

CHQ-U-1- 6-QIS	5	70	1	0.007	59	21	515	3599	Cracked	combined	18
CHQ-U-1- 4-QIS	5	97	-	-	77	25	694	44	Apparently intact.	-	-

3. RESULTS

The summary of results is presented in the Table 3. In addition, the dynamic uniaxial compressive strength (σ_{ducs}) and the dynamic increase factor (DIF) of the fractured samples are plotted to compare results of the three rock types (Figure 6). The σ_{ducs} of both the RB and CMET samples are higher than σ_{ducs} of QS samples. The higher σ_{ducs} value of fractured RB samples is 247 MPa, whereas the higher σ_{ducs} value for fractured CMET samples is 216 MPa. In the case of QS samples, the higher value of σ_{ducs} corresponds to 172 MPa. The fragmented DIF values of QS and CMET samples are major than 1.5 and are typically higher than those calculated for fragmented RB samples.

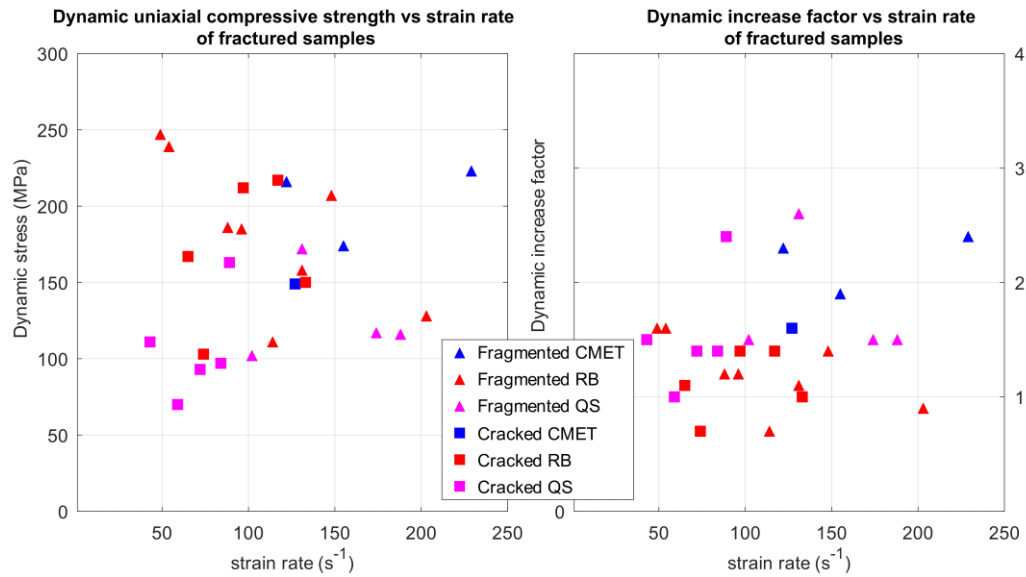


Figure 6: Result comparison of CMET, RB and QS fractured samples.

3.1. Results for CMET

The summary of results for CMET is shown in Table 3. Further, stress-strain curves for fractured samples are shown in Figure 7 where different colors are used for plotting different fracture patterns and failure types. The impact velocity is indicated in the legend (10, 12, 15, 16, and 18 m/s).

In general, three phases of deformation can be recognized in the stress-strain curves: 1) a first stage where the curve adopts a straight trend following a linear-elastic deformation in which Young's Modulus can be identified; 2) approximately after 0.1% of dynamic strain, the curve indicates a non-linear plastic deformation; and 3) a failure stage after the dynamic uniaxial compressive strength is reached.

Most of the strain energy is constrained in the non-linear plastic phase, which is two to six times the strain in the linear-elastic phase. Furthermore, in some samples, the linear elastic phase is difficult to recognize, such as CMET-U-1-2. Peak stress ranges from 132 to 277 MPa. The critical strain is between 0.2 and 0.6%.

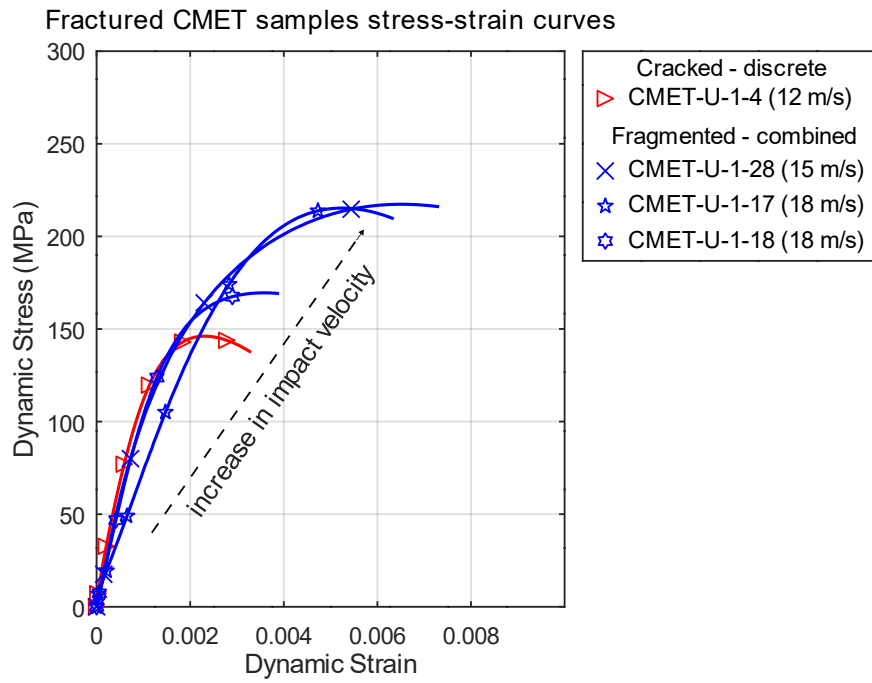


Figure 7 Stress-strain curves for CMET samples. Tests are grouped according to fracture pattern and failure type.

The Dynamic Increase Factor (DIF) values for fractured samples range from 1.2 to 1.8, while peak strain rates exhibit values from 73 to 229 s⁻¹. The initial tangent elastic modulus values range from 81 to 245 GPa. Variations in the elastic modulus of these samples are reported to be common during uniaxial compressive tests under quasi-static loadings (17). In terms of fracture pattern, this group resulted in 3 fragmented, 3 cracked, and 6 apparently intact. Fractures showed veinlet-controlled propagation in fragmented and cracked samples at impact velocities higher than 12 m/s. Moreover, apparently intact samples are mostly related to tests with impact velocities below or equal to 12 m/s.

3.2. Results for RB

The summary of results for RB samples is shown in Table 3. The stress-strain curves for each tested sample are shown in Figure 8, in which colored symbols indicate the failure pattern and type, whereas the legend indicates the impact velocities of 12, 15, 16, and 18 m/s. Peak stress range from 103 to 266 MPa. Samples with impact velocities of 12 to 10 m/s reached peak stress values of 150

MPa, while samples with impact velocities of and above 15 m/s reached values of up to 266 MPa.

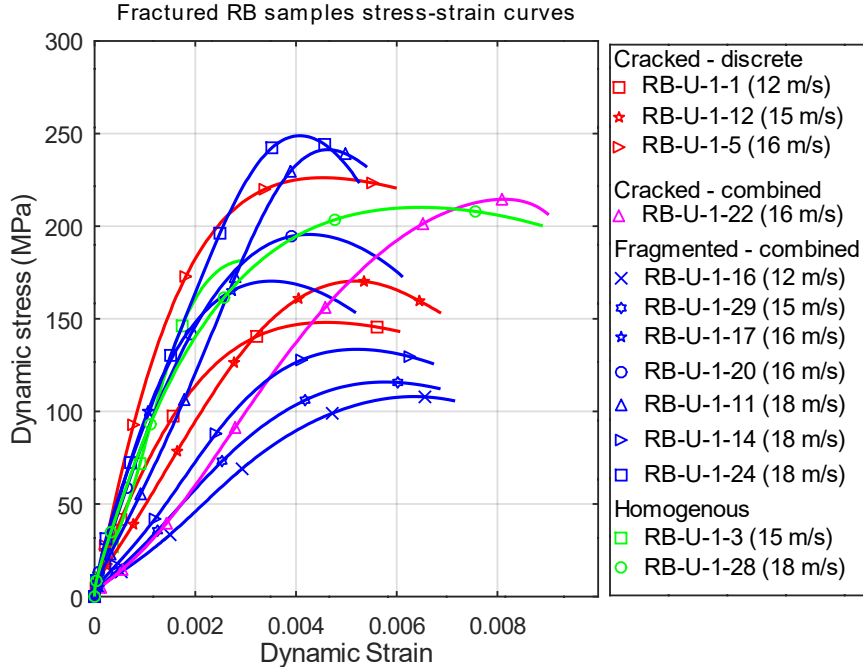


Figure 8 Stress-strain curves for RB samples. Tests are grouped according to fracture pattern and failure type.

The strain at peak stress is between 0.3 and 0.7%. The dynamic increase factor of fractured samples exhibits values from 0.7 to 1.6, and peak strain rates show values from 49 to 203 s^{-1} . The initial tangent elastic modulus values range from 45 to 135 GPa. The fracture pattern of the samples indicates there are 8 fragmented, 5 cracked, and 1 sample apparently intact. All samples that resulted in a fracture pattern from fragmented to cracked showed a clear vein-controlled fracture propagation. Cracked are mostly related to tests with impact velocities below or equal to 15 m/s and peak stress below 170 MPa, whereas samples with higher impact velocities show a fragmented failure pattern and higher peak stress. Nonetheless, the sample with a higher peak stress is the one that resulted in an apparently intact sample.

3.3. Results for QS

The summary of the results for QS samples is shown in Table 3. Stress-strain curves are shown in Figure 9, in which colored symbology indicates failure pattern and type. Impact velocities are indicated in the legend at 5, 12, 15, and 16 m/s. Similar to CMET and RB samples, the phases of deformation identified in QS samples are three: linear elastic, non-linear plastic, and failure stage. Peak stress ranges from 67 to 172 MPa for QS samples; strain at peak stress ranges from 0.2 to 0.7%. The dynamic elastic modulus for these samples ranges from 25 to 79 GPa.

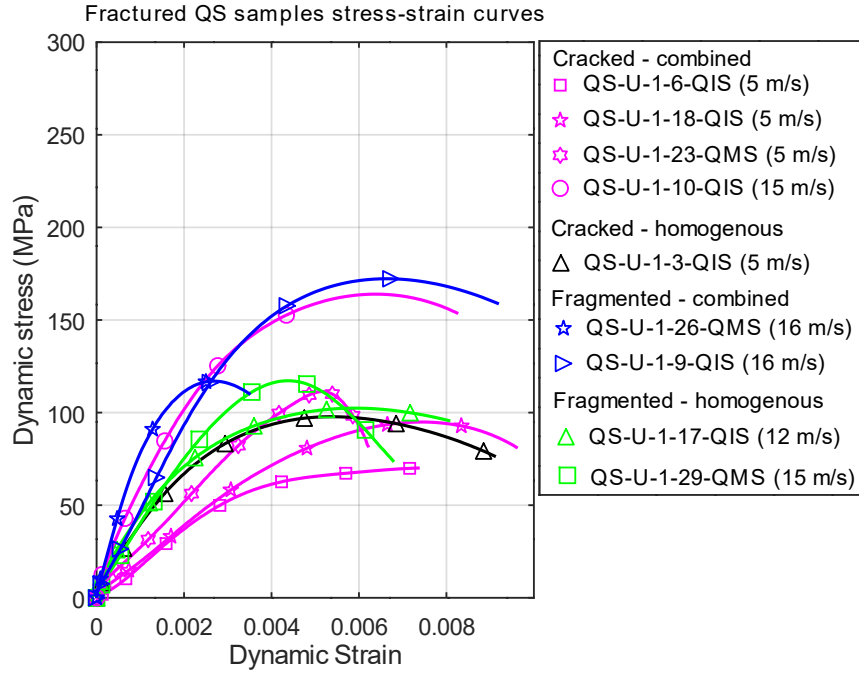


Figure 9 Stress-strain curves for QS samples. Tests are grouped according to fracture pattern and failure type.

In terms of failure patterns, this group resulted in 9 out of 10 fractured samples. In both fragmented and cracked patterns, failure types are mostly combined, but some homogenous types are observed as well. Prior to failure, white patches related to both groundmass and veinlets can be observed widely throughout the surface when the sample is fragmented. Cracked samples are mostly related to tests with impact velocities below 12 m/s, and peak stresses are not higher than 100 MPa, whereas samples with higher impact velocities show failure patterns with multiple fractures and higher peak stresses

4. DISCUSSION

4.1. Dynamic properties: Strain rate effect

The discussion about the effect of higher strain and loading rate by comparing to quasi-static tests has no consensus about whether the elastic modulus or critical strain change. In general, it is accepted that the σ_{ducs} should increase with higher strain rates²⁴. Moreover, the transition from single fracturing to intense pulverization depends on the strain rate²⁵. In that sense, tested rocks exhibited in this study changes in their mechanical properties due to the effect of strain rate increases from 10^{-5} to 10^2 s^{-1} . While CMET elastic modulus of fractured ranges from 68 to 113 GPa, i.e., 1.6 to 2.4 times higher elastic modulus in comparison to a quasi-static test (35.2 GPa adopted in this study). Similar results show RB samples, where 75% of samples exhibit elastic modulus from 1.17 to 2.55 times higher than the quasi-static value (53 GPa). Finally, the elastic modulus of QS samples ranged from 25 to 79 GPa, and the samples showed an increase of 0.9 to 3.95 times with respect to the quasi-static elastic modulus (20 and 27 GPa for QIS and QMS, respectively). Hence, the calculated stiffness values of the three lithological groups are higher with

respect to quasi-static stiffness. In addition, if we consider the difference between quasi-static and dynamic stiffness values (Δ_{ϵ}), the QS samples show consistently greater difference in stiffness than the observed in CMET and RB samples i.e., $(\Delta_{\epsilon}\text{QS}) > (\Delta_{\epsilon}\text{CMET})$ and $(\Delta_{\epsilon}\text{QS}) > (\Delta_{\epsilon}\text{RB})$.

The dynamic uniaxial strength σ_{ducs} exhibited by most of the tested samples tends to be higher than the quasi-static UCS values reported (Table 2), which is indicated by the DIF values for each sample (Table 3). Given the range of strain rates, the increase in strength can be up to 2,6 in QS, 2,4 in CMET, and 1,8 times in RB.

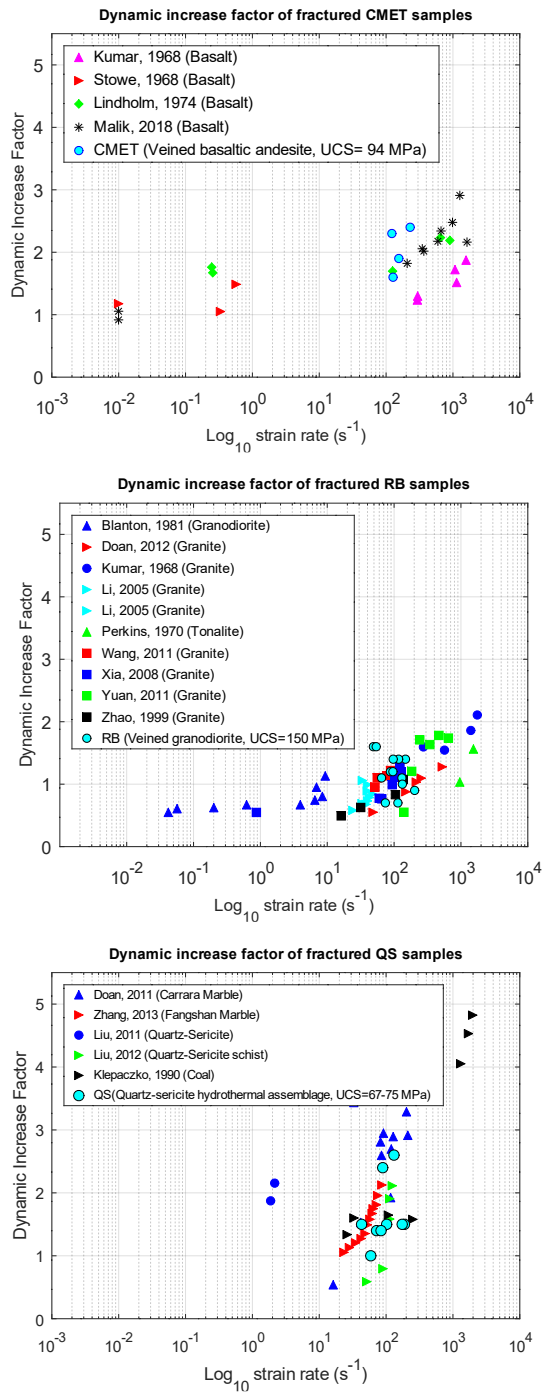


Figure 10. DIF for compressional dynamic test. Top: CMET, Mid: RB and Bottom: QS. Additional data with similar lithology or DIF results are incorporated for comparison.

It is generally accepted that there is a critical strain rate value at which the increase in σ_{ducs} becomes significant whereas fracture patterns change from single to multiple fracturing and pulverization^{22,25,27}. In addition, many efforts have been made by proposing semi-empirical rate-dependent strength equations for rock-like materials^{27,30,69}. To observe the effect of veins at high strain rates, DIF results for dynamic uniaxial compressional tests are compared against other studies for similar lithologies. CMET results for DIF values are close to others obtained for basalts (see Figure 10a). Likewise, RB samples (Figure 10b) show similar DIF values to other studies in granites, granodiorites and tonalites. There is special attention to DIF results in QS. The increase in strength indicates a strong strain rate dependence. It suggests that its critical strain rate is lower than those exhibited by CMET and RB samples and is close to marble.

Finally, two notes of caution should be considered. First, it seems possible that the previous comparisons may be affected by the mismatch in specimen dimensions, however there is no clear evidence of this effect. A detailed analysis of the mismatch is out of the scope of this paper, and more tests should be performed in the future. On the other hand, it is well known that experimental testing on rocks with heterogeneities such as veinlet networks is challenging. Indeed, results usually show some variability and therefore, data must be interpreted with caution. Despite some experimental limitations, this study provides new insights into the dynamic properties of veined rocks.

4.2. Impact velocity effect and fracture process

The trend that stress-strain curves exhibit for an increase of the impact velocity is analyzed for each rock type and strain rate range. In general, by the increase of the impact velocity then higher is the loading rate, and higher is the peak stress.

Experimental results indicate that 70% of the samples resulted in fragmented or cracked samples, both mostly related to veinlets. The fracture process and resulting fragment formation in RB and CMET are controlled by veinlets. Groundmass does not show visible cracks until fracture propagation through veinlets. Given an increase in the impact velocity and loading rate, before the split white patches^{39,71} are observed at the veinlet infills, veinlet edges, and, in some cases, at the groundmass, about 70 s after the stress pulse arrives in the sample. The number of white patches is qualitatively greater as the loading rate increases, as indicated in figures 11 and 12.

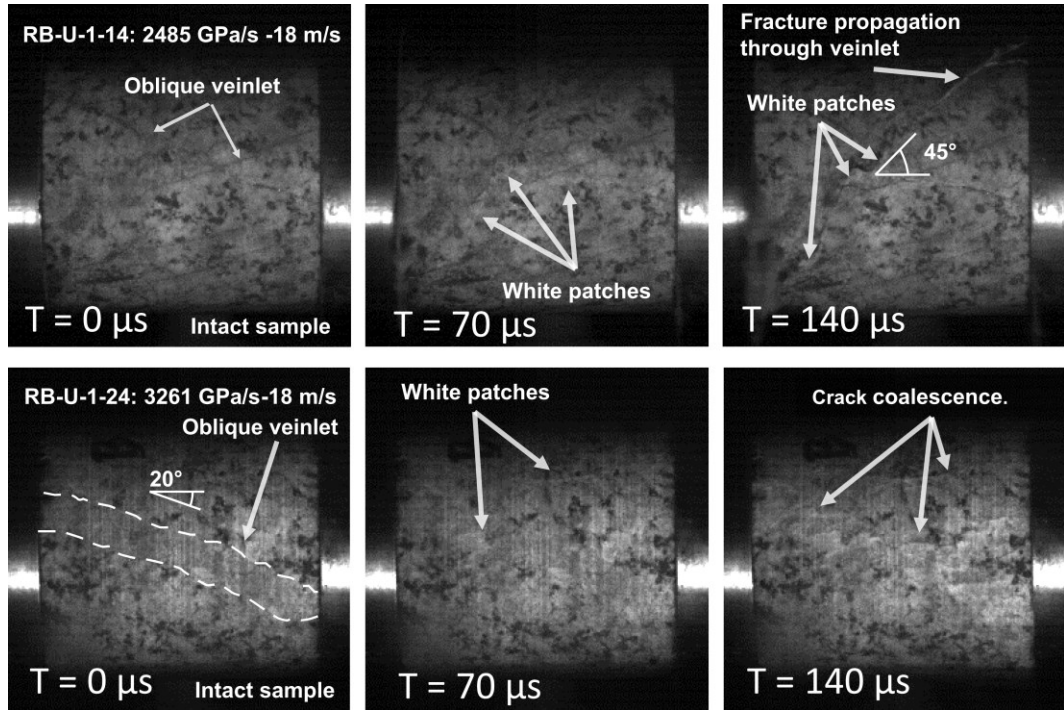


Figure 11 Increase in loading rate in RB samples. It is shown that the veinlet controls the fracture process as a stress reliever, while microcracks close to the veinlet coalesce into microcracks in the groundmass, indicated by the white patches. The higher the loading rate is, the higher the volume of cracks that coalesce around the veinlet.

In the case of QS samples, the fracture pattern is controlled by loading rate and impact velocity, such as CMET and RB, but the fracture pattern does not show a clear vein-controlled mechanism. Instead, coalescence of microcracks occurs widely within the sample when impact velocities are higher than 15 m/s, as shown in Figure 12. For lower impact velocities and loading rates, the fracture propagation is controlled by splits through veins and white patches in groundmass and veins.

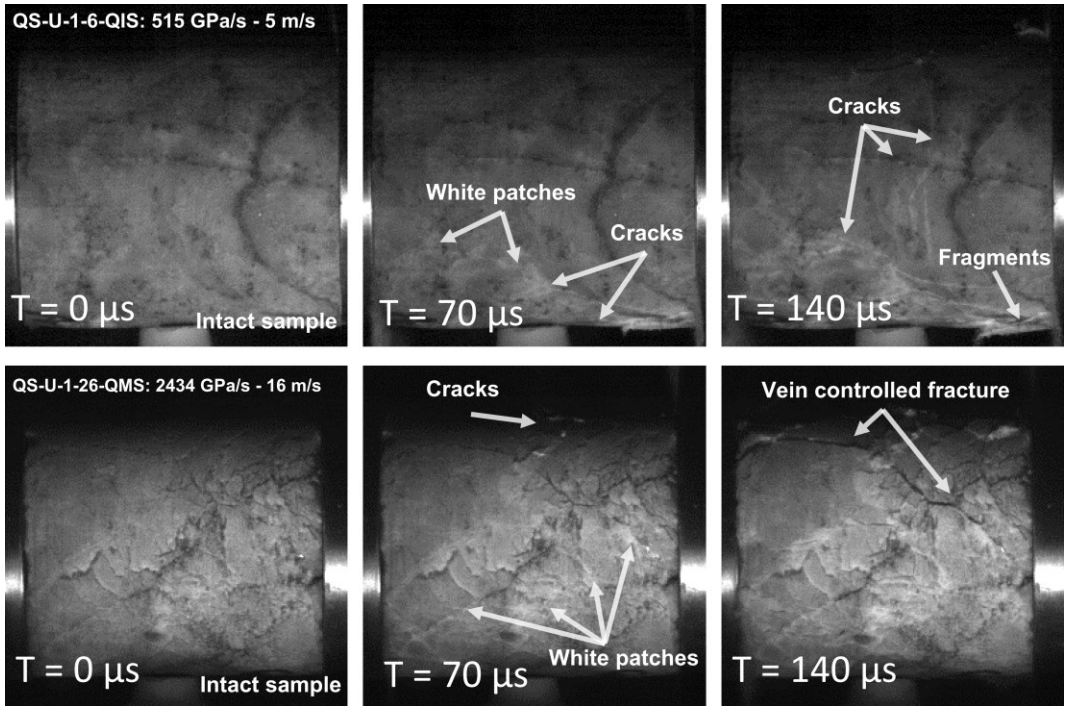


Figure 12 Increase in loading rate due to impact velocity. It is shown that white patches occur prior cracks. White patches can be related to veins or groundmass. Moreover, the number of white patches in surface is qualitatively greater under high loading rates.

The implications of the fracture process under high loading rates (10 to 10^4 MPa/s) have been discussed for rocks such as granite, marble, and sandstone^{16,19,39,73}. Different physical mechanisms are postulated to explain the fracture process and enhancement of mechanical properties of homogenous rocks. Some predominant theories concerning the rate sensitiveness are listed as follows. The fracture process, such as described by Grady and collaborators⁷⁵⁻⁷⁷, indicates that under higher loading rates, a single microcrack is not enough to relieve the increasing stress, then cracks grow and coalesce parallel to the loading axis, resulting in the axial splitting failure. This mechanism explains the additional flaws and a major number of failure surfaces under high loading rates, which resulted in a higher dynamic strength of granite samples²¹. On the other hand, the mechanism explained by Cho and collaborators⁷⁴ indicates that sample inhomogeneities contribute to the strain rate dependency, stress concentrations, and redistributions at high loading rates. Then, the strength increase in the rock under high strain rate is caused by crack arrest due to the generation of microcracks.

To understand the rate sensitiveness and the physical mechanism of the fracture process in tested samples, several aspects related to the results are summarized as follows. In QS samples, white patches are observed in both veinlets and groundmass. Furthermore, the impact velocity increase led from a veinlet-controlled fracture (i.e., cracked) to multiple fractures observed in both the groundmass and veinlets (i.e., fragmented). In CMET and RB samples, white patches are distinguished only by the mineral infills and rims of veins.

For impact velocities in this study, failure types in CMET and RB samples are described as combined or discrete (i.e., veinlet-controlled), whereas QS samples are either combined or homogenous. The veinlet angle with respect to the loading direction (horizontal = 0) is roughly 15

to 50° , and peak stress is related to angles close to 25° . The orientation of the veinlet-controlled fractures for RB fragmented-combined failure are summarized in Figure 13 Left. This result indicates that the involved veinlet angle controls the σ_{ducs} in RB samples. Moreover, as a result of the increase in both the loading rate and impact velocity, the fracture pattern changes from cracked to fragmented. (See Figure 13 right).

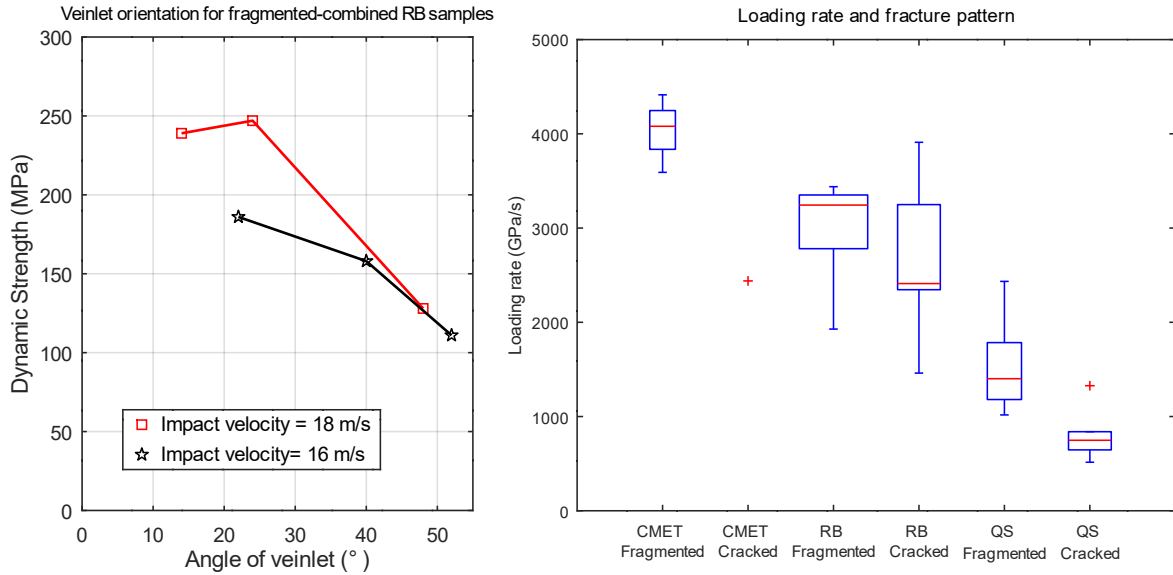


Figure 13: Left: Veinlet-controlled fracture orientation for fragmented-combined failure in RB samples with similar impact velocity, indicating that the σ_{ducs} is controlled primary by the orientation of the involved veinlet. **Right:** Box plot for fracture pattern and loading rate trend for fractured samples in this study indicating that fragmented failure patterns are most likely related to higher loading rates.

In fractured samples, cracks were initially propagated by veinlets in both low and high impact velocities. Nevertheless, in the case of QS samples, this relation is not necessarily true. Instead of that, the fracture propagates to zones where white patches are seen by the naked eye prior failure, i.e., where strain inhomogeneous deformation can be seen, similar to the observations of the compressive strain localizations in heterogenous concrete aggregate materials⁷⁸. The localization of strain could be related to the mechanism postulated by Cho et al. (2003), and explains the presence of white patches and the fracture propagation initially from a veinlet and then to the groundmass, i.e., crack arrest due to the presence of microcracks. Also, the mechanism for the enhancement of the mechanical properties proposed by Grady and collaborators⁷⁵ explains the presence of white patches (i.e., microcracks) in both the groundmass and veins in QS samples.

4.3. Dynamic properties: Implications to strainburst in deep mining

The occurrence of rockbursts is one of the main challenges for underground mining. Among rockbursts types, strainbursts are the most frequent⁷⁹. Following common guidelines for rockburst assessment⁵⁰, two aspects for strainbursts occurrence i.e., potential and severity, must be addressed. In terms of strainburst potential, the main conditions refer to the failure manner of the rock mass, which requires that i) the rock mass must fail in a brittle manner, thus displaying a high intrinsic brittleness, and ii) a high level of tangential stress at the boundary of the excavation. In terms of

severity, the main conditions refer to the actual volume of rock ejected during the burst and the energy budget related to the failure process and rock deformation.

As shown before, our results show a change in the mechanical properties of veined rock samples due to the application of different dynamic loads. As a result of the impact velocity increase, a higher loading rate and dissipated energy are registered (See Table 3, Dissipated Energy Column), which is related to the changes in the fracture pattern from cracked to fragmented. Moreover, we observe that the fracture pattern is controlled by both veins and the impact velocity, failing in a brittle manner. In our study, the energy dissipation for fragmented samples is around 15 to 20 kJ.

Based on our observations, the increase in mechanical properties in terms of stiffness and strength due to dynamic loadings may produce an underestimation of the actual severity and damage when strainburst potential is assessed with respect to the quasi-static rock properties. Also, since the generation of blocks can alter the severity level of strainbursts by increasing the tonnage of displaced rock, it is important to consider the effect of veinlets on the fracture process and the energy being dissipated, in addition to their strain rate dependency. Of course, the installed support system will likely play a role in the extension of the damage observed in the excavation. While this point is not discussed in this work, it is important to mention that support systems modify the response and extension of the damage induced by rockbursts in the excavation.

5. CONCLUSIONS

The dynamic behavior of veined rocks from three major underground mines in Chile was studied by using a Split Hopkinson Pressure Bar. The fracture pattern during the test was recorded by a high-speed camera device. By variating the impact velocity of the striker bar, mechanical properties such as dynamic compressional strength, elastic modulus, failure strain, and fracture pattern were discussed. The instant increase in mechanical properties, in comparison to quasi-static tests, is observed in most of the tested samples.

The ranges for peak stress in CMET and RB are similar to those observed in isotropic samples of similar groundmass lithology, as indicated by the DIF X-log charts, where strain rates range from 10 to 10^2 s^{-1} . Furthermore, our tests show that failure is strongly controlled by the veins. For lower impact velocities, the failure pattern is mostly cracked through veinlet-controlled fractures. As the impact velocity increased, the fracture pattern evolved from cracked to fragmented, while the veinlets conducted fracture propagation. Moreover, the dynamic uniaxial compressive strength of fragmented-combined RB samples appears to be primarily controlled by the angle of the involved veinlet. The generation of white patches during testing appears to be qualitatively higher at higher loading rates. None of the samples were pulverized.

The enhancement of the mechanical properties of the veined rocks can be explained both by the coalescence of microcracks in the groundmass and by the inhomogeneity of the samples. The veinlets act as stress relievers and increase stress concentrations and redistribution mechanisms in the groundmass. The mechanism proposed by Cho et al. (2003) best explains the enhancement of mechanical properties of samples under loading rates with weak rate sensitiveness (CMET and RB samples), while the mechanism postulated by Grady et al. (Grady & Kipp, 1987; Grady & Lipkin, 1980) is suitable for samples with strong rate sensitiveness (QS samples). We propose that the increase in stiffness and dynamic uniaxial compressive strength, the propensity for block formation through veinlet-controlled fractures, and the dissipation energy due to dynamic failure, are

important phenomena to consider during the evaluation of the potential and severity of strainburst on veined rock masses in deep underground mines.

Acknowledgments

FR and LFO gratefully acknowledge the financial support from the basal project FB-0809 of the Advanced Mining Technology Center (AMTC). The authors sincerely appreciate the permission given by CODELCO to publish this paper. Also, we thank Huachuan Wang who continuously supported the tests, data acquisition and processing, and David Veloz who helped with sample preparation. We also deeply acknowledge to Sofia Rebollodo for their contributions and priceless comments. We thank the Editor and the anonymous reviewers for their time and constructive comments. This research has been supported by the National Agency for Research and Development of Chile (ANID) with grant FONDECYT 11190985. Data supporting the analysis and conclusions are available upon request to the corresponding author.

3 Artículo 2: Dynamic mechanical properties under confinement of veined rocks from El Teniente Mine in Chile.

Franco Robbiano^{1,2,3}, Kai Liu^{4,5}, Qian-Bing Zhang⁴, Luis Felipe Orellana^{1,3,*}

¹ Department of Mining Engineering, FCFM - University of Chile, Chile

² Department of Geology, FCFM - University of Chile, Chile

³ Advanced Mining Technology Center (AMTC), FCFM - University of Chile, Chile

⁴ Department of Civil Engineering – Monash University, Melbourne, Australia

⁵ Department of Engineering Science, University of Oxford, Parks Road, OX1 3PJ, United Kingdom

ABSTRACT

Rockbursts correspond to complex events characterized by the spontaneous release of energy at the limits of deep underground rock excavations, and several events in deep underground mines involved both worker and equipment safety being impaired. Therefore, the understanding of this phenomenon is challenging. In this study, we report a series of uniaxial and biaxial tests carried out with a Hopkinson triaxial bar (THB), and a high-speed camera up to 200,000fps, to understand the role of dynamic loads and high strain rates (10 to 10^2 s⁻¹) in mechanical behavior and fracture patterns of veined rocks. The samples correspond to cubes made from rocks of the main underground mining district in Chile, El Teniente (CMET). Two stress states are represented: uniaxial confinement, and biaxial confinement. The results obtained are not conclusive with respect to the increase in the strength to uniaxial load, when compared with respect to the unconfined state with load rates from creep to quasi-static. However, a clear increase in elastic modulus is observed with increasing σ_2 . In addition, two types of post-peak curves are obtained, i.e., Type I and II: The type I is associated to tested sample that does not lose its load capacity in a state of biaxial confinement even after a singular fracture is observed on the free face. The type II curve is associated with the fragmentation of the sample and fragments expulsion from the free faces. Veinlet-controlled fractures are observed in samples with veinlets that are oriented parallel to sub-parallel to the direction of the dynamic load. The phenomenon of dynamically loaded strainburst is satisfactorily reproduced. Indeed, two dynamic phenomena related to this type of event are observed: slab buckling, and fragments expulsion at high speeds after sample fracturing during the test. We suggest that the fractures propagate through the matrix when the mechanical properties show a strong rate-sensitiveness, while they are restricted to the veinlets when this dependence is less evident. Faced with a dynamic pulse that generates deformation rates between 10 to 10^2 s⁻¹, stiffness increases, and therefore energy dissipation as well. The proneness to block formation is higher in veined rocks. Then, the higher temporal stiffness and proneness to block formation are characteristics that could increase the severity of strainburst in the deep underground excavations of the studied mining district.

1. Introduction

One of the principal issues in the last few decades in open-pit mining is the increase in operational costs due to the deeper extension of the ore body. The migration to the underground mining seems to be the a recurrent solution: For example, mining operations in copper-molybdenum porphyries, such as Chuquicamata Mine in Calama, Andina mine in Los Andes, and El Teniente mine in Rancagua, in Chile, are currently mining deeper below ground surface by development of underground mining techniques.

Since new stress conditions(Brown & Hoek, 1978) due to the perturbation after the excavation in deep underground environments, new geotechnical challenges are identified and requires understanding of tectonics, local concentration of stress due to geological faults (Ahorner, 1975; Chester & Chester, 2000; Engelder & Sbar, 1984; Ferrarini et al., 2015), redistribution of in-situ stresses during excavations (Barton & Shen, 2017; M. Cai, 2008; X. Li et al., 2017) and the role of discontinuities, such as joints and veins, in the behavior and mechanical properties of rock. Rocks from porphyry bodies are characterized by the presence of hydrothermal veins, veinlets, and stockworks, which are widely observed in copper molybdenum ore bodies in Chile (Astudillo et al., 2008; Deckart et al., 2005; Skewes et al., 2005). They are the main feature for which these rocks are considered anisotropic.

The dynamic behavior of rocks from porphyry ore bodies is not fully understood yet. Most of the studies about the mechanical properties of anisotropic rocks are carried by testing under creep to quasi-static conditions. Moreover, recent studies of the mechanical properties of bedded or/and anisotropic specimens under high strain rates (W. Wang et al., 2020; Xia et al., 2008; Yang et al., 2020), shows that the mechanical properties, such as young's modulus, peak strength, and critical strain depends on the angle of bedding with respect to the loading axis.

The studies above mentioned have been carried by using the Split Hopkinson Pressure Bar (SHPB) apparatus or Kolsky bar (H. Kolsky, 1949; Q. B. Zhang & Zhao, 2013a). The SHPB is used widely to understand the dynamic mechanical properties of materials under high strain rates (10-10⁴). Some of the tested rocks using this apparatus are enlisted as follows: basalts(Kumar, 1968; Lindholm et al., 1974; Malik et al., 2018), acid igneous rocks(Blanton, 1981; Doan & d'Hour, 2012; Kumar, 1968; X. B. Li et al., 2005; Perkins et al., 1970; Y. Wang & Tonon, 2011; Xia et al., 2008; Zhao, Zhou, et al., 1999) and hydrothermal or metamorphic rocks(Doan & Billi, 2011; S. Liu et al., 2011), among other rock-like materials. These studies indicate that both, mechanical and fracture behavior under dynamic conditions, are different when comparing to quasi-static behavior due to the high loading and strain rates(Bischoff & Perry, 1991; Doan & Gary, 2009; K. Liu et al., 2019b; Q. B. Zhang & Zhao, 2013b; Zhao, Zhou, et al., 1999).

Dynamical testing of rocks provides priceless information about the mechanical properties of rocks under dynamic loads. Moreover, the implementation of new dynamic testing techniques, such as the Triaxial Hopkinson Bar(K. Liu et al., 2019b) opened a new approach for the rockburst phenomena understanding (K. Liu et al., 2020; Su et al., 2019).

Rockburst is a deep underground rock phenomenon that occurs as a violent and sudden event of damage near an excavation face and is associated with a seismic event (M. Cai, 2019; Ming Cai & Kaiser, 2018; Peter K. Kaiser & Cai, 2012; Simser, 2019; Y. X. Zhou et al., 2012). Even though rockburst classification still in debate(J. Zhou et al., 2018b), the classification shown in Figure 1 is adopted in this study (Figure 1).

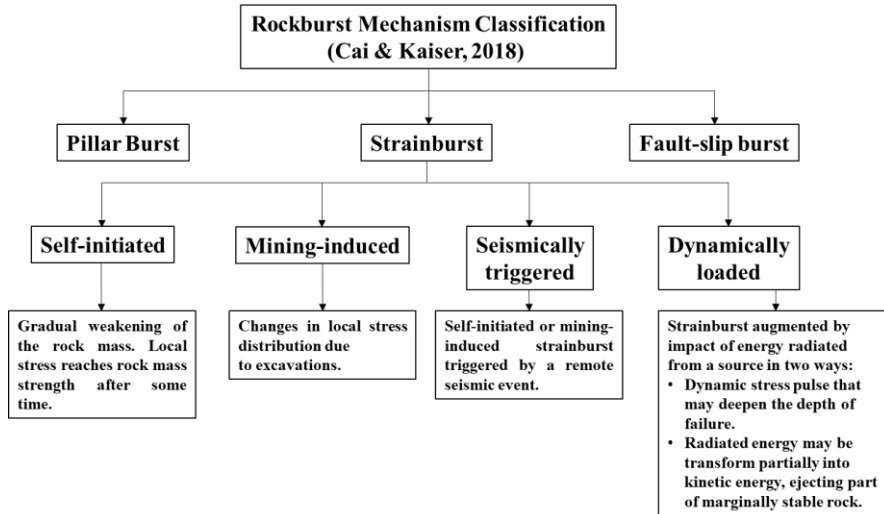


Figure 1 Rockburst and strainburst mechanism classification according to Cai & Kaiser (2018).

Dynamically loaded strainburst can be caused by a dynamic disturbance, predominantly by stress pulses from blasting or energy transfer from a remote seismic, such as schematically shown in Figure 2. In Chile, more than 100 of these events are recorded since 1992 in the El Teniente mine(Ming Cai & Kaiser, 2018), and other mines and projects in the world(J. Zhou et al., 2018b). Understanding this phenomenon in underground mines represents a great priority to minimize risk to mining operations: Injuries to workers or fatalities, damage to mine infrastructure and equipment, time-consuming rehabilitation, and production losses(Ming Cai & Kaiser, 2018; Peter K. Kaiser & Cai, 2012).

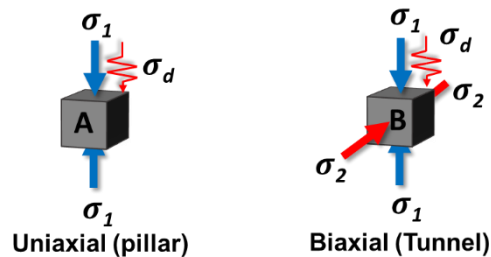
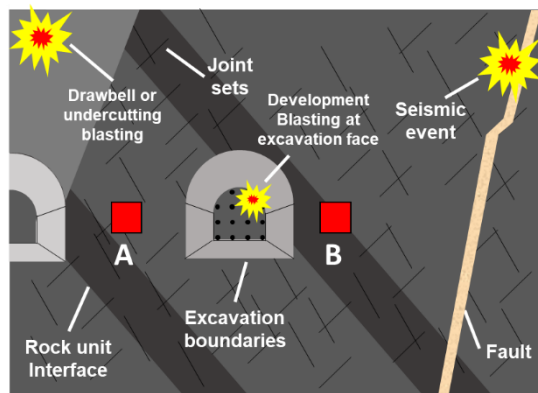


Figure 2 Schematic representation for underground excavation and coupled static-dynamic loading conditions given a dynamic load source.

Given the dynamic nature of this process, such events may be easily reproduced by dynamic tests in the lab(K. Liu et al., 2020) by using a Triaxial Hopkinson bar, giving an approach to rockburst prevention or mitigation, but also to rockburst assessment. In this research a Triaxial Hopkinson Bar apparatus is used for testing rocks from the major underground mine in Chile operated by CODELCO: El Teniente. By this, the objective is to aim for a better understanding of dynamic compressional properties of veined rocks subjected to dynamic loads and high strain rates (10 to 10^2 s^{-1}) in different biaxial and uniaxial confinement states, aiming for a dynamic approach for strainburst assessment.

2. Experimental procedures

To study the dynamic mechanical properties of veined rocks under biaxial confinement in a Triaxial hopkinson, rock samples were obtained from El Teniente Mine, in Central Chile, with estimated resources of $>96 \times 10^6$ metric tonnes of fine Cu in ore in central Chile (CODELCO, 2019; Skewes et al., 2005). Most of mineral resources in El Teniente mine are hosted by El Teniente Mafic Complex (CMET) geological unit, which consist in a pervasively biotite-altered and mineralized mafic intrusive complex composed of gabbros, diabases, and porphyritic basalts and basaltic andesites (Skewes et al., 2005). This unit is also affected by a dense stockwork composed of biotite-dominated veins whose thickness range from 0,5 mm to several centimeters, with biotite rich halos of variable width. Density of veins is often so high that overlaps each other. Subsequent Late Magmatic Alteration generated quartz veins that cut earlier biotite-veins, as shown in (Skewes et al., 2005). The physical and mechanical properties of intact rock are summarized in table 1:

Table 1: Physical and mechanical properties of rock samples used in this study(Vallejos et al., 2016).

Properties	CMET (9)
UCS (MPa)	92 ± 14
Density ρ (kg/m^3)	2800
P-wave velocity C_L (m/s)	5070
Elastic Modulus E (GPa)	35 ± 5
Poisson's ratio ν	0.22 ± 0.04

2.1. Sample preparation

A total of 8 cubic samples were manufactured with a $50 \times 50 \times 50 \text{ mm}^3$ volume, in order to accomplish average size recommendation (Y. X. Zhou et al., 2012). Samples are rectified and the parallelism of opposite faces is less than 0.02 mm in 25mm. Perpendicularity among adjacent

surfaces is accomplished by rectifying and polishing, with a grinding machine, the lateral surfaces of a rock cylinder. Figure 3 shows two different samples with similar lithology but different types of veins, which implicates strictly anisotropy.

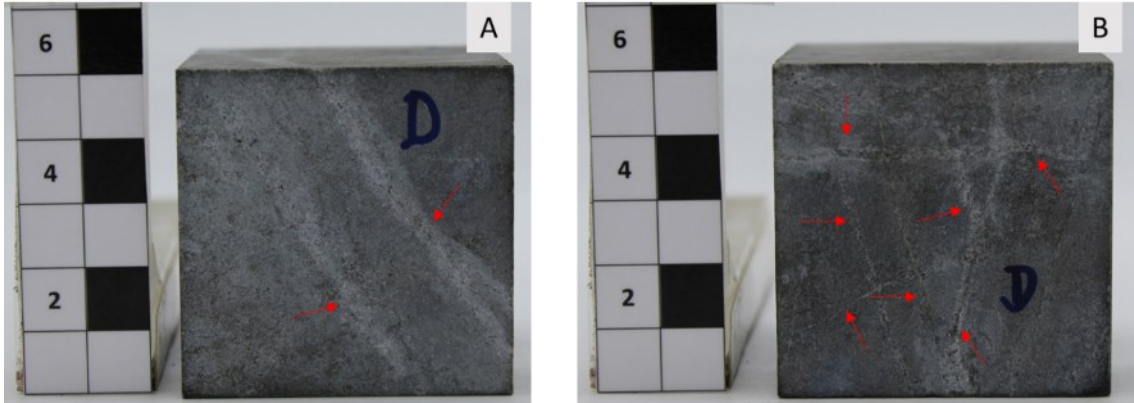


Figure 3 Photograph of samples before the experiment. A) CMET sample with two Late Magmatic Quartz veins cutting earlier Biotite veins (Skewes et al., 2005). B) Biotite veins in the CMET rock cubic sample.

2.2. Triaxial Hopkinson Bar System

In this work, we used a Triaxial Hopkinson Bar (THB) at Monash University (a 4, top) (K. Liu et al., 2019b, 2020; Q. B. Zhang & Zhao, 2014). The apparatus consists in a dynamic loading system, which includes a gas gun, a laser-beam module for velocity measures and a striker bar ($\rho_b = 7850 \text{ kg/m}^3$, $E_b = 210 \text{ GPa}$, $C_b = 5200 \text{ m/s}$, $\sigma_p = 930 \text{ MPa}$, $\varphi=40\text{mm}$, impact velocity up to 50 m/s), and three independent pairs of steel square bars (cross section 50 x 50 mm²) aligned orthogonally into three directions (XYZ): The striker, incident and transmission bars in the X-direction, two output bars in the Y-direction, and two output bars in the Z-direction.

Though triaxial pre-stress state can be obtained using THB, biaxial and uniaxial pre-stresses state can be achieved as well. The triaxial in-situ state in a cubic sample is achieved using two hydraulic cylinders that loads the incident and transmitted bars in X-direction and output bars in Y-direction, while one vertical hydraulic cylinder loads output bars in Z-direction. The dynamic load can be applied using the dynamic loading system, so that striker bar moves towards incident bar. Striker bar velocity is measured by the laser-beam module right before impact. A Red copper disc is placed as a pulse shaper at the impact face of incident bar (Y. X. Zhou et al., 2012).

For the test, cubic sample is placed in the loading cell at the intersection of the three axes. Once gas gun is triggered, striker bar moves towards incident bar in which an incident wave (ε_{In}) is produced along during the impact. It is transmitted through the bar to the sample, and interaction resulted in a transmission wave (ε_{Tr}) and a reflection wave (ε_{Re}) in X-direction, and transmitted waves ε_{y1} and ε_{y2} in the Y-direction. All waves are measured by strain gauges as shown in Figure 2 bottom.

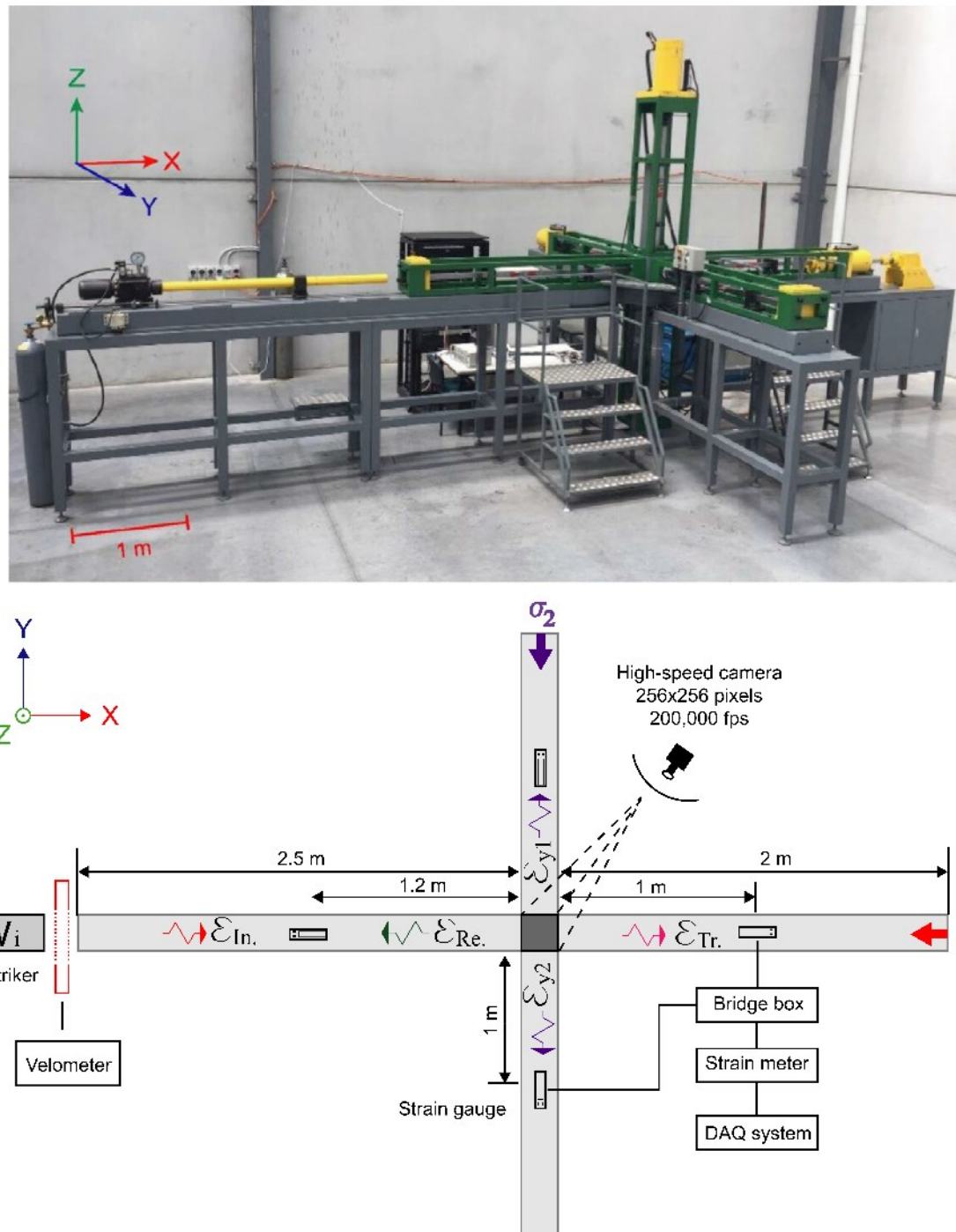


Figure 4 Triaxial Hopkinson Bar in Monash University simplified typical configuration of a Triaxial Hopkinson bar for biaxial compression test.

To study the fracture pattern experienced during dynamic deformation, we used a high-speed camera CMOS Phantom V2511 (resolution of 256x256 pixels, 200,000 frames per second (fps)). The data acquisition is done by a high-speed data acquisition (DAQ) system.

2.3. Processing

The Incident (ε_{In}), transmitted (ε_{Tr}) and reflected (ε_{Re}) waves are measured by strain gauges installed on the incident and transmission bars. This wave data is processed for each test and allows to recognize the peak load, strain, and strain rates. Furthermore, using ε_{In} , ε_{Tr} y ε_{Re} , following equations result:

$$\sigma_x(t) = \frac{A_b E_b}{2A_s} [\varepsilon_{In}(t) + \varepsilon_{Tr}(t) + \varepsilon_{Re}(t)] = \frac{A_b E_b}{2A_s} \varepsilon_{Tr}(t) \quad (1)$$

$$\varepsilon_x(t) = \frac{C_b}{L_s} \int_0^t [\varepsilon_{In}(t) - \varepsilon_{Tr}(t) - \varepsilon_{Re}(t)] dt = \frac{C_b}{L_s} \int_0^t \varepsilon_{Tr}(t) dt \quad (2)$$

$$\dot{\varepsilon}_x(t) = \frac{C_b}{L_s} [\varepsilon_{In}(t) - \varepsilon_{Tr}(t) - \varepsilon_{Re}(t)] = \frac{-2C_b}{L_s} \varepsilon_{Re}(t) \quad (3)$$

$$\sigma_y(t) = \frac{A_b E_b}{2A_s} [\varepsilon_{y1}(t) + \varepsilon_{y2}(t)] \quad (4)$$

$$\varepsilon_y(t) = \frac{C_b}{L_s} \int_0^t [\varepsilon_{y1}(t) + \varepsilon_{y2}(t)] dt \quad (5)$$

Where $\sigma_x(t)$ is the axial compressional stress as a function of time t , A_b is the section surface of the bars, E_b is the Young's modulus of the bars, C_b is the wave velocity in the bars, and L_s y A_s are the length and area of the sample. The parameter ε_x corresponds to strain and the subscripts *In*, *Re* and *Tr* refer to the incident, transmitted and reflected waves in the X-direction, respectively.

To be consistent, in this study compressive values are positive, then pre-stresses and dynamic compressive strength are as well. An example for interpretation of biaxial pre-stress state (40,30,0) in a Triaxial Hopkinson Bar test is shown in Figure 5.

The typical signal obtained from strain gauges in the impact X-direction is represented in Figure 5a, where Incident (in), Transmitted (Tr) and Reflected (Re) waves are measured. The average value 43 MPa indicated in the unloading stage of incident wave is a result of the interaction between the incident bar and wedge reaction device by the impact of the striker bar(Hokka et al., 2016; K. Liu et al., 2019a; H. Wang et al., 2021; Yang et al., 2020). Rock specimen under biaxial pre-stressed loading is deformed because of the dynamic load, and a transmitted wave can be measured in Y-direction due to Poisson's effect and confinement, as shown in Figure 5b.

To validate results of each dynamic compression test in a SHPB, the deformation uniformity of the sample must be checked (Q. B. Zhang & Zhao, 2014). Similarly, it must be checked during a Triaxial Hopkinson bar test, as indicated in Figure 5c, even though the stress concentration at the corners (X. Li et al., 2017). Thus, given a THB test, stress balance is achieved when the stresses measured at both ends of the sample are nearly equal, according to the next the equation $\sigma_{In}(t) + \sigma_{Re}(t) = \sigma_{Tr}(t)$. As shown in Figure 5c, the stress equilibrium is well achieved at around 65 μ s until 90 μ s, before sample failure. Total stress applied during dynamic load in each direction to the sample is shown in Figure 3d, where the maximum value for X-direction is 231 MPa and Y-direction is 59 MPa, and both consider the static (40,30,0) and the dynamic load ($\sigma_x(t), \sigma_y(t), 0$). Then, Figures 5 e,f show the dynamic stress-strain curves of the sample, calculated as Eq. 1 – 5.

Artículo 2: Dynamic mechanical properties under confinement of veined rocks from El Teniente Mine in Chile.

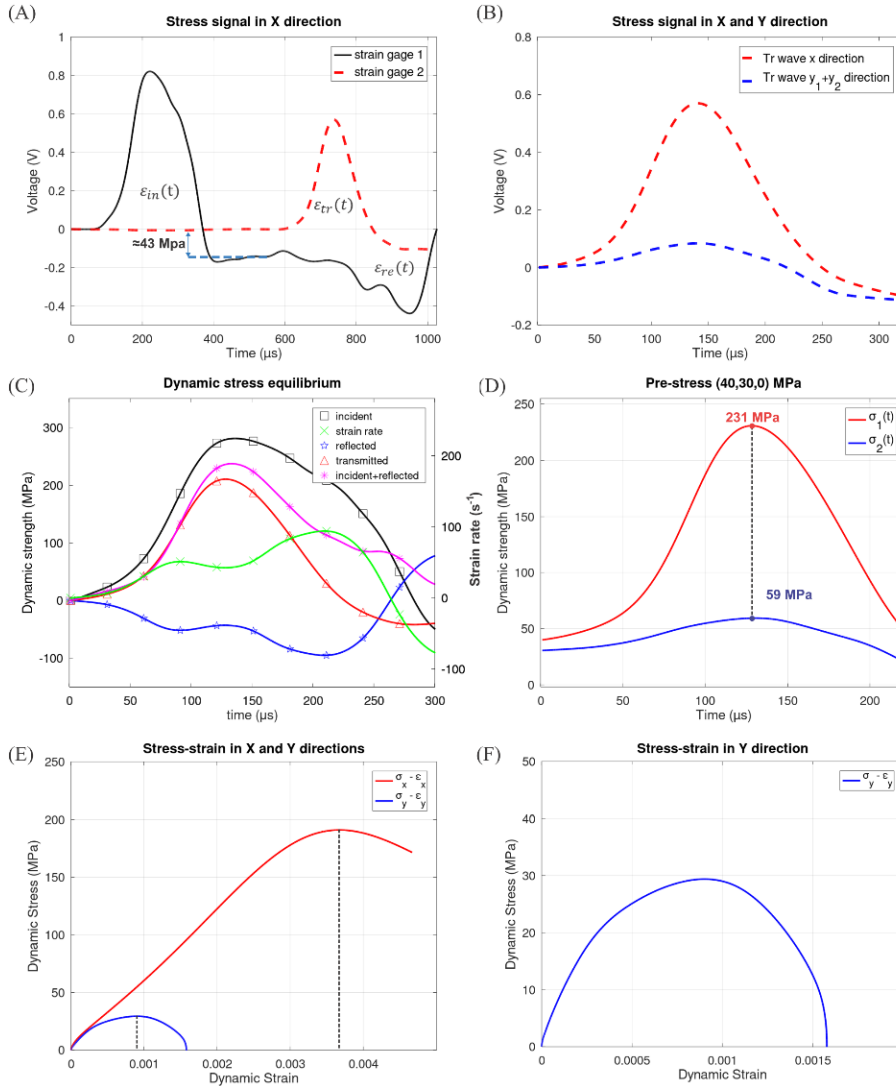


Figure 5 Summary of experimental data for the sample T-1-10 obtained after the Triaxial Hopkinson bar test. Pre-stress setup equals to (40,30,0) in this figure. (a) Typical incident ϵ_{inx} , transmitted ϵ_{trx} and reflected ϵ_{rex} wave signal. The moment when the material fails is recognized in the reflected wave. (b) Transmitted wave in the X-direction (red) and Y-direction (blue).(c) Dynamic stress equilibrium along X-direction. (d) Dynamic stress applied to the sample (pre-stress + dynamic stress) in both directions. (e) Dynamic stress vs Dynamic strain paths for X-direction (red) and Y-direction. (f) Dynamic stress vs dynamic strain path for Y-direction.

3. RESULTS AND DISCUSSION

3.1. Dynamic mechanical properties

In this study, a total of 8 samples were dynamically tested under high strain rates ($10-10^2$ s^{-1}) using a Triaxial Hopkinson Pressure Bar, under different confinement states: a) Uniaxial confinement state with $\sigma_1 = 40$ MPa and b) Biaxial confinement state with $\sigma_1 = 40$ MPa and the variation of σ_2 from 15 to 30 MPa. The impact velocity of the striker bar is set to 21 m/s.

The compaction stage is notorious in the samples tested under biaxial confine state equal to (40,30), nevertheless, it is difficult to identify in the (40,15) state, which is apparently showing a briefer stage. The compaction stage is particularly important given the presence of veinlets in the cubic samples. Under biaxial confinement, the veinlets might present small displacements in their dominion after the specimen is submitted to dynamic loads, indicated by white patches(X. Li et al., 2017), as the shear strength of these planes could be close to the shear stress obtained after both the pre-stresses and the dynamic load are applied. Hence, lateral confinement (i.e., X and Y bars) restricts the deformation, thus major displacements are observable to naked eye in the free face. On the other hand, there is no compaction stage in the stress-strain curves of the samples tested under uniaxial pre-stress state (40,0), and the curve is like that obtained when testing samples using a Split Hopkinson Pressure Bar. There is no retain of the displacement along veinlets due the presence of free faces in both Y and Z directions.

The strain-stress curves for the biaxial and uniaxial pre-stress state are shown the Figures 6A and B respectively. In general, the stress-strain curves for specimens tested under both biaxial and uniaxial confinement exhibit a linear elastic segment, which is identified from 75 μ s until 100 μ s after the loading wave arrived. There are differences in the elastic modulus of the specimens tested under the same biaxial pre-stress setup which has been described as proper characteristic of the CMET lithology (Marambio et al., 2000). Nevertheless, an increase of the elastic modulus E_d is observed after increasing σ_2 in samples that exhibits a Type I post-peak behavior.

The axial peak strength showed is calculated from the transmitted wave, thus the pre-stress σ_1 is not considered. The values of strength obtained under biaxial confinement state are in general higher than those obtained under uniaxial state, as shown in Figure 6C, and both higher than typical UCS values for this type of rock (i.e., 168-233 MPa against 92 \pm 5 MPa, respectively).

Two different post-peak behaviors are identified after peak strength is reached: a) Type I corresponds to the dynamic stress-strain curve obtained after testing of confined rocks, which results in a permanent strain represented as the hysteresis loop in the post peak state, and b) Type II, which corresponds to that obtained as a result after testing under uniaxial confinement state and in the T-1-9 sample. These two types of post peak behaviors are indicated in Figure 6A and B.

Recent works about dynamic properties in geomaterials under biaxial confinement state had similar results about Type I and Type II post peak curves (K. Liu et al., 2020; H. Wang et al., 2021). The reason behind this type of curves is revealed after analyzing the enclosed area of the post-peak segment, which indicates the release of the stored energy after peak load is reached. The input of energy to the specimen due to the incident wave must be lower than the critical energy, at which is dynamically fragmented, to fail as the Type I stress strain curve. Moreover, the rock fails like the Type II curve as the energy input surpasses the critical energy. Additional results about this topic are discussed further.

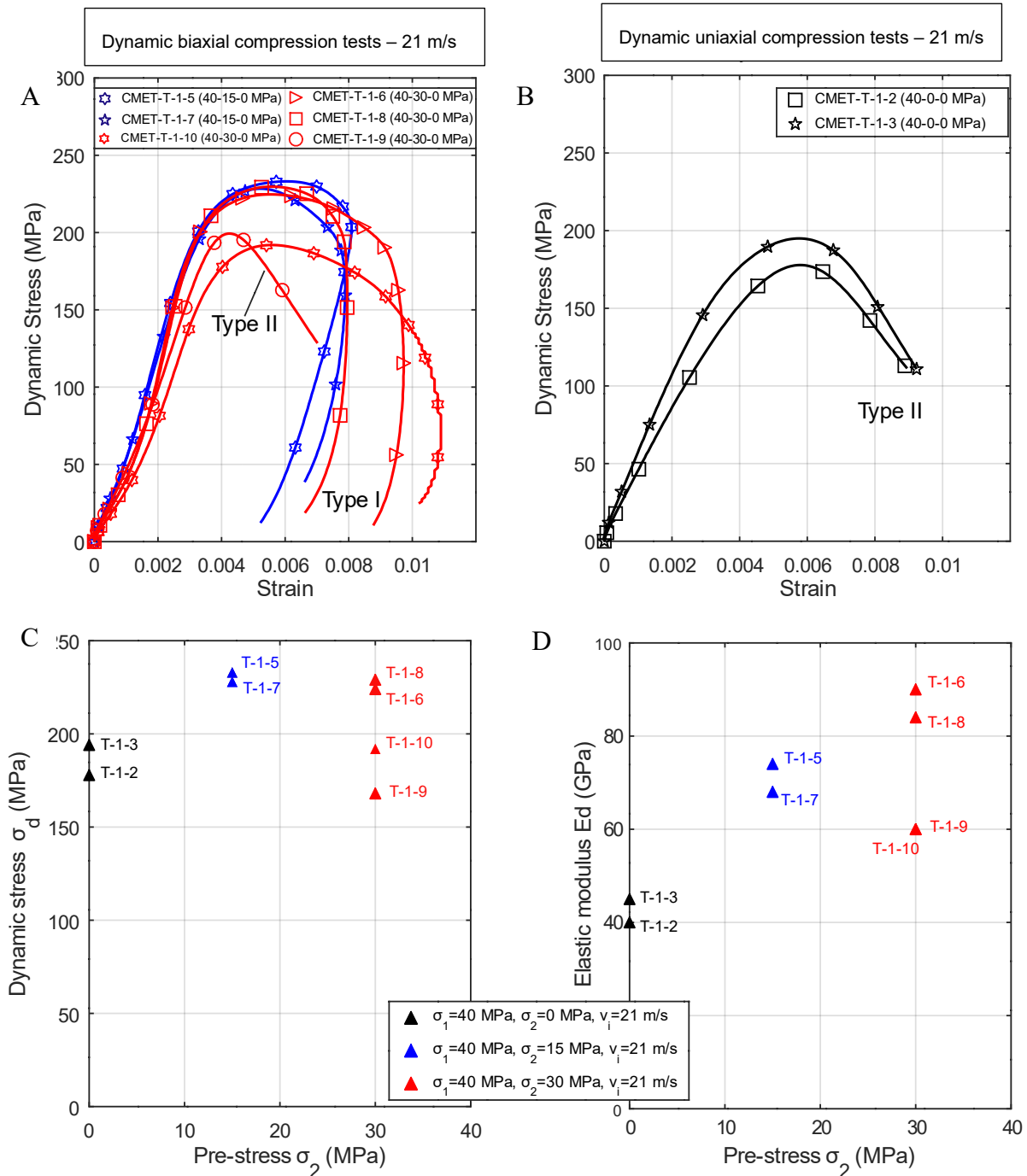


Figure 6 Summary of experimental results obtained from Triaxial Hopkinson bar test.

Samples were dynamically tested with an impact velocity of 21 m/s under high strain rates in the range from 66 to 176 s⁻¹. The confinement varies from uniaxial pre-stress ($\sigma_1 = 40) to biaxial confining state of (40,15) and (40,30).$

As previously mentioned, the variation of the elastic modulus E_d , after testing specimens under the same experimental conditions is intrinsic to the CMET lithology (Marambio et al., 2000). Furthermore, the dynamic elastic modulus E_d is higher when comparing to the one calculated under creep to quasi-static conditions(Q. B. Zhang & Zhao, 2014; Zhao, Li, et al., 1999).

Nevertheless, a clear dependence of σ_2 is appreciated in Figure 6D. In general, a major E_d is obtained after increasing σ_2 , which is related to the lateral restriction to displacement due the biaxial confinement state (Turichshev & Hadjigeorgiou, 2016, 2017).

In general, the peak strength observed in the samples under biaxial confinement is higher than those obtained under uniaxial state. This result is like to that obtained under creep strain rate tests (Turichshev & Hadjigeorgiou, 2016, 2017), and it is mainly because of the effect of veinlets, as the dilatancy of these rocks is controlled by the fracture of veinlets that are subparallel to the loading axis. Hence, whereas the confinement is lower, a major weakening of the veined rock is expected.

The discussion above mentioned is related to the fracture characteristics of specimens. In the Figure 7, samples T-1-2 and T-1-9 are shown, also both exhibit the Type II post-peak behavior. Main difference among them is the test confinement conditions at which are submitted: T-1-2 to uniaxial state (40,0) and T-1-9 to biaxial state (40,30). After 75 μs and until 100 μs , both samples have reached to the linear-elastic phase. However, the strain associated to crack stable growth (i.e., after 100 μs until 150 μs) is lower in the sample T-1-9 under the biaxial state, which can be interpreted as an effect of the lateral restriction due the confinement.

Artículo 2: Dynamic mechanical properties under confinement of veined rocks from El Teniente Mine in Chile.

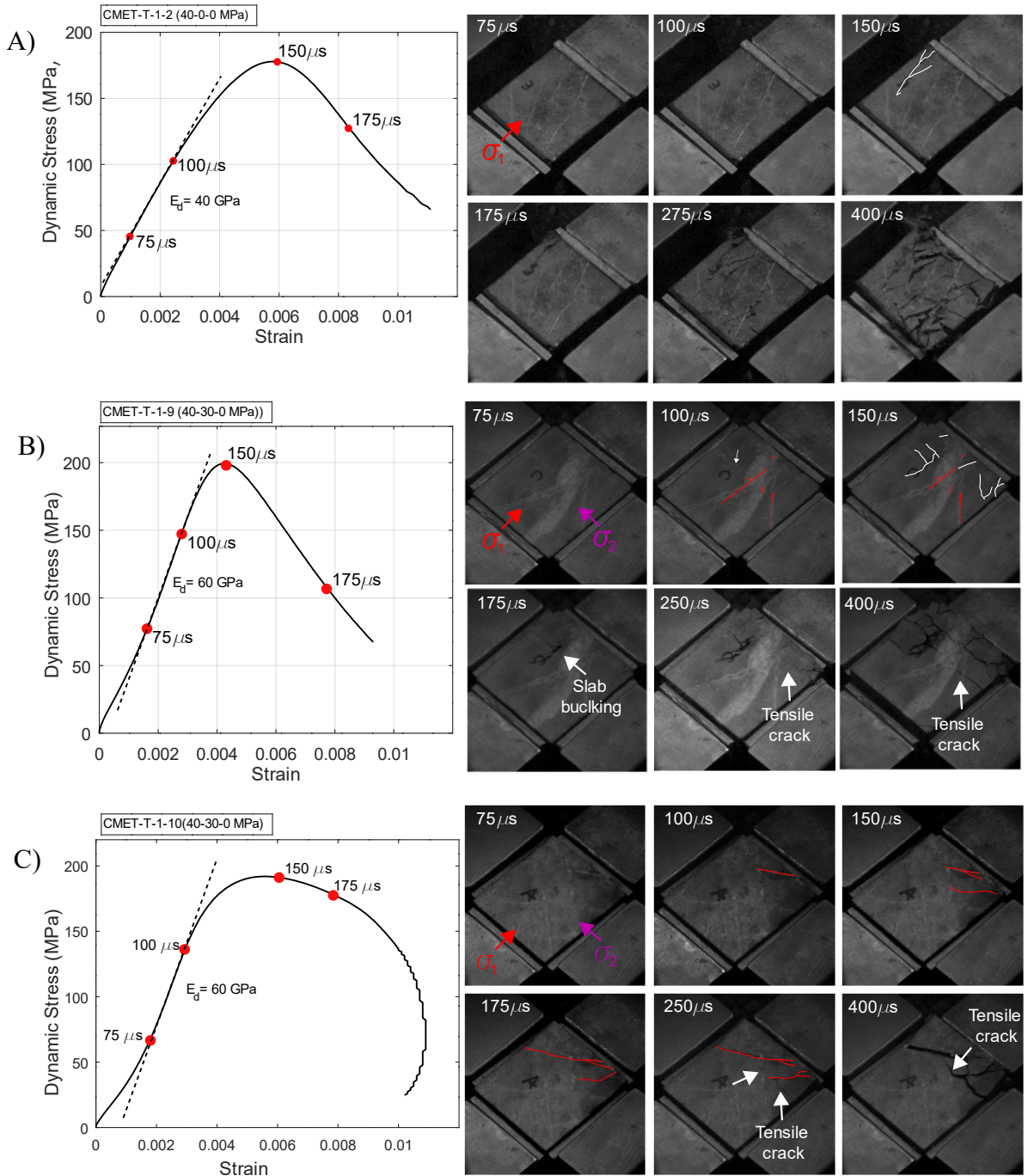


Figure 7 Fracture evolution of CMET rocks under uniaxial (a) and biaxial (b and c) pre-stress for Type-II dynamic stress-strain curves.

Moreover, the fracture characteristics differs one from another, as shown from 175 μs to 400 μs : T-1-2 resulted totally fragmented and even partially pulverized, whereas failure was controlled by the propagation of shear cracks. On the other hand, T-1-9 presented slab buckling from the free face (X-Z plane) and tensile cracks can be observed in the ejected slabs (See Figure 7B, 400 μs). More about slab ejection and its relation to strainburst is discussed further.

3.2. Fracture pattern

During the tests, all the samples resulted with a certain grade of damage, indicated by the stress-strain curves: a) The samples exhibiting Type I post-peak curve did not lost the load capacity under biaxial confinement, even though fractures are observed to be subparallel to the dynamic load (T-1-8 as an example), and b) The samples exhibiting Type II post peak curve lost the load capacity after fragmentation of the specimen.

The fracture orientation observed T-1-8 sample, under biaxial confinement, is shown in the Figure 8. It is evident that most of the fractures occurs in the X-Y or X-Z planes (i.e., parallel to sub-parallel to σ_1). Moreover, fractures are related with veinlets parallel or subparallel to σ_1 . The phenomenon is related to the fact that a veinlet is a weak plane with mineral infills(Brzovic & Villaescusa, 2007; Turichshev & Hadjigeorgiou, 2016, 2017; Vallejos et al., 2016), and to that microcracks generated after the linear-elastic phase are parallel to the σ_1 direction(Zhao, Li, et al., 1999). In this case, the post-peak behavior indicates a Type I stress-strain curve, which is related to that the energy input did not reach the critical energy for reproducing slab buckling.

Similarly, the fracture pattern of T-1-10 sample take place in cracks that are subparallel to σ_1 . An important influence of the veinlets in the crack formation and growth is observed in the side faces (Y-direction), as shown in the Figure 9. Furthermore, a major number of veinlets are cracked because of the loading wave when compared to T-1-8.

Even though the post-peak behavior of the T-1-10 specimen can be described as a Type I, this stress-strain curve is considered as a transitional post-peak state from Type I to Type II. This statement is sustained by the following results:

- It is shown that the peak strength of Type I curve, after comparing post-peak curves of the same biaxial confinement state, is considerably lower (Figure 6C). It is noted that the specimen T-1-10 shows an intermediate value.
- Similar as the above mentioned, the dynamic elastic modulus E_d of the T-1-10 specimen is an intermediate value between the elastic modulus of samples with Type I and II curves (Figure 6D).
- The specimen has not lost the load capacity, represented by the loop in the post-peak stage, such as the type I stress-strain curves. Furthermore, under biaxial confinement, the specimen should behave as stable, though with a lower competence (i.e., lower Elastic modulus and peak strength).
- Even though the slab buckling after the peak load is hard to identify, block ejection from the fee face occurs approximately after 400 μ s. Moreover, the orientation of the fractures and the geometry of the parts formed after fractures (blocks) are like to that obtained in the T-1-9 specimen (Figure 10).

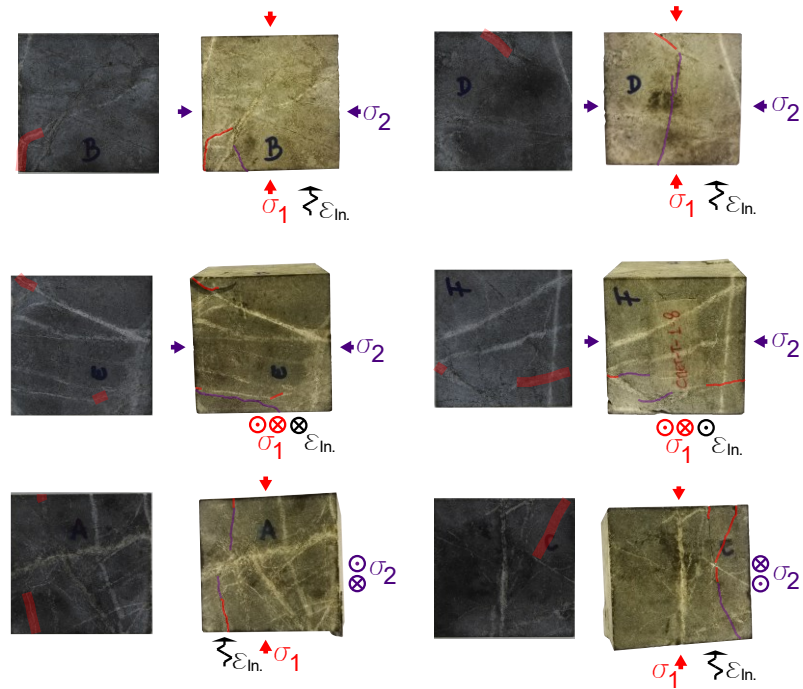


Figure 8 Fractured rock from CMET under biaxial pre-stress (40,30,0). Type-I Post-peak behavior for this sample (T-1-8). The thick red lines in the left picture indicate a veinlet that was cracked after the test. The same veinlet (or crack) is pointed as a red line in the right picture. The purple line indicates the crack is in the groundmass.

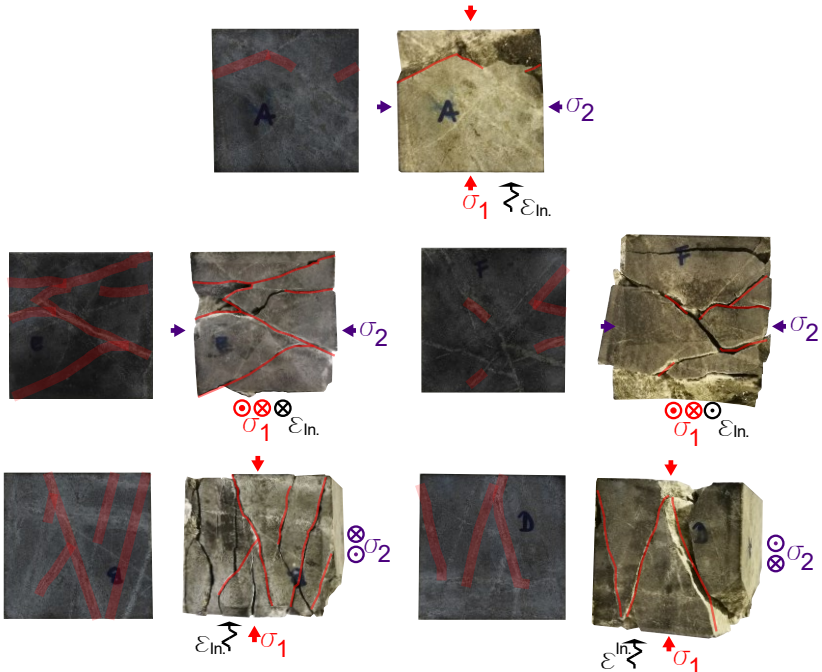


Figure 9 Fractured specimen (T-1-10) tested under biaxial pre-stress (40,30). The stress-strain curve exhibits a Type-II post-peak behavior. Fracture characteristic indicates propagation from

the corner to the center. The thick red lines in the left picture indicate a veinlet that results cracked after the test. The same veinlet (or crack) is pointed as a red line in the right picture.

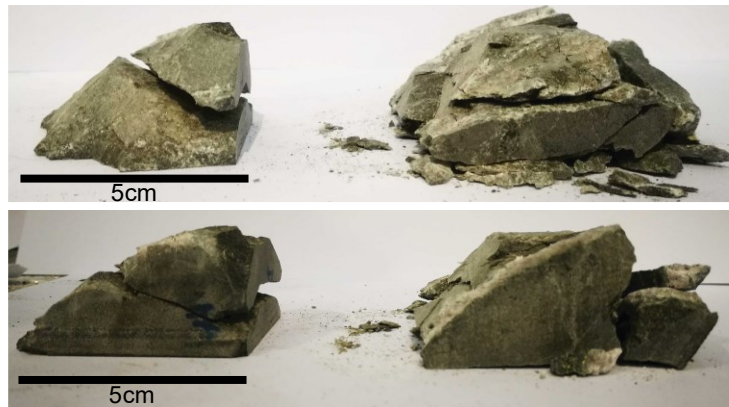


Figure 10 Fractured specimen (T-1-9) tested under biaxial pre-stress (40,30,0). The stress-strain curve exhibits a Type-II post-peak behavior. Fracture characteristic indicates propagation from the corner to the center. The upper and bottom pictures show the front and rear of the fractured sample, respectively.

The similarities about fractured T-1-10 and fragmented T-1-9 specimens can be observed in previous works about dynamic mechanical properties of sandstones and concrete aggregates (K. Liu et al., 2019b, 2020; H. Wang et al., 2021) as shown in Figure 11. The fragmentation in the three samples is clearly seen, whereas fracture orientations are subparallel to the load direction.

It is described that cracks propagation starts from the edge to the center, and in particular from the corners with a certain angle of propagation (K. Liu et al., 2020). Although most of the cracks observed in this study were propagated through veinlets, both the resultant geometry of the blocks and the crack orientation is like to that described for sandstones, which suggest a similar but modified crack propagation by the veinlets, which fails to the shear stress and propagates the fracture while reducing the mechanical properties (i.e., peak strength and the elastic modulus).

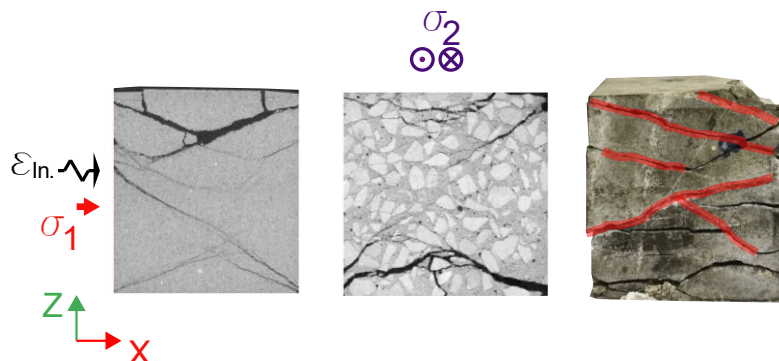


Figure 11 2D greyscale slices of fractured sandstone (K. Liu et al., 2020) (left) and concrete aggregate (H. Wang et al., 2021) (middle) after tested under biaxial state. Fractured CMET

(right) tested under biaxial pre-stress (40,30) state. Red thick lines represent cracked veinlets in the sample.

3.3. Post-peak behavior and strainburst

Rockburst phenomena is a major concern nowadays, and the understanding of such events is one of the main challenges for underground mining.

The strainburst phenomena is categorized according to the triggering mechanism (Ming Cai & Kaiser, 2018), as shown in Figure 3. In this study, the dynamically loaded strainburst is successfully reproduced, after the results observed in samples T-1-9 and T-1-10, both under biaxial confinement state.

The input energy from the dynamic load is partially transformed into kinetic energy and is considered the source for ejection of fragments observed in the post-peak stage. Even though the geometrical features of the ejected fragments are not fully determined, the shape of the fragments is controlled by veinlets with favorable orientations (i.e., subparallel to the loading axis) due to the crack propagation through their infills or parallel to vein through intact rock. The compaction stage of the stress-strain curves in the biaxial state indicates accommodation due to micro-fissures, presumable in the veinlet dominion, considered to be the precursors white patches observed during the crack growth stage (i.e., after 100 μ s). As a result, veinlets are most likely to act as a weak plane after the tested specimen reached a crack growth stage, failing due to shear cracks and thus affecting and controlling the block formation process.

The effect of pre-stresses under biaxial confinement state in this study is the control of the stiffness after σ_2 increased. According to the strainburst proneness assessment, the brittle the rock is, then higher is the potential of strainburst. The dynamic elastic modulus can be two times the quasi-static elastic modulus (see Table 1). Hence, the potential of the dynamically loaded strainburst is higher when CMET rocks are subjected to dynamic loads, such as impact waves from undercutting or development blasting.

Finally, according to the observations in this study, the strainburst assessment with respect to the quasi-static mechanical properties may underestimate both the actual severity and the potential of a dynamically load strainburst. The increase of mechanical properties, in terms of stiffness and dynamic strength, due to biaxial in-situ stress and dynamic loadings, is an additional consideration to have in mind when assessing strainburst empirically. Thus, additional proposed considerations are indicated in the Table 2 for strainburst assessment

Table 2: Additional considerations proposal for strainburst assessment.

Strainburst proneness assessment: Additional considerations		
Criteria	Results	Consideration Proposal
Potential	<ul style="list-style-type: none"> • Enhancement stiffness and peak load during true biaxial state. • Shear cracks observed in the free faces in both uniaxial and biaxial states. 	The blasting methods might be considered as a factor that increase the strainburst potential under certain conditions of in-situ stress in veined rocks, firstly, due to the

	<ul style="list-style-type: none"> • Slab buckling and block ejection in veinlet-controlled cracks 	brittle failure of CMET rocks and the transient enhancement of the stiffness due a dynamic load.
Severity	<ul style="list-style-type: none"> • Crack propagation is controlled by veinlets. • Slab buckling due to veinlet-controlled crack after a dynamic load. 	<ul style="list-style-type: none"> • The severity of the dynamical loaded strainburst should be higher in veined rockmass. The crack propagation is conducted through veinlets and veins. Although the scale effect is not studied in this work, our results should be interpreted as a possible scenario when designing the excavation on brittle veined rocks.

4. Conclusions

The dynamic mechanical properties of andesite veined rocks from El Teniente, the major underground mine in Chile, are being studied for a better understanding of rockburst phenomena. In this study, cubic samples are submitted to uniaxial and biaxial confinement states by using a Triaxial Hopkinson Bar, whereas the fracture pattern of the free face is recorded by a high-speed camera device. Tests are planned to vary the impact velocity of 21 m/s. The mechanical properties such as dynamic compressional strength, elastic modulus, failure strain, and fracture pattern were calculated.

- The stress-strain curves of CMET rocks under biaxial confinement state are described. Two post-peak behaviours are observed: The Type I, associated with single fracturing with no loss of load capacity under confinement, and the Type II, associated with a fragmentation of the specimen, and ejection of rock fragments from the free faces.
- The crack propagation is controlled by veinlets. Even though fracture propagation is like to that obtained for homogeneous rocks (i.e., from the corners or sides to the centre), veinlets with favourable orientations to the loading axis showed to conduct the propagation.
- The increase of σ_2 under biaxial confinement state resulted in a clear improvement of the elastic modulus. Nevertheless, it does not affect the crack propagation through veinlets.

Two rockburst features are reproduced during biaxial tests. In effect, slab buckling and fragment ejection are observed in type II post-peak behaviour specimens. Fragment formation is controlled by veinlets. Moreover, samples' elastic modulus is higher as veined rocks are submitted to the coupled dynamic-static confinement state under high strain rates. The results are proposed to be considered in the proneness assessment of strainburst during excavations in deep underground mines in Chile.

Acknowledgments

FR and LFO gratefully acknowledge the financial support from the basal project FB-0809 of the Advanced Mining Technology Center (AMTC). The authors sincerely appreciate the permission given by CODELCO to publish this paper. Also, we thank Huachuan Wang and Wanrui Hu who continuously supported the tests, data acquisition and processing, and David Veloz who helped with the exhaustive preparation of samples. We also deeply acknowledge to Prof. Sofia Rebollo for their contributions and priceless comments to this research. This research has been supported by the National Agency for Research and Development of Chile (ANID) with grant FONDECYT 11190985. Data supporting the analysis and conclusions are available upon request to the corresponding author.

4 Conclusiones y trabajo futuro

4.1 Conclusiones generales

Se ha investigado la dinámica de las rocas con vetillas de tres yacimientos tipo pórfido cuprífero presentes en Chile: El Teniente, Chuquicamata y Andina. Así, el estudio comprende las propiedades mecánicas de las rocas ante una carga dinámica, en un estado desconfinado, confinado uniaxial y confinado en un estado biaxial real. Entrega además cualitativamente el comportamiento de la fractura frente a un aumento de la tasa de carga, y junto con ello se realiza un análisis sobre la severidad y el potencial de estallido de rocas en yacimientos con métodos de explotación subterráneos. En base a los resultados obtenidos, se concluye lo siguiente:

- El aumento de las propiedades mecánicas, es decir, la carga máxima y los valores de rigidez, debido al aumento de la tasa de deformación, la tasa de carga y la velocidad de impacto de la prueba se observa en la mayoría de las muestras probadas de las pruebas no confinadas (SHPB). Los rangos de cargas máximas en CMET y RB son similares a los observados en muestras isotrópicas, indicados por los gráficos factor de incremento dinámico vs log tasa de deformación, donde las tasas de deformación varían de 10 a 10^2 s⁻¹. Con respecto a las muestras de CHQ, el rango de cargas máximas exhibidas es mayor para el mismo rango de la tasa de deformación. La tasa de deformación crítica a la que la resistencia a la compresión dinámica de CHQ se vuelve dependiente de la deformación es menor que para las muestras CMET y RB.
- Las pruebas muestran que el proceso de falla está fuertemente controlado por la presencia de vetillas, tanto en un estado desconfinado como en uno confinado. En el caso desconfinado, a velocidades de impacto más bajas, la falla se clasifica como “aparentemente intactas”, o “dividida a través de una vetilla”. A medida que aumenta la velocidad del impacto, el patrón de fractura evoluciona desde “dividido a través de una vetilla”, hasta “fracturamiento múltiple”. El proceso de fractura siempre se inicia desde las vetillas, tanto por una sola vetilla como a través de múltiples vetillas. La aparición de “parches blancos” es observado en todas las velocidades de impacto, pero su presencia es cualitativamente mayor a tasas de carga más altas. Ninguna de las muestras resultó pulverizada. Para el caso de los ensayos confinados, aunque la propagación de la fractura es similar a la obtenida para rocas homogéneas (es decir, desde las esquinas o lados hacia el centro), las vetillas con orientaciones favorables o paralelas al eje de carga demostraron conducir la propagación.
- La mejora de las propiedades mecánicas instantáneas de las rocas con vetillas puede explicarse tanto por la coalescencia de las microfisuras en la masa fundamental como por la falta de homogeneidad de las muestras, donde las vetas actúan como mitigadores de tensiones, es decir, aumentan las concentraciones de tensiones y el mecanismo de redistribución en la masa fundamental. El mecanismo propuesto por Cho et al. (2003) se ajusta mejor a muestras bajo tasas de carga sin una fuerte dependencia de la tasa de deformación (muestras CMET y RB), mientras que el mecanismo postulado por Grady y colaboradores (Grady & Kipp, 1987; Grady & Lipkin, 1980) resulta adecuado para muestras con una fuerte dependencia de la tasa de deformación (muestras CHQ).
- Se describen las curvas de tensión-deformación de rocas CMET en estado de confinamiento biaxial. Se observan dos comportamientos posteriores al peak: el Tipo I, asociado con

fracturación simple sin pérdida de capacidad de carga bajo confinamiento, y el Tipo II, asociado con una fragmentación del espécimen y expulsión de fragmentos de roca de las caras libres.

- El aumento de σ_2 en estado de confinamiento biaxial resultó en una clara mejora del módulo elástico. Sin embargo, no afecta la propagación de la fisura a través de las vetillas.
- El fenómeno de strainburst se reproduce con éxito. En efecto, el pandeo de la losa (slab buckling) y la expulsión de fragmentos se observa en probetas con comportamiento post pico tipo II en estado de confinamiento biaxial tras ser sometidas a cargas dinámicas. Las vetillas controlan la formación de fragmentos mientras que el aumento de σ^2 aumenta la rigidez. Se propone que ambos resultados se consideren en la evaluación de la propensión de strainburst durante excavaciones en minas subterráneas en Chile.

4.2 Recomendaciones y trabajo futuro

Las conclusiones generales de la investigación proporcionan una perspectiva innovadora con respecto a las propiedades mecánicas de las rocas estudiadas. Esto corresponde a un aporte al conocimiento a través de la ciencia en pos de una mayor seguridad y entendimiento de los procesos naturales e inducidos que pueden ocurrir en grandes yacimientos con operaciones subterráneas en suelo chileno. Según la configuración tectónica en la que se encuentra Chile, los resultados y conclusiones podrían ser aplicables en otras partes del borde occidental de Sudamérica, y también del mundo.

Las limitaciones identificadas se relacionan principalmente a la alta dureza y rigidez que poseen las rocas ensayadas, y por consiguiente el riesgo que corren los equipos (SHPB y THB). Teniendo esto en consideración, se sugieren las siguientes recomendaciones y trabajos complementarios.

- Elaborar un plan experimental que contemple ensayos con repeticiones, es decir, ensayar de forma repetida con una velocidad de impacto y confinamiento fijo la misma muestra, y medir el cambio de las propiedades mecánicas de acuerdo con el número de repeticiones.
- Generar un modelo 3-D de las muestras, tanto antes como después de ensayar, mediante una reconstrucción a través de rayos X y micro-CT. Esto permite acceder a información estadística sobre la orientación de las fracturas con respecto a la dirección de las cargas.
- Aumentar el volumen de ensayos desconfinados, y así contar con una cantidad robusta de datos, de manera de construir las curvas DIF tanto para CMET, CHQ y RB.
- Elaborar un sistema de recuperación de fragmentos de manera que se pueda medir con el menor error posible su granulometría.
- Diseñar un modelo numérico para la modelación del proceso de fractura dinámica en rocas con vetillas como las ensayadas en este estudio.

5 Bibliografía

1. Brown ET, Hoek E. Trends in relationships between measured in-situ stresses and depth. *Int J Rock Mech Min Sci.* 1978;15(4):211-215. doi:10.1016/0148-9062(78)91227-5
2. Ahorner L. Present-Day stress field and seismotectonic block movements along major fault zones in central Europe. *Dev Geotecton.* 1975;9(C):233-249. doi:10.1016/B978-0-444-41420-5.50029-0
3. Engelder T, Sbar ML. Near-Surface In Situ Stress ' Introduction equilibrium inside a free body whose boundaries. October. 1984;89:9321-9322.
4. Chester FM, Chester JS. Stress and deformation along wavy frictional faults. *J Geophys Res Solid Earth.* 2000;105(B10):23421-23430. doi:10.1029/2000jb900241
5. Ferrarini F, Lavecchia G, de Nardis R, Brozzetti F. Fault Geometry and Active Stress from Earthquakes and Field Geology Data Analysis: The Colfiorito 1997 and L'Aquila 2009 Cases (Central Italy). *Pure Appl Geophys.* 2015;172(5):1079-1103. doi:10.1007/s00024-014-0931-7
6. Day JJ, Diederichs MS, Hutchinson DJ. Composite Geological Strength Index Approach with Application to Hydrothermal Vein Networks and Other Intrablock Structures in Complex Rockmasses. *Geotech Geol Eng.* 2019;37(6):5285-5314. doi:10.1007/s10706-019-00980-4
7. Brzovic A, Villaescusa E. Rock mass characterization and assessment of block-forming geological discontinuities during caving of primary copper ore at the El Teniente mine, Chile. *Int J Rock Mech Min Sci.* 2007;44(4):565-583. doi:10.1016/j.ijrmms.2006.09.010
8. Bewick RP, Kaiser PK, Amann F. Strength of massive to moderately jointed hard rock masses. *J Rock Mech Geotech Eng.* 2019;11(3):562-575. doi:10.1016/j.jrmge.2018.10.003
9. Phillips WJ. Hydraulic fracturing and mineralization. *J Geol Soc London.* 1972;128(4):337-359. doi:10.1144/gsjgs.128.4.0337
10. Gustafson LB, Hunt JP. The porphyry copper deposit at El Salvador, Chile. *Econ Geol.* 1975;70(5):857-912. doi:10.2113/gsecongeo.70.5.857
11. Sillitoe RH. Porphyry copper systems. *Econ Geol.* 2010;105(1):3-41. doi:10.2113/gsecongeo.105.1.3
12. Astudillo N, Roperch P, Townley B, Arriagada C, Maksae V. Importance of small-block rotations in damage zones along transcurrent faults. Evidence from the Chuquicamata open pit, Northern Chile. *Tectonophysics.* 2008;450(1-4):1-20. doi:10.1016/j.tecto.2007.12.008
13. Deckart K, Clark AH, Aguilar A. C, et al. Magmatic and hydrothermal chronology of the Giant Río Blanco porphyry copper deposit, central Chile: Implications of an integrated U-Pb and 40Ar/ 39Ar database. *Econ Geol.* 2005;100(5):905-934. doi:10.2113/gsecongeo.100.5.905
14. Skewes MA, Arévalo A, Floody R, Zuñiga PH, Stern CR. The El Teniente Megabreccia Deposit, The World' Largest Copper Deposit. 2005;1(Figure 2):1-37.
15. Vallejos JA, Suzuki K, Brzovic A, Mas D. International Journal of Rock Mechanics & Mining Sciences Application of Synthetic Rock Mass modeling to veined core-size samples. *Int J Rock Mech Min Sci.* 2016;81:47-61. doi:10.1016/j.ijrmms.2015.11.003
16. Turichshev A, Hadjigeorgiou J. Triaxial compression experiments on intact veined andesite. *Int J Rock Mech Min Sci.* 2016;86:179-193. doi:10.1016/j.ijrmms.2016.04.012

17. Turichshev A, Hadjigeorgiou J. Quantifying the effects of vein mineralogy, thickness, and orientation on the strength of intact veined rock. *Eng Geol.* 2017;226(June):199-207. doi:10.1016/j.enggeo.2017.06.009
18. Marambio F, Pereira J, Russo A. Caracterización de la propiedades geotécnicas de las “Andesitas de la mina”. Yacimiento El Teniente. Chile Central. Published online 2000:3.
19. H. Kolsky. An Investigation of the Mechanical Properties of Materials at very High Rates of Loading. *Proc Phys Soc Sect B.* Published online 1949:676-700.
20. Zhang QB, Zhao J. Determination of mechanical properties and full-field strain measurements of rock material under dynamic loads. *Int J Rock Mech Min Sci.* 2013;60:423-439. doi:10.1016/j.ijrmms.2013.01.005
21. Zhao J, Li HB, Wu MB, Li TJ. Dynamic uniaxial compression tests on a granite. *Int J Rock Mech Min Sci.* 1999;36(2):273-277. doi:10.1016/S0148-9062(99)00008-X
22. Zhang QB, Zhao J. A review of dynamic experimental techniques and mechanical behaviour of rock materials. *Rock Mech Rock Eng.* 2014;47(4):1411-1478. doi:10.1007/s00603-013-0463-y
23. Liu K, Zhang QB, Wu G, Li JC, Zhao J. Dynamic Mechanical and Fracture Behaviour of Sandstone Under Multiaxial Loads Using a Triaxial Hopkinson Bar. *Rock Mech Rock Eng.* 2019;52(7):2175-2195. doi:10.1007/s00603-018-1691-y
24. Bischoff P, Perry S. Compressive behaviour of concrete at high strain rates. *Mater Struct.* 1991;24:425-450.
25. Doan ML, Gary G. Rock pulverization at high strain rate near the San Andreas fault. *Nat Geosci.* 2009;2(10):709-712. doi:10.1038/ngeo640
26. Liu K, Zhang QB, Wu G, Li JC, Zhao J. Dynamic Mechanical and Fracture Behaviour of Sandstone Under Multiaxial Loads Using a Triaxial Hopkinson Bar. *Rock Mech Rock Eng.* 2019;0(0):0. doi:10.1007/s00603-018-1691-y
27. Liu K, Zhang QB, Zhao J. Dynamic increase factors of rock strength. *Rock Dyn & Exp Theor Appl - Proc 3rd Int Conf Rock Dyn Appl ROCODYN-3* 2018. Published online 2018:169-174.
28. Kumar A. The effect of stress rate and temperature on the strength of basalt and granite. *Geophysics.* 1968;33(3):501-510.
29. Lindholm US, Yeakley LM, Nagy A. The dynamic strength and fracture properties of dresser basalt. *Int J Rock Mech Min Sci.* 1974;11(5):181-191. doi:10.1016/0148-9062(74)90885-7
30. Malik A, Chakraborty T, Rao KS. Strain rate effect on the mechanical behavior of basalt: Observations from static and dynamic tests. *Thin-Walled Struct.* 2018;126(August 2017):127-137. doi:10.1016/j.tws.2017.10.014
31. Blanton TL. Effect of strain rates from 10-2 to 10 sec-1 in triaxial compression tests on three rocks. *Int J Rock Mech Min Sci.* 1981;18(1):47-62. doi:10.1016/0148-9062(81)90265-5
32. Doan ML, d'Hour V. Effect of initial damage on rock pulverization along faults. *J Struct Geol.* 2012;45:113-124. doi:10.1016/j.jsg.2012.05.006
33. Li XB, Lok TS, Zhao J. Dynamic characteristics of granite subjected to intermediate loading rate. *Rock Mech Rock Eng.* 2005;38(1):21-39. doi:10.1007/s00603-004-0030-7
34. Perkins RD, Green SJ, Friedman M. Uniaxial stress behavior of porphyritic tonalite at strain rates to 103/second. *Int J Rock Mech Min Sci.* 1970;7(5):527-535. doi:10.1016/0148-9062(70)90005-7

35. Wang Y, Tonon F. Dynamic validation of a discrete element code in modeling rock fragmentation. *Int J Rock Mech Min Sci.* 2011;48(4):535-545. doi:10.1016/j.ijrmms.2011.02.003
36. Xia K, Nasseri MHB, Mohanty B, Lu F, Chen R, Luo SN. Effects of microstructures on dynamic compression of Barre granite. *Int J Rock Mech Min Sci.* 2008;45(6):879-887. doi:10.1016/j.ijrmms.2007.09.013
37. Doan ML, Billi A. High strain rate damage of Carrara marble. *Geophys Res Lett.* 2011;38(19):1-6. doi:10.1029/2011GL049169
38. Liu S, Xu J, Liu J, Lu X. SHPB experimental study of sericite-quartz schist and sandstone. *Chinese J Rock Mech Eng.* 2011;30(9):1864-1871.
39. Li X, Zhou T, Li D. Dynamic Strength and Fracturing Behavior of Single-Flawed Prismatic Marble Specimens Under Impact Loading with a Split-Hopkinson Pressure Bar. *Rock Mech Rock Eng.* 2017;50(1):29-44. doi:10.1007/s00603-016-1093-y
40. Wang QZ, Li W, Xie HP. Dynamic split tensile test of Flattened Brazilian Disc of rock with SHPB setup. *Mech Mater.* 2009;41(3):252-260. doi:10.1016/j.mechmat.2008.10.004
41. Yao W, He T, Xia K. Dynamic mechanical behaviors of Fangshan marble. *J Rock Mech Geotech Eng.* 2017;9(5):807-817. doi:10.1016/j.jrmge.2017.03.019
42. Chong KP, Hoyt PM, Smith JW, Paulsen BY. Effects of strain rate on oil shale fracturing. *Int J Rock Mech Min Sci.* 1980;17(1):35-43. doi:10.1016/0148-9062(80)90004-2
43. Wang W, Zhao Y, Teng T, Zhang C, Jiao Z. Influence of Bedding Planes on Mode I and Mixed-Mode (I-II) Dynamic Fracture Toughness of Coal: Analysis of Experiments. *Rock Mech Rock Eng.* Published online 2020. doi:10.1007/s00603-020-02250-9
44. Yang G, Bi J, Li X, Liu J, Feng Y. SHPB Testing and Analysis of Bedded Shale under Active Confining Pressure. *J Eng (United Kingdom).* 2020;2020. doi:10.1155/2020/5034902
45. Blair DP. Blast vibration control in the presence of delay scatter and random fluctuations between blastholes. *Int J Numer Anal Methods Geomech.* 1993;17(2):95-118. doi:10.1002/nag.1610170203
46. Zhao J, Zhou YX, Hefny AM, et al. Rock dynamics research related to cavern development for ammunition storage. *Tunn Undergr Sp Technol.* 1999;14(4):513-526. doi:10.1016/S0886-7798(00)00013-4
47. Huang RQ, Wang XN. Analysis of dynamic disturbance on rock burst. *Bull Eng Geol Environ.* 1999;57(3):281-284. doi:10.1007/s100640050046
48. He M, e Sousa LR, Miranda T, Zhu G. Rockburst laboratory tests database - Application of data mining techniques. *Eng Geol.* 2015;185:116-130. doi:10.1016/j.enggeo.2014.12.008
49. Mudau A, Govender RA, Stacey TR. A step towards combating rockburst damage by using sacrificial support. *J South African Inst Min Metall.* 2016;116(11):1065-1074. doi:10.17159/2411-9717/2016/v116n11a9
50. Cai M, Kaiser PK. Rockburst Support. Vol 1.; 2018.
51. Liu K, Zhao J, Wu G, Maksimenko A, Haque A, Zhang QB. Dynamic strength and failure modes of sandstone under biaxial compression. *Int J Rock Mech Min Sci.* 2020;128(April). doi:10.1016/j.ijrmms.2020.104260
52. Cai M. Rock support in strainburst-prone ground. *Int J Min Sci Technol.* 2019;29(4):529-534. doi:10.1016/j.ijmst.2019.06.008

53. Kaiser PK, Cai M. Design of rock support system under rockburst condition. *J Rock Mech Geotech Eng.* 2012;4(3):215-227. doi:10.3724/sp.j.1235.2012.00215
54. Simser BP. Rockburst management in Canadian hard rock mines. *J Rock Mech Geotech Eng.* 2019;11(5):1036-1043. doi:10.1016/j.jrmge.2019.07.005
55. Zhou YX, Xia K, Li XB, et al. Suggested methods for determining the dynamic strength parameters and mode-I fracture toughness of rock materials. *Int J Rock Mech Min Sci.* 2012;49(June 2018):105-112. doi:10.1016/j.ijrmms.2011.10.004
56. Heal D, Potvin Y, Hudyma M. Evaluating rockburst damage potential in underground mining. *Proc 41st US Rock Mech Symp - ARMA's Golden Rocks 2006 - 50 Years Rock Mech.* 2006;(June 2006).
57. Dou L, Chen T, Gong S, He H, Zhang S. Rockburst hazard determination by using computed tomography technology in deep workface. *Saf Sci.* 2012;50(4):736-740. doi:10.1016/j.ssci.2011.08.043
58. Zhu WC, Li ZH, Zhu L, Tang CA. Numerical simulation on rockburst of underground opening triggered by dynamic disturbance. *Tunn Undergr Sp Technol.* 2010;25(5):587-599. doi:10.1016/j.tust.2010.04.004
59. Chun'an Tang. Numerical simulation of progressive rock failure and associated seismicity. *Int J rock Mech Min Sci Geomech Abstr.* 1997;34(2):249-261. doi:10.1016/S0148-9062(96)00039-3
60. Ma J, Dong L, Zhao G, Li X. Discrimination of seismic sources in an underground mine using full waveform inversion. *Int J Rock Mech Min Sci.* 2018;106(April):213-222. doi:10.1016/j.ijrmms.2018.04.032
61. Dong LJ, Li XB, Peng K. Prediction of rockburst classification using Random Forest. *Trans Nonferrous Met Soc China (English Ed.)* 2013;23(2):472-477. doi:10.1016/S1003-6326(13)62487-5
62. Su G, Feng X, Wang J, Jiang J, Hu L. Experimental Study of Remotely Triggered Rockburst Induced by a Tunnel Axial Dynamic Disturbance Under True-Triaxial Conditions. *Rock Mech Rock Eng.* 2017;50(8):2207-2226. doi:10.1007/s00603-017-1218-y
63. Su G, Jiang J, Feng X, Jiang Q, Chen Z, Mo J. Influence of loading rate on strainburst: an experimental study. *Bull Eng Geol Environ.* 2019;78(5):3559-3573. doi:10.1007/s10064-018-1351-1
64. Li X, Gong F, Tao M, et al. Failure mechanism and coupled static-dynamic loading theory in deep hard rock mining: A review. *J Rock Mech Geotech Eng.* 2017;9(4):767-782. doi:10.1016/j.jrmge.2017.04.004
65. Zhang Y, Ma J, Sun D, Zhang L, Chen Y. AE Characteristics of Rockburst Tendency for Granite Influenced by Water Under Uniaxial Loading. *Front Earth Sci.* 2020;8(March):1-12. doi:10.3389/feart.2020.00055
66. CODELCO. Memoria Anual 2019. Published online 2019.
67. Schellmann M, Bermudo E, Díaz D. Auscultación , Monitoreo y Control de Taludes Mineros Anglo-American Sur, División Bronces.; 2014.
68. Dai F, Huang S, Xia K, Tan Z. Some fundamental issues in dynamic compression and tension tests of rocks using split Hopkinson pressure bar. *Rock Mech Rock Eng.* 2010;43(6):657-666. doi:10.1007/s00603-010-0091-8
69. Zhang Q-B, Liu K, Wu G, Zhao J. Dynamic Deformation, Damage, and Fracture in Geomaterials.; 2021. doi:10.1007/978-1-4614-8968-9_73-1

70. Li J, Zhao J, Wang HC, Liu K, Zhang QB. Fracturing behaviours and AE signatures of anisotropic coal in dynamic Brazilian tests. *Eng Fract Mech.* 2021;252(February). doi:10.1016/j.engfracmech.2021.107817
71. Wong LNY, Einstein HH. Systematic evaluation of cracking behavior in specimens containing single flaws under uniaxial compression. *Int J Rock Mech Min Sci.* 2009;46(2):239-249. doi:10.1016/j.ijrmms.2008.03.006
72. Bewick RP, Amann F, Kaiser PK, Martin CD. Interpretation of UCS test results for engineering design. 13th ISRM Int Congr Rock Mech. 2015;2015-MAY(May):1-14.
73. Li QM, Meng H. About the dynamic strength enhancement of concrete-like materials in a split Hopkinson pressure bar test. 2003;40:343-360.
74. Cho SH, Ogata Y, Kaneko K. Strain-rate dependency of the dynamic tensile strength of rock. *Int J Rock Mech Min Sci.* 2003;40(5):763-777. doi:10.1016/S1365-1609(03)00072-8
75. Grady DE, Kipp ME. Dynamic Rock Fragmentation. ACADEMIC PRESS LIMITED; 1987. doi:10.1016/b978-0-12-066266-1.50015-6
76. Grady DE, Lipkin J. Criteria for Impulsive Rock Fracture. *Geophys Res Lett.* 1980;7(4):255-258.
77. Lankford J. The role of tensile microfracture in the strain rate dependence of compressive strength of fine-grained limestone-analogy with strong ceramics. *Int J Rock Mech Min Sci.* 1981;18(2):173-175. doi:10.1016/0148-9062(81)90742-7
78. Wang H, Zhao J, Li J, Liu K, Braithwaite CH, Zhang Q. Dynamic mechanical properties and fracturing behaviour of concrete under biaxial compression. *Constr Build Mater.* 2021;301:124085. doi:10.1016/j.conbuildmat.2021.124085
79. Kaiser PK, McCreath DR, Tannant DD. Canadian Rockburst Support Handbook. 1996;(January):314.
80. Cai M. Influence of intermediate principal stress on rock fracturing and strength near excavation boundaries-Insight from numerical modeling. *Int J Rock Mech Min Sci.* 2008;45(5):763-772. doi:10.1016/j.ijrmms.2007.07.026
81. Barton N, Shen B. Risk of shear failure and extensional failure around over-stressed excavations in brittle rock. *J Rock Mech Geotech Eng.* 2017;9(2):210-225. doi:10.1016/j.jrmge.2016.11.004
82. Zhang QB, Zhao J. Determination of mechanical properties and full-field strain measurements of rock material under dynamic loads. *Int J Rock Mech Min Sci.* 2013;60:423-439. doi:10.1016/j.ijrmms.2013.01.005
83. Zhou J, Li X, Mitri HS. Evaluation method of rockburst: State-of-the-art literature review. *Tunn Undergr Sp Technol.* 2018;81(October 2017):632-659. doi:10.1016/j.tust.2018.08.029
84. Hokka M, Black J, Tkalich D, et al. Effects of strain rate and confining pressure on the compressive behavior of Kuru granite. *Int J Impact Eng.* 2016;91:183-193. doi:10.1016/j.ijimpeng.2016.01.010